Modeling the Translocation of DNA Structures through Nanopores

Von der Fakultät Mathematik und Physik der Universität Stuttgart genehmigte Abhandlung zur Erlangung der Würde eines Doktors der Naturwissenschaften (Dr. rer. nat.)

vorgelegt von

Kai Stephan Szuttor
aus Ostfildern

Hauptberichter: Prof. Dr. Christian Holm
Mitberichter: Apl. Prof. Dr. Johannes Roth
Vorsitzender: Prof. Dr. Peter Michler

Tag der mündlichen Prüfung: 13.09.2021

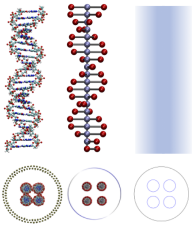

Institut für Computerphysik,
Universität Stuttgart
2021

Contents

Glossary

B

BTE BOLTZMANN transport equation. 22

C

C++ a compiled system programming language with a focus on performance and efficiency. 31

D

DNA deoxyribonucleic acid. 9–12, 15, 17–20, 29, 35, 65–73, 76–82, 86–89, 107–109, 111, 112, 114

dsDNA double-stranded DNA. 35, 36, 41, 66, 67, 72, 79, 80, 82, 84, 86–89

E

ESPResSo Simulation package to perform coarse-grained molecular dynamics simulations. 31, 32, 43, 45, 65–67, 119, 120

F

FEM a method to numerically solve differential equations on a mesh. 25, 52, 53

G

git a distributed version control system. 117, 118

git submodule a reference to a snapshot of another git version controlled project. 118

GROMACS Simulation package to perform all-atom molecular dynamics simulations. 32, 33, 35

L

LAMMPS a parallel molecular dynamics software developed at the Sandia National Laboratories. 32

LB lattice-Boltzmann. 23, 31, 42–44, 47

LBGK lattice Bhatnagar-Gross-Krook. 23

LBM a method to numerically solve a discretized version of the Navier-Stokes equation on a lattice. 15, 22–25, 119

M

molecular dynamics a simulation method that is based on numerically solving Newton's equations of motion. 20, 21, 24, 25, 31, 32

MPI a standard describing an interface for passing messages and data between distributed memory locations. 32

P

Python a interpreted, high-level programming language. It's language constructs aim to support writing clear code. 31, 45

R

RNA ribonucleic acid. 15, 18

T

Tcl a high-level, general-purpose, interpreted, dynamic programming language. 45

W

WCA interaction modified version of the Lennard-Jones interaction that only contains the repulsive part. 40

Chapter 1

Introduction

The deoxyribonucleic acid (DNA) molecule is built up by two polynucleotides that form a double helix. It is widely known as an information carrier for the building plans of any life on Earth. Especially for this reason it is — and has already been for a long time — of special interest in the scientific community to understand the physical and chemical interactions between DNA and its environment in great detail. The information contained in the molecule is encoded in the sequence of nucleobases that form so-called base pairs via hydrogen bonds. Thus, by knowing the sequence of the nucleobases along the DNA strand it is possible to gain any information about the building plan of life contained in the molecule. This information can help to diagnose diseases, *e. g.* in the area of non-invasive prenatal testing. Also, the understanding of the cancer disease has been largely influenced by DNA sequencing [1]. Therefore, a lot of effort has been put into finding cost-efficient and fast methods to sequence whole chromosomes that contain the complete genetic information of an organism.

One of the approaches to DNA sequencing is the so-called resistive pulse sensing. The idea of using a setup of two electrolyte reservoirs that are connected only by a tiny orifice in a membrane to count and size particles can be tracked back to the experiments of Wallace Coulter [2]. Back then he was interested in counting red and white blood cells due to the politically unstable situ-

ation in the 1940s that led to a fear of a nuclear war and with it the need for a method to rapidly analyse human blood arose [3]. For a pure electrolyte solution the conductivity is approximately constant, whereas spikes in the current can be observed if a blood cell traverses the orifice. Therefore, by using this modulation effect COULTER was able to count the blood cells in the sample. In the meantime, more refined setups allowed detecting smaller and smaller analytes [4, 5, 6, 7, 8, 9, 10, 11, 12, 13]. Nowadays, the tiny orifices turned into pores with diameters on the nanometer scale that are even capable of detecting single DNA molecules and identifying different nucleotides is possible [14, 15] which has already been commercially implemented [16, 17, 18, 19]. Mainly two different types of nanopores are used in science and technology, namely biological nanopores and solid-state nanopores. The biological nanopores most widely used and investigated are the exotoxin α-hemolysin and the mycobacterial porin MspA [20, 21]. The solid-state nanopores are fabricated by various methods, *e. g.* ion or electron beam drilling through thin solid-state membranes [22, 23], by utilizing dielectric breakdown between two electrolyte reservoirs separated by a thin silicon plate [24, 25] or by heating and simultaneous pulling of glass tubes [26, 27]. Especially the latter approach has been extensively used to study DNA nanopore systems since the preparation is very fast and cost effective in comparison to fabrication methods for other solid-state nanopores [28, 29, 30, 31].

Experimentally, various studies investigated the ionic current modulation caused by the translocation of a DNA molecule through a nanopore [32, 33, 34, 35, 36, 37, 38, 39, 40, 41]. Numerical studies of nanometre sized pores for sensing applications can be found in Refs. [42, 43, 44, 45, 46, 47, 48, 49, 50, 51, 52, 53, 54, 55]. A general overview can be found in the review articles in Refs. [56, 9, 57, 58, 59, 60, 13].

Numerical simulations have proven to be a viable tool to investigate soft-matter systems and often enable scientists to investigate details that are not accessible in experiments. Modeling DNA-nanopore systems has since been a challenge due to the large separation of length scales. The whole system including the electrolyte reservoir often approaches several microme-

ters in dimension, while the counter-ion layer in the vicinity of the DNA varies on the length scale of Ångstroms to nanometers and a single turn of the DNA's helix is several nanometers in length. All-atom simulations of the translocation of a short (20 base pairs) DNA molecule through an artificial nanometer sized pore have first been performed in 2004 by Aksementiev *et al.* [61] These simulations, however, had been restricted to short DNA sequences and suffered from sampling issues. In order to reduce the computational costs and improve on the sampling, Kesselheim *et al.* [47] performed all-atom simulations of a 20 base pair sequence of DNA in a nanopore without the electrolyte reservoirs. In addition, periodic boundary conditions had been applied along the helix which enabled the measurement of the ionic current without finite size effects. These simulations had been able to reproduce experimental values for the ionic current through the pore as a function of the bulk electrolyte concentration and revealed a previously unknown mobility reduction of the ions in the vicinity of the DNA. In this work we used this setup as a building block by replicating the double helix several times and restrain this configuration in space in order to construct more complex DNA origami structures on the all-atom level of detail.

In order to reach longer time- and length-scales, so-called coarse-grained DNA models with a reduced number of degrees of freedom have since been developed in several groups [62, 63, 64, 65, 66, 56, 67, 68, 69, 70]. These models do not incorporate the interaction between every atom with every other atom of a system but combine several interaction sites into a single effective interaction. In addition, the interactions between solute and solvent are often treated implicitly by introducing stochastic collisions with an imaginary heat bath [71].

However, most of the coarse-grained DNA models do not explicitly incorporate electrostatic interactions and hydrodynamic interactions within a united model. Especially, hydrodynamic interactions often cannot be neglected for the electrophoretic transport of biomolecules and polyelectrolytes in general [72, 73, 47, 74]. Electrostatic interactions on the other hand can in some situations be treated via short-ranged interaction poten-

tials between charged particles if electrostatic screening effects are very strong, *i. e.* in systems with a high electrolyte concentration. However, the typical salt concentrations investigated for DNA translocation setups do not allow to treat the interaction of charged species as a short-ranged interaction. The length-scales on which the electrostatic interactions are relevant range from around 1 Å to about 10 nm. Weik *et al.* [52] developed a model incorporating explicit hydrodynamics and electrostatic interactions and were able to reproduce the aforementioned ion mobility reduction near the DNA strand by incorporating a phenomenological frictional interaction between ions and the DNA. This frictional interaction was incorporated in a momentum conserving way [75] and thus preserves the hydrodynamic interactions in the system. Extensions to this model [76] even showed that it is possible to reproduce experimental data on the salt-dependent electrophoretic mobility [77] and persistence length [78]. In this work this coarse-grained DNA model is used as a building block for the investigation of more complex DNA structures.

Early continuum models [52] of DNA nanopore systems based on a so-called cell-model [79, 80, 81, 54] failed to reproduce the ionic current modulation that has been observed in experiments. This is somehow expected due to the fact that these systems did not take into account the DNA specific mobility reduction of the ions around the DNA helices. By extending these models and explicitly taking into account this frictional interaction a mean field model capable of reproducing ionic current data from experimental setups is presented in this thesis.

Publications

The following paper with draft status will soon be submitted and is discussed in this dissertation:

> Kai Szuttor, Patrick Kreissl, and Christian Holm. Investigation of Finite Size Effects in DNA Nanopore Systems. *To be submitted (as of July 2021)*

During the course of this thesis I also contributed to the following peer-reviewed publications (not all of them are directly connected to the work presented in this thesis, the framed publications are explicitly discussed):

Kai Szuttor, Florian Weik, Jean-Noël Grad, and Christian Holm. Modeling the current modulation of bundled DNA structures in nanopores. *The Journal of Chemical Physics*, 154(5):054901, 2021. doi: 10.1063/5.0038530

Miru Lee, Christoph Lohrmann, Kai Szuttor, Harold Auradou, and Christian Holm. The influence of motility on bacterial accumulation in a microporous channel. *Soft Matter*, 17:893–902, 2021. doi: 10.1039/D0SM01595D

Florian Weik, Kai Szuttor, Jonas Landsgesell, and Christian Holm. Modeling the current modulation of dsDNA in nanopores – from mean-field to atomistic and back. *European Physical Journal Special Topics*, 227(14):1639–1655, 2019. doi: 10.1140/epjst/e2019-800189-3

Florian Weik, Rudolf Weeber, Kai Szuttor, Konrad Breitsprecher, Joost de Graaf, Michael Kuron, Jonas Landsgesell, Henri Menke, David Sean, and Christian Holm. ESPResSo 4.0 – an extensible software package for simulating soft matter systems. *European Physical Journal Special Topics*, 227 (14):1789–1816, 2019. doi: 10.1140/epjst/e2019-800186-9

Miru Lee, Kai Szuttor, and Christian Holm. A computational model for bacterial run-and-tumble motion. *The Journal of Chemical Physics*, 150:174111, 2019. doi: 10.1063/1.5085836

Jonas Landsgesell, David Sean, Patrick Kreissl, Kai Szuttor, and Christian Holm. Modeling gel swelling equilibrium in the mean field: From explicit to Poisson-Boltzmann models. *Physical Review Letters*, 122:208002, 5 2019. doi: 10.1103/PhysRevLett.122.208002

Johannes Hartmann, Tamal Roy, Kai Szuttor, Jens Smiatek, Christian Holm, and Steffen Hardt. Relaxation of surface-tethered polymers under moderate confinement. *Soft Matter*, 14(38):7926–7933, 2018. doi: 10.1039/c8sm01246f

Tamal Roy, Kai Szuttor, Jens Smiatek, Christian Holm, and Steffen Hardt. Conformation and dynamics of long-chain end-tethered polymers in microchannels. *Polymers*, 11(3): 488, 2019. doi: 10.3390/polym11030488

Kai Szuttor, Tamal Roy, Steffen Hardt, Christian Holm, and Jens Smiatek. The stretching force on a tethered polymer in pressure-driven flow. *The Journal of Chemical Physics*, 147(3):034902, 2017. doi: 10.1063/1.4993619

Tamal Roy, Kai Szuttor, Jens Smiatek, Christian Holm, and Steffen Hardt. Electric-field-induced stretching of surface-tethered polyelectrolytes in a microchannel. *Physical Review E*, 96(3):032503, 2017. doi: 10.1103/PhysRevE.96.032503

Tamal Roy, Kai Szuttor, Jens Smiatek, Christian Holm, and Steffen Hardt. Stretching of surface-tethered polymers in pressure-driven flow under confinement. *Soft Matter*, 13: 6189–6196, 2017. doi: 10.1039/C7SM00306D

Chapter 2

Theoretical Background

This chapter contains the basic theoretical framework needed to understand and interpret the results of the studies presented in this work. To this end, the most important concepts of (charged) polymers are introduced in Sec 2.1. In the next section, the properties of DNA are discussed, followed by sections that deal with the technical frameworks that have been applied, namely molecular dynamics (Sec. 2.4), the lattice-Boltzmann method (LBM) (Sec. 2.5) and the finite element method (Sec. 2.6). Finally, the last two sections introduce the electrokinetic transport phenomena electroosmosis and electrophoresis and the electrokinetic equations that describe charged systems by means of partial differential equations.

2.1 Polymers and Polyelectrolytes

Polymers are molecules built up of connected subunits called monomers. They can be found in many products of everyday life, for example rubber, clothing, plastic bags, tires, paints, glue and many more. However, polymers can also be found in many biological systems, *e. g.* proteins like collagen or hemoglobin, carbohydrates like starch, or nucleic acids like DNA and ribonucleic acid (RNA). Polymers with groups that can dissociate in aqueous solution are known as polyelectrolytes. The properties

of polymers depend on the local interaction between monomers but also on the interaction between monomers and the solvent.

The persistence length of polymers defines the length scale on which the bond orientation correlation along the polymer decays and therefore gives a measure for the stiffness of the chain: the shorter the persistence length, the more flexible the polymer is and vice versa. For polyelectrolytes the persistence length additionally depends on the concentration of salt ions in the solution. The higher the concentration of salt, the more the like-charge repulsion between monomers is reduced because of the screening of electrostatic interactions.

The relevant length scale of electrostatic screening is the so-called DEBYE-HÜCKEL screening length which depends on the salt concentration, the valency of the ions and the temperature:

$$\lambda_{\mathrm{D}} = \left(\frac{\varepsilon_0 \varepsilon_r k_{\mathrm{B}} T}{\sum_{i=1}^{N} c_i q_i} \right)^{\frac{1}{2}}, \tag{2.1}$$

where ε_0 is the permittivity of free space, ε_r is the relative permittivity, k_{B} is the BOLTZMANN constant, T the temperature, N the number of charged species, c_i and q_i the density and charge of species i, respectively. This length scale naturally occurs in the linearized POISSON-BOLTZMANN equation that describes the electrostatics of electrolyte solutions.

An important dynamic quantity of interest of polyelectrolytes is the electrophoretic mobility that describes the response of the charged chain to an externally applied electric field. In the linear-response regime the electrophoretic mobility is defined as the ratio of the center of mass velocity and the applied field:

$$\mu = \frac{|\mathbf{v}_{\mathrm{COM}}|}{|\mathbf{E}|}, \tag{2.2}$$

with $|\mathbf{v}_{\mathrm{COM}}|$ the polymer's center of mass velocity and $|\mathbf{E}|$ the magnitude of the applied electric field.

2.2 DNA

Deoxyribonucleic acid (DNA) is known to contain the information for the building blocks of life. This section is therefore dedicated to take a short excursion into the biology of cells in order to explain the role of DNA in the creation of life and provide a broader context for why the DNA molecule is of such a great interest in science and technology.

The DNA molecule is built up by two polynucleotides that form a double helix. Each of the nucleotides is complementary to another: adenine forms pairs with thymine and guanine with cytosine (*cf.* Fig. 2.1). The base pair specific hydrogen bonds as well as steric restrictions imposed by the sugar–phosphate backbones lead to the helical structure of the DNA molecule. On a larger scale the DNA is organized into nucleosomes which

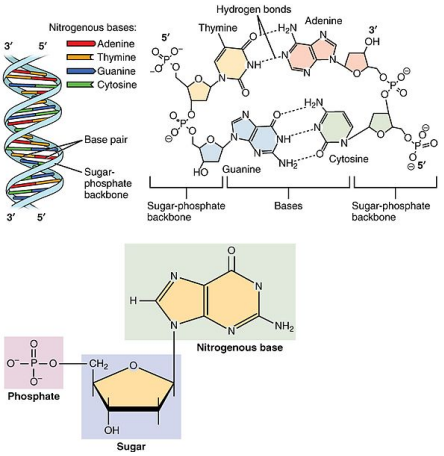

Figure 2.1: The double-helical structure of the double-stranded DNA molecule with its phosphate backbone and the base pairs. Each of the nucleotides has three main chemical groups: the phosphate, the sugar and the base group. Taken from Ref. [92].

are histone octomers around which DNA is wrapped in a spiral. Furthermore, these nucleosomes are wrapped into fibers

with a diameter of about 30 nm. A dense pack of these fibers is called chromatin which in turn form the chromosome on the length scale of micrometers (*cf.* Fig. 2.2). The chromosomes

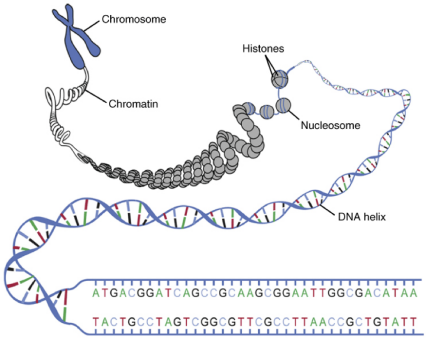

Figure 2.2: The double-stranded DNA is organized into larger structures. It binds to certain proteins (histones) and wraps itself around them. These structures are organized into chromatin and the chromosome upon cell division. Taken from Ref. [92].

in turn live in the nucleus of a cell which contains all the DNA and therefore genetic information of the cell. In such eukaryotic cells the DNA serves as a template for the creation of single stranded messenger RNA (mRNA) molecules. This is the so-called transcription process in which the information from the double-stranded DNA in the nucleus is read and by exploiting the complementary base pairing an enzyme catalyzes the formation of the pre-mRNA molecule which in turn is processed to the final mRNA. This molecule contains the information about a single gene of the DNA. After this transcription process, the mRNA is processed by the ribosome which is a specialized part of the cell. In eukaryotic cells, the mRNA molecules leave the nucleus and are transported to the cytoplasm. In the cytoplasm the ribosomes maps a triplet of base pairs called codon to a single amino acid and the sequence of amino acids form a protein. Proteins in general are the "workhorses" of the cell, performing all sorts of important steps in the life of a cell and therefore life

in the more broad sense. It is important to remember at this point that the origin of the building plan of these proteins is the sequence of base pairs in the DNA molecule.

2.3 DNA origami molecules

The self-assembly of three-dimensional DNA structures exploits the base specific binding mechanisms of DNA to form pre-programmed structures on the nanometer scale. The basic element of such structures are sections of double-stranded DNA with a pre-defined length [93]. A single stranded so-called scaffold strand of up to several thousands bases is folded into more compact bundles that are supported by so-called staple stands to enable the formation of various three-dimensional shapes. With this approach

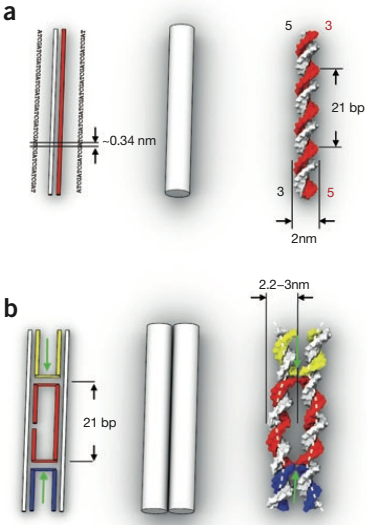

Figure 2.3: The scaffold strand (white) and the (various colors) staple strands. Taken from Ref. [93].

not only single layered structures but also multi-layered DNA as shown in Fig. 2.4 origamis are possible.

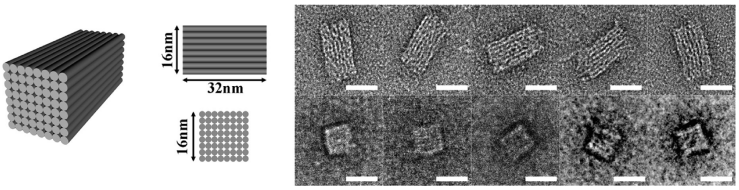

Figure 2.4: An example for a multilayered DNA origami nanostructure. The images on the right have been created with a transmission electron microscope. The scale bars are 20 nm long. Taken from Ref. [94].

2.4 Molecular Dynamics Simulation

Molecular dynamics simulations numerically solve Newton's equations of motion for a system of interacting particles. These particles can either represent a single atom in the case of all-atom simulations or a group of particles in coarse-grained models. Predefined force fields describe the distance dependent non-bonded and bonded interaction potentials between the components. In addition, more complex 3- and 4-body interactions are possible, *e. g.* bond-angle and dihedral potentials.

Since the forces are computed from distance-dependent pair potentials, the most time-consuming part in a simulation is the calculation of all distances between interacting components. The most common integration algorithm is the so-called velocity Verlet algorithm [95]. The Verlet algorithm has two major drawbacks if it is used in numerical simulations:

- in the update of the positions, the term of order Δt^2 is much smaller than the other terms in the sum which leads to numerical imprecision of the algorithm,
- velocity and position is not known at the same time step.

To overcome these drawbacks, the velocity Verlet algorithm was developed by Swope et al. [95]. This update scheme is mathematically equivalent to the aforementioned Verlet scheme

but numerically more stable and the positions and the velocities are available at the same time step :

$$\begin{aligned}\mathbf{r}_i\left(t+\Delta t\right) &= \mathbf{r}_i(t) + \Delta t \mathbf{v}_i(t) + \frac{\Delta t^2}{2m_i}\mathbf{F}_i(t) + \mathcal{O}\left(\Delta t^3\right), \\ \mathbf{v}_i\left(t+\Delta t\right) &= \mathbf{v}_i(t) + \frac{\Delta t}{2m_i}\left[\mathbf{F}_i(t) + \mathbf{F}_i\left(t+\Delta t\right)\right] + \mathcal{O}\left(\Delta t^3\right).\end{aligned} \tag{2.3}$$

Often molecular dynamics simulations of solutes are carried out with an implicit solvent in order to get rid of the huge number of degrees of freedom in the system which result from solute-solvent interactions, thus saving a lot of computational costs. The solvent is then only taken into account in an averaged manner by introducing a friction and a random noise term in the integration scheme.

In molecular dynamics simulations, the LANGEVIN equation is used as a heat bath to keep the temperature constant and therefore simulating the statistics of particles in an NVT-ensemble. The equations of motion are thus extended by a random force leading to the following stochastic differential equation [71]:

$$m_i \frac{\mathrm{d}^2\mathbf{r}_i(t)}{\mathrm{d}t^2} = -\nabla_i U\left(\mathbf{r}_i(t)\right) - \gamma m_i \frac{\mathrm{d}\mathbf{r}_i(t)}{\mathrm{d}t} + \mathbf{R}_i(t), \tag{2.4}$$

where m denotes the mass of the particle, $\mathbf{r}$ the position, U the interaction energy, γ the friction coefficient and $\mathbf{R}$ a random force. The friction coefficient γ and the random force $\mathbf{R}$ are connected by the so-called *fluctuation-dissipation theorem*. This connection originates in the fact that both forces are caused by collisions with solvent particles [96]. The *fluctuation-dissipation theorem* states that if a process exists which turns energy into heat (friction), there has to be a reverse process that turns out to be the thermal fluctuations in LANGEVIN dynamics. Thus, the first two moments of the random force can be expressed as follows:

$$\left\langle \mathbf{R}_i(t) \right\rangle_t = 0, \tag{2.5}$$

$$\left\langle \mathbf{R}_i(t)\mathbf{R}_j(t') \right\rangle_t = 6\gamma k_\mathrm{B} T m_i \delta_{i,j}\delta(t-t'), \tag{2.6}$$

where $k_\mathrm{B}T$ is the thermal energy.

2.5 Lattice Boltzmann Method

The lattice-BOLTZMANN method is a numerical method in the realm of computational fluid dynamics that solves a discretized version of the BOLTZMANN equation on a lattice. It can be shown that this algorithm solves the NAVIER-STOKES equation under the assumption of small Mach numbers and small density variations [97].

The particle density function f in the combined momentum- and position-space is defined such that it satisfies the following equation:

$$N = \int_{\mu} \mathrm{d}^3\,\mathbf{v} \int_{\mu} \mathrm{d}^3\,\mathbf{r} f\left(\mathbf{v}, \mathbf{r}, t\right), \tag{2.7}$$

where N denotes the number of particles in the system at time t.

For velocity independent forces $\mathbf{F}$ acting on the particles the evolution of the density function due to streaming in time can be described by the total differential with respect to time:

$$\frac{\mathrm{d}f}{\mathrm{d}t} = \frac{\partial f}{\partial t} + \mathbf{v} \cdot \nabla_{\mathbf{r}} f + \frac{\mathbf{F}}{m} \cdot \nabla_{\mathbf{v}} f. \tag{2.8}$$

The interaction between the pseudo-particles is described by a collision. The change of the density function f due to collisions is here be denoted by the expression $\left(\frac{\partial f}{\partial t}\right)_{\text{coll}}$. Due to the LIOUVILLE-theorem [98], which states that the phase-space density of a classical system with uncorrelated velocities (*molecular chaos approximation* [99, 100]) is constant over time, the changes of the density function due to streaming have to be balanced by changes caused by collisions:

$$\frac{\partial f}{\partial t} + \mathbf{v} \cdot \nabla_{\mathbf{r}} f + \frac{\mathbf{F}}{m} \cdot \nabla_{\mathbf{v}} f = \left(\frac{\partial f}{\partial t}\right)_{\text{coll}}. \tag{2.9}$$

This equation is known as the BOLTZMANN transport equation (BTE).

In the LBM, the BOLTZMANN-equation (*cf.* Eq. (2.9)) is discretized in the velocity and time space. Velocities are restricted

to a finite set of directions and magnitudes. The BOLTZMANN-equation in this framework reads:

$$\frac{\partial}{\partial t} f_i + \mathbf{v}_i \cdot \nabla f_i = \left(\frac{\partial f_i}{\partial t} \right)_{\text{coll}}, \tag{2.10}$$

where $\mathbf{v}_i \in \{\mathbf{v}_0, \ldots, \mathbf{v}_Q\}$ and $f_i \coloneqq f(\mathbf{v}_i)$ [101]. For the collision operator $\left(\frac{\partial f_i}{\partial t} \right)_{\text{coll}}$ several descriptions exist, differing in the way the modes of the probability density function relax to the equilibrium distribution. For a single relaxation rate λ, the collision operator simplifies to the so-called lattice BHATNAGAR-GROSS-KROOK (LBGK) operator [102]:

$$\left(\frac{\partial f_i}{\partial t} \right)_{\text{coll}} = -\lambda \left(f_i - f_i^{\text{eq}} \right). \tag{2.11}$$

Finally, the LBM equation in the single relaxation time approximation reads:

$$f_i \left(\mathbf{r} + \mathbf{v}_i, t + \delta t \right) - f_i \left(\mathbf{r}, t \right) = -\lambda \left(f_i \left(\mathbf{r}, t \right) - f_i^{\text{eq}} \left(\mathbf{r}, t \right) \right). \tag{2.12}$$

It is possible to calculate macroscopical physical quantities from the discrete equilibrium particle density distributions f_i^{eq}:

$$\begin{aligned}
\sum_i f_i^{\text{eq}} &= \rho, \\
\sum_i f_i^{\text{eq}} v_{i\alpha} &= \rho u_\alpha, \\
\sum_i f_i^{\text{eq}} v_{i\alpha} v_{i\beta} &= \rho c_s^2 \delta_{\alpha\beta} + \rho u_\alpha u_\beta, \\
\sum_i f_i^{\text{eq}} v_{i\alpha} v_{i\beta} v_{i\gamma} &= \frac{\rho}{3} \left(u_\alpha \delta_{\beta\gamma} + u_\beta \delta_{\gamma\alpha} + u_\gamma \delta_{\alpha\beta} \right) + \rho u_\alpha u_\beta u_\gamma,
\end{aligned} \tag{2.13}$$

where Greek indices denote Cartesian coordinates, u the fluid velocity, ρ the fluid density and c_s is a constant that depends on the lattice model.

In the fluid simulation, the lattice-BOLTZMANN (LB) algorithm in general is performed in two steps (the order can vary between different implementations):

- streaming step:
  the populations on each lattice side propagate in the respective velocity direction,

- collision step:
  the collision operator is applied to all lattice sides and the new populations for each of the discrete velocities are updated.

In order to simulate solid boundaries within the LBM framework, the so-called *link-bounce-back* algorithm can be used. If a population of a fluid node gets streamed onto a boundary node, the population is bounced back to the node it came from [103] (see Fig. 2.5).

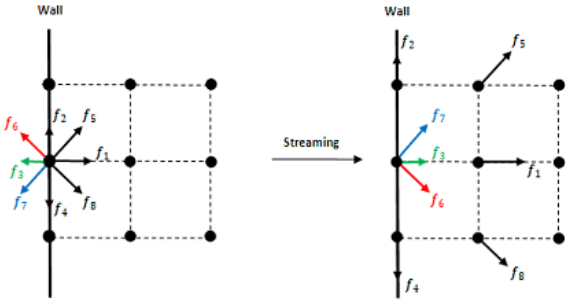

Figure 2.5: Sketch of the *link-bounce-back* boundary condition. Node populations get bounced back from wall nodes which results in a no-slip boundary condition in the mid-plane between fluid and boundary nodes. Taken from Ref. Bao and Meskas [104]

In order to combine the LBM with classical molecular dynamics simulation, the two methods have to be coupled. Ahlrichs and Dünweg proposed a point coupling scheme [105, 106] which exchanges momentum between the fluid and the particle. The fluid velocity $\mathbf{u}$ at the particle coordinate $\mathbf{r}$ is calculated either by two-point or three-point interpolation functions that arise from

the neighboring LBM node velocities. In most applications of coupled LBM/molecular dynamics simulations, the linear two-point coupling is of sufficient precision [106]. The momentum exchange is chosen according to STOKES' friction proportional to the difference of the fluid velocity $\mathbf{u}$ and the velocity $\mathbf{v}(\mathbf{r})$ of the particle. Therefore, the force $\mathbf{F}_{\text{particle}}$ on the particle mediated by the fluid reads:

$$\mathbf{F}_{\text{particle}} = -\zeta \left(\mathbf{v} - \mathbf{u} \right), \tag{2.14}$$

where ζ is the friction coefficient. To ensure momentum conservation, the respective force density is also applied to neighboring lattice nodes.

2.6 Finite Element Method

The Finite element method (FEM) is used to numerically solve partial differential equations that naturally occur in many fields of engineering and physics. The simulation domain is discretized via a mesh which leads to an approximation of the governing differential equations in the respective simulation domain with its boundary conditions. Describing the (often) complex geometry of the domain by smaller fragments simplifies finding a solution for the overall domain by treating each fragment independently [107]. These fragments give the methods its name, these fragments are the finite elements. Each of the finite elements is treated as an independent domain for which the partial differential equations are solved for. Of course the representation of the geometry may not be exact and already at this point a systematic error is introduced, although it might be small if the segmentation of the domain is done carefully.

In the next step, the unknown quantities are represented by a linear combination of polynomials: $X = \sum_i c_i \Phi_i$, where c_i are coefficients to be determined and Φ_i are the polynomial functions. The degree of the polynomial also dictates how man subdivisions per element are necessary: a linear polynomial only needs two nodes whereas a quadratic polynomial needs three nodes and so on. The coefficients for the polynomials have to

be determined such that the approximations for the unknowns satisfy the differential equations of interest at the nodes in an approximate way [107]. Therefore, the approximate solution is found by first expressing the differential equation in the so-called weak form.

The POISSON equation for electrostatics shall serve as an example. In one dimension it reads:

$$-\frac{d}{dx}\left(\varepsilon(x)\frac{d\phi(x)}{dx}\right) = \rho(x), \tag{2.15}$$

where ε is the dielectric constant, ϕ the electrostatic potential and ρ the charge density. The domain of interest is $0 \leq x \leq L$ with the boundary conditions $\phi(0) = \phi_0$ and $\left(\varepsilon(x)\frac{d\phi(x)}{dx}\right)_{x=L} = C$. The quantity of interest in this case is the electrostatic potential in the domain which will be approximated by polynomials:

$$\phi(x) \approx \phi_N(x) = \sum_i c_i \Phi_i(x) + \Phi_0(x). \tag{2.16}$$

The approximation for the electrostatic potential leads to a difference between the left and the right-hand side of Eq. (2.15), the so-called residual:

$$R = -\frac{d}{dx}\left(\varepsilon(x)\frac{d\phi_N}{dx}\right) - \rho(x). \tag{2.17}$$

There are several measures that can be used to define the quality of the approximation that results from the respective coefficients c_i of the polynomials. A commonly chosen way is to find coefficients c_i such that integrals over the domain for the weighted residual vanish:

$$\int_0^L w_i(x) R(x, c_i) = 0, \tag{2.18}$$

where $w_i(x)$ are the weight functions. The (often used) so-called GALERKIN method uses the polynomials of the approximation as the weight functions, such that $w_i = \Phi_i$. The condition in Eq. (2.18) is the so-called weighted integral form. This form

requires Φ_i to be chosen such that the resulting approximate representation of the electrostatic potential is differentiable as often as demanded by the POISSON equation while respecting the boundary conditions.

There is another approach that makes it easier to incorporate boundary conditions and weakens the demands on the differentiability of the electrostatic potential approximation. It is therefore called the weak form of the problem statement and is derived in the following for the case of the POISSON equation. Starting from the integral statement, integrating by parts yields:

$$\begin{aligned} 0 &= \int_0^L \left(w_i(x) \left(-\frac{d}{dx} \left(\varepsilon(x) \frac{d\phi(x)}{dx} \right) \right) - w_i(x)\rho(x) \right) dx \\ &= \int_0^L \left(\varepsilon(x) \frac{dw_i(x)}{dx} \frac{d\phi(x)}{dx} - w_i(x)\rho(x) \right) dx \\ &\quad - \left[w_i(x)\varepsilon(x) \frac{d\phi(x)}{dx} \right]_0^L . \end{aligned} \tag{2.19}$$

Note, that now the boundary condition for the electric flux explicitly occurs in the problem statement. Another important advantage of this representation is the fact that the electrostatic potential now has to only be differentiable once and not twice (as in the case of the weighted integral approach). The weight functions w_i have to vanish at $x = 0$ since the potential is explicitly defined and may not be changed by any weight at this boundary. Thus, Eq. (2.19) yields:

$$\int_0^L \left(\varepsilon(x) \frac{dw_i(x)}{dx} \frac{d\phi(x)}{dx} - w_i(x)\rho(x) \right) dx = w_i(L)\varepsilon(L) \left. \frac{d\phi(x)}{dx} \right|_{x=L} , \tag{2.20}$$

which is termed the weak form of Eq. (2.15). In order to numerically solve the weak form, a suitable discretization has to be used (as described above). After applying the discretization, the weak form can be represented as $\mathbf{A}\phi_\mathbf{N} = \mathbf{b}$, where A is an NxN matrix containing the coefficients for $\phi_\mathbf{N}$ and $\mathbf{b}$ contains

the charge density portion of the POISSON equation. Note that, depending on the basis functions that are used for the discretization, the coefficient matrix is often very sparse. This system of equations can now be solved numerically.

2.7 Electroosmosis and Electrophoresis

Electroosmosis describes the electrokinetic transport phenomenon that is observed if a charged surface is in contact with an electrolyte solution and an external electrostatic potential gradient is applied.

Consider a planar charged surface as depicted in Fig. 2.6. The blue rectangle represents the charged surface whereas the density of the counter-ions in the electrolyte is shown in shades of red. The mobile ions in the vicinity of the charged surface form a double layer. This layer carries a net charge that is driven by the electric field. In addition, the driven layer of ions pushes the surrounding fluid along which results in a velocity profile as shown in white in Fig. 2.6. The length-scale on which the electrostatic potential in the counter-ion layer decays is the DEBYE length (*cf.* Sec. 2.1). The resulting velocity profile of the fluid is [108]:

$$v_x(y) = \frac{\varepsilon}{4\pi\eta}\left(\Psi(y) - \zeta\right)\tilde{E}_z, \tag{2.21}$$

where ε is the dielectric constant of the fluid (≈ 80 for water at room temperature), η is the dynamic viscosity of the fluid, Ψ is the electrostatic potential depending on the distance to the charged surface, ζ is the electrostatic potential at the charged surface and $\tilde{E}_z$ is the electric field at $y = \lambda_\mathrm{D}$. Far away from the charged surface the flow is parallel to the surface (plug flow). Therefore, the velocity in the bulk v_x^bulk can be obtained from Eq. (2.21) for a vanishing electrostatic potential Ψ:

$$v_x^\mathrm{bulk} = -\frac{\varepsilon}{4\pi\eta}\zeta\tilde{E}_z \tag{2.22}$$

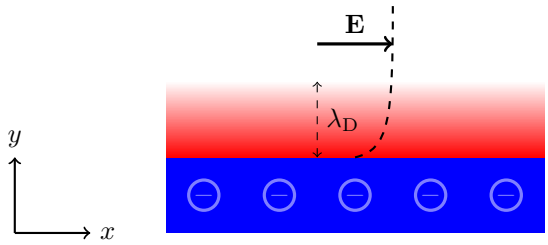

Figure 2.6: A planar charged surface in contact with an electrolyte solution under an externally applied electric field $\mathbf{E} = E\hat{\mathrm{e}}_x$.

Electrophoresis on the other hand describes the motion of a charged object through a fluid caused by an externally applied electric field. Again, the charged object's charge is screened by mobile ions in the fluid. The externally applied electric field also exerts a force on the counter-ion cloud. The resulting force on the counter-ions points in the opposite direction as the force on the charged object. The portion of the force on the ions that is transferred onto the particle via the fluid is called retardation force. In addition, there is a so-called relaxation effect of the counter-ion cloud due to the movement of the charged object that causes a deformation of the ionic double layer. The electrophoretic mobility μ of a charged object is then defined as the ratio of the steady state velocity v in direction of the external field and the amplitude of the applied electric field E:

$$\mu = \frac{v}{E}. \tag{2.23}$$

2.8 Electrokinetic equations

This section introduces the basic theoretical framework that is used to describe the DNA nanopore systems on a mean-field level. More specific descriptions of the modeling and adaptions of the equations introduced in this section can be found in the model description in Sec. 3.3.

The electrostatic potential $\Psi(\mathbf{r})$ of a charge density $\rho(\mathbf{r})$ can be calculated from the POISSON equation (plus boundary conditions):

$$\nabla \cdot \big(\varepsilon_0 \varepsilon_r(\mathbf{r}) \nabla \Psi(\mathbf{r})\big) = -\rho(\mathbf{r}) = -e \sum_i z_i c_i(\mathbf{r}), \tag{2.24}$$

with ε_0 being the permittivity of free space, $\varepsilon_r(\mathbf{r})$ the relative permittivity of the medium containing the ions, z_i the valency of the ionic species i and c_i the number density of species i.

On the mean-field level ion transport can be modeled by means of the so-called NERNST-PLANCK equation:

$$\nabla \cdot \big[-D_i \nabla c_i(\mathbf{r}) - \mu_i z_i e c_i(\mathbf{r}) \nabla \Psi(\mathbf{r}) + c_i \mathbf{u}(\mathbf{r})\big] = 0, \tag{2.25}$$

where D_i is the diffusion constant of ion species i, c_i the concentration, μ_i the mobility, Ψ the electrostatic potential and $\mathbf{u}$ the solvent velocity. Note that the ion mobility μ and the ion diffusivity D is connected via the Einstein relation: $D_i = \mu_i k_\mathrm{B} T$. The NERNST-PLANCK equation is an extension to FICKIAN diffusion which is based on conservation laws that describe the mass conservation of the ionic species in every infinitesimally small volume taking into account the different kinds of fluxes that may be present in the system. First, there is the diffusive flux due to concentration gradients:

$$j^i_\mathrm{diffusive} = -D_i \nabla c_i(\mathbf{r}). \tag{2.26}$$

The ion's concentration tends to a homogeneous distribution due to thermal motion (BROWNIAN motion). Second, there is the migration of ions caused by an electric field $E(\mathbf{r})$:

$$j^i_\mathrm{migration} = -\mu_i z_i e c_i(\mathbf{r}) \nabla \Psi(\mathbf{r}) = \mu_i z_i e c_i(\mathbf{r}) E(\mathbf{r}). \tag{2.27}$$

The migration term describes the ionic flux caused by electrophoretic forces originating from electric fields acting on the charged species. The third kind of flux describes the advection with the fluid: $j^i_{advective} = c_i \mathbf{u}(\mathbf{r})$. Here, the ionic flux is caused by the fluid flow velocity of the underlying solvent.

The steady state description of an incompressible ($\nabla \cdot \mathbf{u}(\mathbf{r}) = 0$) fluid flow under the influence of an external driving force $\mathbf{f}$ can be described by STOKES' equation:

$$-\eta \nabla^2 \mathbf{u}(\mathbf{r}) = \mathbf{f}(\mathbf{r}), \tag{2.28}$$

where η is the dynamic viscosity. This equation describes the flow well under the assumption of low REYNOLDS numbers, *i. e.* in systems where viscous forces are dominant compared to inertial forces: $\mathrm{Re} = \rho u L/\mu \ll 1$, with ρ being the fluid density and L a characteristic length scale of the respective geometry.

In order to couple electrostatic effects and the fluid flow, the effect of momentum transport between ions and the fluid has to be taken into account. Therefore, the driving force $\mathbf{f}(\mathbf{r})$ in Eq. (2.28) has to include the frictional forces that arise from ions moving either due to diffusion or an external electric field:

$$\mathbf{f}(\mathbf{r}) = \sum_i \frac{j^i_{\text{diffusive}} + j^i_{\text{migration}}}{\mu_i}. \tag{2.29}$$

In summary, this leads to a system of partial differential equations that can be solved for a specific geometry and given boundary conditions numerically.

MD Software — ESPResSo

All coarse-grained simulations in this work have been performed with the molecular dynamics software ESPResSo (`https://espressomd.org`) [109, 110, 111, 84]. ESPResSo's key features are:

- has a node parallel C++ core (backend),
- has a Python scripting interface (frontend),
- is able to couple molecular dynamics to a LB hydrodynamics solver,
- contains implementations of solvers for long-range electrostatic interactions (in particular the $\mathrm{P^3M}$ algorithm [112]).

The combination of the key features listed above renders this software an ideal and flexible tool to investigate the physics of charged soft matter via molecular dynamics simulations. While the backend of ESPResSo is implemented in a node-parallel fashion using message passing interface (MPI) and is therefore capable of handling large-scale systems on highly parallel hardware (*i. e.* compute clusters), the software is mostly used because of the unique set of the aforementioned features plus the enormously flexible frontend. Thus, compared to other molecular dynamics software like GROMACS [113] or LAMMPS [114, 115] the focus of ESPResSo is more on flexibility than on performance.

The following short sample script shows the flexibility of having a python interface to the molecular dynamics backend in ESPResSo:

```
import numpy as np

import espressomd

system = espressomd.System(box_l=[10.0] * 3)
system.part.add(pos=np.random.random((100,3)) * system.box_l)
system.part[::2].q = 1.0
system.part[1::2].q = -1.0
system.non_bonded_inter[0,0].lennard_jones.set_params(sigma=1.0, epsilon=1.0, cutoff
      =2**(1./6.), shift="auto")
```

Listing 2.1: ESPResSo code sample. (Tested with commit hash 3e2674a8f2b193b32c404dd4cab633cd8c5c76a3).

The listing above gives an idea how a simulation is built up step by step and how the user can interact with the components at each stage of the simulation:

- a simulation domain is initialized with size 10 in all directions
- 100 particles with random positions in the domain are added
- half of the particles get a positive, the other half a negative electrostatic charge assigned
- a non-bonded interaction is added.

This bare minimum example already demonstrates the flexibility compared to static parameter files (*e. g.* in the case of GROMACS).

2.9 Resistive pulse sensing

Sensing molecules using nanopores is based on the modulation of the ionic current in a setup where two electrolyte reservoirs are connected by a nanopore (*cf.* Fig. 2.7). This technique is known as *resistive pulse sensing* or as a COULTER-counter. The field of nanopore based molecule detection and analysis has shown growing interest in the soft matter scientific community in the last years. The basic idea dates back to the late 1940s when Wallace Coulter [2] invented a device to count red blood cells. An electric field causes a steady ionic current and at the same time drives charged particles or molecules through the nanopore. During the translocation of the analyte a salt-dependent ionic current modulation can be observed. Such systems were used to study a range of analytes from DNA and proteins to viruses [9, 10, 12]. Depending on the ratio between the pore diameter and the analyte the signal-to-noise (SNR) ratio may be adjusted and thereby the temporal and spatial resolution of the sensing setup. However, also the translocation speed of the analyte plays a crucial role for the SNR [116].

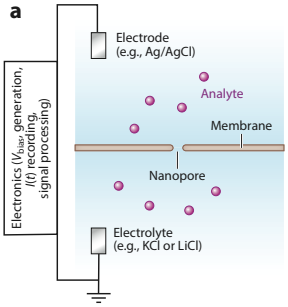

Figure 2.7: A schematic view on a resistive pulse sensing setup. Taken from Ref. [13].

Chapter 3

Models for DNA nanopore systems

In this chapter we describe the investigated simulation models for the DNA structures with different levels of detail. The first section 3.1 contains the model parameters for the DNA models used in the all-atom molecular dynamics simulations. In Sec. 3.2 we describe the coarse-grained DNA models. Finally, the last section 3.3 deals with the DNA model on the mean-field level.

3.1 All-atom DNA models

This section contains the all-atom models for double-stranded DNA (dsDNA), a dsDNA origami and a quad formation of dsDNA in an infinite cylindrical pore that has been investigated via molecular dynamics simulations.

Infinite pore model

The model described in the following is mostly inherited from Ref. [47], details have been adopted in order to make the setup compatible with a more recent release of the simulation package GROMACS [113], namely the 2018 release. It served as a reference model with known results to compare to and to make

sure that the data analysis implementation (that will also be used for other all-atom models) is valid. The all-atom model for dsDNA is a homo-polymer build up of 20 stacked cytosine-guanine base pairs. In order to reduce end effects of the finite DNA molecule it is periodically connected along the axis of the helix. A cylindrical pore is constructed by two layers of particles with a generic Lennard-Jones interaction (*cf.* Sec. 2.4) with a diameter of 0.5 nm, a Lennard-Jones interaction strength of $5.0\,\mathrm{kJ\,mol^{-1}}$ and a gap of 0.5 nm between adjacent pore particles. The simulation domain is constrained to a rectangular box with dimensions of $L_x = 15\,\mathrm{nm}$, $L_y = 15\,\mathrm{nm}$, $L_z = 6.67\,\mathrm{nm}$ and periodic boundary conditions along the z axis. To compensate for the charged backbone of the dsDNA molecule of $2\,e$ per base pair, 40 potassium ions have been added to the system. Between 16 and 144 excess salt ion pairs have been added to simulate different electrolyte reservoir concentrations. The respective bulk salt concentrations have been estimated from radial ion density profiles *a posteriori*. With the given range of excess ion pairs, this resulted in bulk electrolyte concentrations ranging from $0.07\,\mathrm{mol\,l^{-1}}$ to about $0.6\,\mathrm{mol\,l^{-1}}$. Following Ref. [47], the phosphorous atoms' and the pore particles' positions have been restrained via a harmonic potential with a strength of $1000\,\mathrm{kJ\,mol^{-1}\,nm^{-1}}$. After water molecules had been added, an external electric field of $0.2\,\mathrm{V\,nm^{-1}}$ is applied along the symmetry axis of the helix.

For the dsDNA the AMBER03 force field [117] and for the ions a force field optimized for correct dynamics [118, 119, 120] has been used. The water molecules are represented with the so called SPC/E water model [121]. Bonds between the dsDNA molecule and hydrogen atoms were fixed and the temperature of the system was held constant via a stochastic velocity rescaling approach. Further details of the simulation parameters can be found in the Appendix Sec. 8.1.

DNA origami model

The model description in this section is part of the following publication:

Kai Szuttor, Florian Weik, Jean-Noël Grad, and Christian Holm. Modeling the current modulation of bundled DNA structures in nanopores. *The Journal of Chemical Physics*, 154(5):054901, 2021. doi: 10.1063/5.0038530

The basis of our all-atom model is a structure file of the DNA origami provided to us by the Keyser group[1] who did the experimental work motivating this study [31]. We extracted a periodically recurring segment of the origami and placed it in a rectangular simulation box with periodic boundary conditions to create an infinite origami that reproduced the shape of the original structure, using bonded interactions across the unit cell. We added a cylindrical pore wall built up of atoms with a purely repulsive interaction potential. Similarly to the single DNA setup, the dsDNA origami's phosphorus atoms as well as the pore atoms have been fixed in space via a harmonic potential. We solvated the molecule in water and compensated the net charge by an appropriate amount of potassium counter-ions. To simulate different bulk salt concentrations we exchanged a varying number of water molecules with potassium chloride ion pairs. The bulk salt concentrations have been estimated *a posteriori* from the charge density profiles. The all-atom simulations have been performed with the molecular dynamics software GROMACS version 2020.3 [113].

Details of the procedure of setting up the periodic chunk of the origami molecule can be found in the Appendix section. In the visualization of the simulated molecule in Fig. 3.1 the inter-helix staple strands that stabilize the origami structure are visible.

Quad DNA model

The model description in this section is part of the following publication:

[1] Prof. Dr. U. F. Keyser

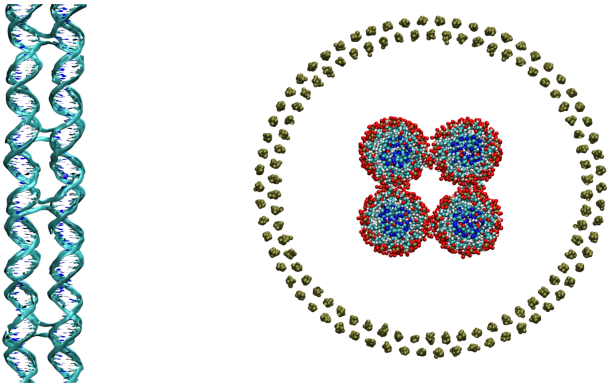

Figure 3.1: The side view (left) and cross-section (right) of the all-atom origami molecule section in a pore. For clarity the water molecules have been excluded.

Kai Szuttor, Florian Weik, Jean-Noël Grad, and Christian Holm. Modeling the current modulation of bundled DNA structures in nanopores. *The Journal of Chemical Physics*, 154(5):054901, 2021. doi: 10.1063/5.0038530

This model is constructed by placing four parallel strands of the dsDNA described in Sec. 3.1 parallel to each other on a 2x2 lattice. The secondary structure of this model is very similar to the actual all-atom origami model described above. The main differences are the missing interconnecting staple strands (Fig. 3.2). Each of the four helices consists of 20 CG base pairs which corresponds to two full turns of the helix. All other simulation parameters are adopted from the model above.

3.2 Coarse-grained DNA models

Existing three-bead model

The following model description is mainly inherited from Ref. [76] and the first version of this model was first published in Ref. [52].

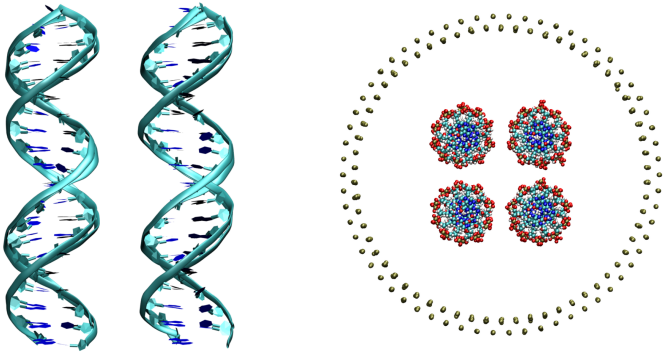

Figure 3.2: Side view (left) and cross-section (right) of the simulated all-atom quad molecule in a pore.

However, during the verification of the model with more recent versions of the simulation software and a full transcription of the model from a deprecated interface scripting language, some parameters were adapted to reproduce static and dynamic results from all-atom simulations.

This DNA model is based on a much coarser representation of the base pairs as compared to the previously discussed all-atom models of Sec. 3.1. Several atoms are combined into a single bead which combines the lower-level interactions into a single effective interaction that is tuned to reproduce structural and dynamical data from all-atom simulations. A single coarse-grained nucleobase pair consists of three beads: two beads represent the phosphate backbones of the two strands and the third bead replaces the connecting nucleobase pair atoms, *cf.* Fig. 3.3b.

This three-bead base pair is simulated as a rigid body, so there are only six degrees of freedom for its center of mass. The distance between the backbone beads and the base pair bead is set to $R_{\mathrm{bb}} = 7.9\,\text{Å}$ and the angle between the connecting lines of base pair and backbone beads is $\phi_{\mathrm{bb}} = 144°$ (*cf.* Fig. 3.3b). Together with the dsDNA model, an ion model has been adopted based on the simple assumptions of charged hard spheres, the so-

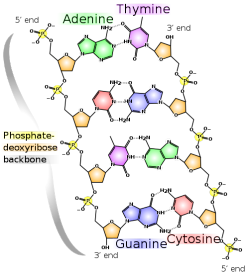

(a) Illustration of a short dsDNA segment, taken from https://commons.wikimedia.org/wiki/File:DNA_chemical_structure.svg, visited at 21.04.2021.

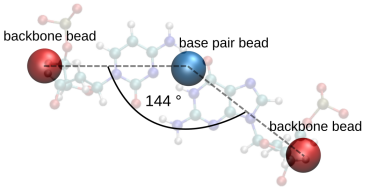

(b) Visualization of a single base pair as it is modelled by the coarse-grained model.

called restricted primitive model [122]. The short-ranged non-bonded interactions between ions and dsDNA beads as well as ions and ions are described by a Lennard-Jones like interaction potential of the following form:

$$V_{\mathrm{LJ}}(r) = \begin{cases} 4\varepsilon \left[\left(\frac{\sigma}{r - r_{\mathrm{off}}} \right)^{12} - \left(\frac{\sigma}{r - r_{\mathrm{off}}} \right)^{6} + c_{\mathrm{shift}} \right], & \text{if } r_{\mathrm{off}} < r < r_{\mathrm{cut}} + r_{\mathrm{off}} \\ 0, & \text{else,} \end{cases} \tag{3.1}$$

where r is the distance between two interacting particles, ε is the interaction strength in units of $k_{\mathrm{B}}T$, and r_{off} and c_{shift} add an offset in r or a shift in V, respectively. For the interaction between two ions, the attractive part of Eq. (3.1) is not used, but instead the so called Weeks-Chandler-Andersen interaction (WCA). The WCA interaction uses a cutoff distance of $r_{\mathrm{cut}} = 2^{\frac{1}{6}}\sigma$ which is the location of the minimum of the attractive portion. Together with the appropriate shift c_{shift} to zero at r_{cut}, this potential serves as a purely repulsive hard sphere potential. Due to the fact that the exact parameters for the dsDNA-ion interaction parameters have changed over the course

of the model improvement, a summary of the parameters is listed in Table 3.1. In all non-bonded interactions between ions and the DNA molecule the shift in the potential c_{shift} has been chosen such that the potential vanishes at the cutoff distance (r_{cut} is set to 2.5 $\sigma + r_{\text{off}}$).

Table 3.1: Non-bonded interaction parameters of the coarse-grained model for the interaction between ions and dsDNA beads. The particle diameter σ is set to 4.25 Å in all cases. Abbreviations used: BB for backbone, BP for basepair.

publication	ε ion BB	r_{off} ion BB	ε ion BP	r_{off} ion BP
Weik *et al.* [52]	$k_{\text{B}}T$	2.9 Å	0.75 $k_{\text{B}}T$	0.06 Å
Rau *et al.* [76]	$k_{\text{B}}T$	0.0	$k_{\text{B}}T$	0.75 Å
this work	$k_{\text{B}}T$	0.0	$k_{\text{B}}T$	0.75 Å

The first version of the dsDNA model as published in [52] did not include any bonded interactions since it has only been used as rigid body model in the limit of time-scale separation of the dsDNA's and ion's dynamics where the dsDNA has therefore been fixed in space.

In the improved model as published in [76], two-, three- and four-body interactions have been added. First, a harmonic bond potential between the base pair bead of every segment has been added (*cf.* Fig. 3.4a):

$$V_{\text{harmonic}}(r) = \frac{1}{2} K_{\text{harmonic}} \left(r - R_{\text{basepair}}\right)^2 , \tag{3.2}$$

where $K_{\text{harmonic}} = 200\ \frac{k_{\text{B}}T}{\sigma^2}$ defines the strength of the bonded interaction and $R_{\text{basepair}} = 3.4$ Å is the equilibrium distance. The value for R_{basepair} has been taken from experimental data in Ref. [123].

Second, a bond-angle potential is defined to control the persistence length of the dsDNA (*cf.* Fig. 3.4b) and another bond-angle potential stabilizes the angle between the backbone and the base pairs (*cf.* Fig. 3.4c). The bond-angle potentials are in structure similar to the harmonic potential for the distance, but

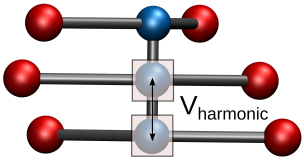

(a) The harmonic bonded potential between backbone beads.

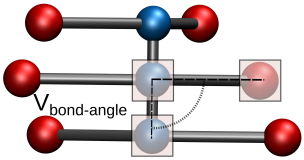

(b) The bond angle harmonic potential on the backbone beads.

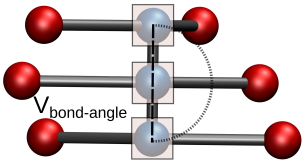

(c) The bond angle harmonic potential on the base pair beads.

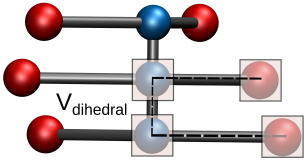

(d) The dihedral angle potential.

Figure 3.4: A three base pair sequence of the coarse-grained model with marked interaction partners for the four different interactions as defined in [76].

depend on the difference to a given equilibrium angle:

$$V_{\text{bond-angle}} = \frac{1}{2} K_{\text{BB/BP}} \left(\phi - \phi_{\text{BB/BP}}\right)^2 , \tag{3.3}$$

where $K_{\text{BB/BP}} = 100\ \frac{k_B T}{\sigma^2}$ again defines the interaction strength and $\phi_{\text{BB/BP}}$ is the equilibrium angle for the case of the backbone (*cf.* Fig. 3.4b) or base pair (*cf.* Fig. 3.4c) interaction, respectively. The equilibrium angles are set to $\phi_{\text{BB}} = \pi$ and $\phi_{\text{BP}} = \frac{\pi}{2}$. The dihedral potential is defined as

$$V_{\text{dihedral}} = K_{\text{dihedral}} \left[1 - \cos(\phi - \phi_{\text{dihedral}})\right] \quad , \tag{3.4}$$

where $K_{\text{dihedral}} = 200 \frac{k_B T}{\sigma^2}$ and $\phi_{\text{dihedral}} = 34.3°$.

In order to incorporate hydrodynamic interactions the beads are coupled to a LB fluid. The coupling is implemented following

Weik *et al.* [52] Thus, the drag force of the fluid applied to a particle is defined by

$$\mathbf{F}_{\text{fric}} = -\gamma \left[\mathbf{v} - \mathbf{u}(\mathbf{r})\right], \tag{3.5}$$

where $\mathbf{v}$ is the particle velocity, $\mathbf{u}$ denotes the bilinear interpolation of the fluid velocity at the particle position $\mathbf{r}$, and γ is a frictional coupling constant. A stochastic thermostat is added in a momentum conserving fashion that fulfills the fluctuation dissipation theorem. The hydrodynamic radius r_{h} is calculated using Stokes' law and the mobility of an isolated particle $\mu = (6\pi\,\eta\,r_{\text{h}})^{-1}$ using

$$\frac{1}{r_{\text{h}}} = \frac{6\pi\,\eta}{\Gamma} + \frac{6\pi\,g}{a}, \tag{3.6}$$

where η denotes the dynamic viscosity, a denotes the grid constant of the LB method, and g is a numerical factor that depends on the implementation and takes in our implementation the value $g = 0.04$ [124, 106].

Quad DNA model

The model description in this section is part of the following publication:

> Kai Szuttor, Florian Weik, Jean-Noël Grad, and Christian Holm. Modeling the current modulation of bundled DNA structures in nanopores. *The Journal of Chemical Physics*, 154(5):054901, 2021. doi: 10.1063/5.0038530

We followed the modeling strategy for a coarse-grained model of a dsDNA molecule as described in Sec. 3.2. In order to extend the model to reproduce the geometry of a 2x2 origami molecule we created a fixed arrangement of four parallel dsDNA strands (*cf.* Fig. 3.5). Simulations have been performed with the release 4.0 of the MD software ESPResSo [84].

The segments of the coarse-grained dsDNA consist of a rigid arrangement of three beads (two for the backbone and one for

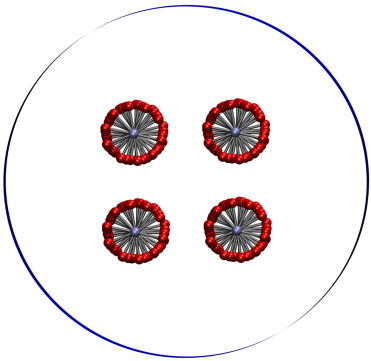

Figure 3.5: Visualization of the origami geometry for the coarse-grained model.

the base pair). A scheme for a single base pair is shown in Fig. 3.3b. Hydrodynamic interactions are included by coupling molecular dynamics with a LB hydrodynamics solver. Using the point coupling scheme [124, 106] to exchange momentum between particles and the LB fluid, a nonphysical fluid flow as observed along the grooves of the helix [52] which is suppressed with additional beads that only interact with the fluid and are part of the rigid body of each segment. To match the distance dependent ion mobility in the vicinity of the DNA observed in all-atom simulations [47], a frictional coupling force $\mathbf{F}_{ij}$ is added between the backbone particles and the ions:

$$\mathbf{F}_{ij} = \begin{cases} -\zeta \left(1 - \frac{r_{ij}}{r_\mathrm{c}}\right)^2 \mathbf{v}_{ij}, & r_{ij} \leq r_\mathrm{c} \\ 0, & \text{else,} \end{cases} \tag{3.7}$$

where $\zeta = 1.43 \times 10^{-13}\,\mathrm{kg\,s^{-1}}$ is a frictional constant, r_{ij} is the inter-particle distance between DNA bead and ion, r_c is the cut-off radius up to which the frictional interaction is enabled, $\mathbf{v}_{ij}$ is the relative velocity. The two free parameters ζ and r_c are tuned to match the ion velocity profile of the respective all-atom simulation for a single salt concentration. In addition to the frictional force, a random force according to the fluctuation-

dissipation theorem is applied. Details of the model can be found in Ref. [76], exact values for all parameters are listed in below.

Table 3.2: Summary of pair interaction parameters.

interaction pair	σ[Å]	$\epsilon[k_\mathrm{B}T]$	$r_\mathrm{cut}[\sigma]$	$r_\mathrm{off}[\sigma]$
ion-ion	4.25	1	$2^{\frac{1}{6}}$	0.0
ion-pore	4.25	1	$2^{\frac{1}{6}}$	0.0
ion-backbone	4.25	1	$2^{\frac{1}{6}}$	0.0
ion-basepair	4.25	1	$2^{\frac{1}{6}}$	0.18

Transcription of Tcl implementation

Since the development of the first version of the coarse-grained model, the scripting interface of the simulation software ESPResSo has switched from Tcl to a modern Python interface. Because not only the interface of the software has changed over time, but also the underlying simulation core has been refactored, a transcription of such a simulation model is therefore non-trivial. This made it mandatory to come up with a more elaborate and rigorous testing of the simulation script itself. We have, therefore, moved the actual setup of the individual particles and their corresponding bonded interactions to a python module that mocks the behavior of the simulation backend (ESPResSo) which makes it possible to test the model independently of the simulation package. Details can be found in Sec. 8.3 in the Appendix.

3.3 Mean-field model

The model description in this section is part of the following publication:

> Florian Weik, Kai Szuttor, Jonas Landsgesell, and Christian Holm. Modeling the current modulation of dsDNA in nanopores – from mean-field to atomistic and back. *Eu-*

ropean Physical Journal Special Topics, 227(14):1639–1655, 2019. doi: 10.1140/epjst/e2019-800189-3

Infinite pore model

The atomistic simulations demonstrated that the mobility of the K^+ ions is reduced close to the DNA surface [47]. The mobilities are normalized to the respective bulk mobilities at their bulk concentration to account for the well-known concentration dependence of the bulk mobility [125]. These normalized mobilities show a common radial profile for all concentrations and result in a current reduction. Furthermore, it was possible to quantify the current contributions from the additional and expelled ions. It could be shown that, taken together, the expelled ions were always overcompensated by the additional ions brought in by the DNA's surface charge. This changes the overall interpretation of the current blockade: It is not a balance between additional and expelled ions, but between additional charge carriers and the friction losses. This is different from the models by Smeets et al. [126], which considered the ions expelled from the pore as the primary effect governing the current reduction, and by van Dorp [54], who did not explicitly include the modified ion friction close to the DNA but rather assumed a constant mobility.

The resulting currents as a function of concentration can be inspected in Fig. 4.13, which also includes the experimental data. The all-atom data fits the experimental data well. Especially the so-called cross-over concentration, *i. e.*, the salt concentration at which the ionic currents with and without DNA are equal, is in good agreement with experimental data. We want to stress here that the force fields have not been fine-tuned for the specific application, nor have Kesselheim *et al.* [47] looked for particular combinations of force fields that yielded the best fit to experimental data. However, the exact physical cause of this mobility reduction still is not quite obvious. Potential explanations include electrofriction [127] and hydrodynamic interactions with the complicated geometry of the DNA surface [128].

Since the strength and spatial dependence of this friction can be quantified and extracted from the all-atom simulation data,

we used this information and incorporated it in terms of a suitably parametrized friction term in a coarse-grained molecular dynamics model. This route was already followed successfully in Ref. [52]. There, the electrolyte as well as the DNA molecule were significantly coarse-grained: The water molecules were replaced by a LB fluid, which drastically reduces the number of degrees of freedom while keeping the salt ions as explicit particles. The level of detail of the DNA molecule was reduced by representing each base pair as one rigid body composed of three beads. This allowed removing most of the chemical detail of the molecule while preserving its double-helix structure. To reflect the mobility reduction observed in the atomistic simulations, a dissipative force $\mathbf{F}^D$ between the salt ions and the DNA of the following form was introduced:

$$\mathbf{F}_{ij}^D = -\alpha\omega(r_{ij})\mathbf{v}_{ij}. \tag{3.8}$$

Here, $\omega = \omega(r)$ is a distance-dependent weight function for the friction with

$$\omega(r) = \begin{cases} \left(1 - \frac{r}{r_c}\right)^2 & \text{if } r < r_c \\ 0 & \text{else,} \end{cases} \tag{3.9}$$

where r_c is the cut-off value for the friction, $\mathbf{v}_{ij}$ and r_{ij} the relative velocity and distance between the ions and the beads of the DNA model, and α is a constant parameter characterizing the strength of the friction. With this friction term, the current modulation observed in experiment and the all-atom studies could be reproduced with the coarse-grained model. This coarse-grained model could also be developed into a fully flexible model which reproduced all the electrokinetic properties of finite length dsDNA fragments, like the salt dependence of the persistence length, and the electrophoretic mobility as function of the number of base pairs [76].

Here, we follow a new continuum approach where we incorporate a suitably parametrized friction term to the continuum electrokinetic model by applying a simple force balance argument for the ions. As we will show, this enables us to reproduce the current modulation observed in experiments on a

mean-field level, which opens up doors for a fast exploration of the parameter space, for example, when displacing the DNA or inserting more complicated macromolecular objects like DNA origami[129]. DNA origami molecules are tailored DNA strands that can be designed to self-assemble into any desired shape. Keyser *et al.* attached specific DNA origami onto glass nanopores, trapping it at the tip of the nanocapillary to modify, *e. g.*, its sensitivity for single stranded DNA (ssDNA) detection [130, 131]. As a natural consequence we ask for the influence on the current modulation of DNA origami inserted into a nanopore.

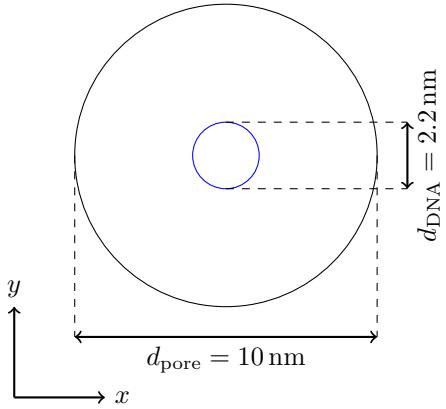

Figure 3.6: Sketch of the continuum model in 2D. The dsDNA (blue contour) is modeled as a charged cylinder within an uncharged cylinder that represents the nanopore. The simulation domain Ω is the area between the two cylinders.

In our electrokinetic model, we approximate the dsDNA as an infinitely long cylinder which has a diameter and charge density comparable to that of dsDNA confined in a cylinder with radius r_{pore}. The assumed geometry of the model is shown in Fig. 3.6.

We use cylindrical coordinates (r, φ, z) with respect to the center of the simulation box. The problem domain is given by $\Omega = [r_{\mathrm{DNA}}, r_{\mathrm{pore}}] \times [0, 2\pi] \times \mathbb{R}$.

The salt ions are described as diffusive species with concen-

tration c_i following the diffusion-advection equation [132]

$$\partial_t c_i = -\nabla \cdot \mathbf{j}_i \tag{3.10}$$

$$\mathbf{j}_i = [-D_i \nabla + \mathbf{u} + \mu_i \mathbf{F}_i]\, c_i, \tag{3.11}$$

subject to $j^r = 0$ on $\partial\Omega$. Here $\mathbf{j}_i$ is the ionic current density, D_i the diffusion coefficient of the ions, $\mathbf{u}$ the fluid velocity and $\mathbf{F}_i$ the external force on the species, and μ_i their mobility. The diffusive species have valency z_i, giving them the charges $q_i = \mathrm{e} z_i$ per particle, where e is the elementary charge. The electrostatic potential Ψ is given by Poisson's equation

$$\Delta\Psi = -\frac{\sum_i \mathrm{e} z_i c_i}{\varepsilon_0 \varepsilon_r}, \tag{3.12}$$

subject to $\partial_r \Psi(r_{\mathrm{pore}}) = -\sigma_{\mathrm{pore}}/(\varepsilon_0\varepsilon_r) = 0$ and $\partial_r \Psi(r_{\mathrm{DNA}}) = -\sigma_{\mathrm{DNA}}/(\varepsilon_0\varepsilon_r)$. Here, σ_{Pore} and σ_{DNA} is the surface charge density of the DNA and the pore charge density respectively, ε_r is the relative permittivity of the solvent.

The advective flow field $\mathbf{u}$ is taken into account by considering Stokes' equation:

$$\eta \nabla^2 \mathbf{u} - \nabla p + \mathbf{f} = 0 \tag{3.13}$$

$$\nabla \cdot \mathbf{u} = 0, \tag{3.14}$$

where η is the dynamic viscosity, $\mathbf{u}$ and p are the velocity and pressure fields, and $\mathbf{f}$ is the force density on the fluid caused by the ions. We use no-slip boundary conditions $\mathbf{u} = 0$ on $\partial\Omega$.

Only the stationary case with $\partial_t c = 0$ is considered, and, due to the symmetry of the system, all axial and tangential derivatives vanish. In addition no pressure gradient across the pore is applied, so we also have $\partial_z p = 0$.

This reduces Eq. (3.13) to the radial Stokes equation, the other components of $\mathbf{u}$ are zero:

$$\frac{1}{r}\partial_r(r\partial_r u^z) + f^z = 0. \tag{3.15}$$

Since there is no advection in radial direction ($u^r = 0$) the only force acting on the ions is electrostatics, and we have $F_i^r =$

$-q_i \partial_r \Psi$. With this the radial diffusion-advection equation can be formally integrated for the stationary case ($j^r = 0$), giving

$$c_i(r) = c_i^0 \exp\left(-\frac{z_i \mathrm{e} \Psi(r)}{k_\mathrm{B} T}\right). \tag{3.16}$$

In this equation, c_i^0 is the bulk concentration of the species i, where in the bulk $\Psi = 0$ holds.

With this, the concentrations can be eliminated from Eq. (3.12), yielding a radial POISSON-BOLTZMANN equation for the electrostatic potential Ψ:

$$\frac{1}{r}\partial_r(r\partial_r \Psi) = -\frac{1}{\varepsilon_0 \varepsilon_r} \sum_i c_i^0 z_i \mathrm{e} \exp\left(-\frac{z_i \mathrm{e} \Psi}{k_\mathrm{B} T}\right). \tag{3.17}$$

So far, the force density on the fluid $\mathbf{f} = \mathbf{f}(c_i, \mathbf{j}_i, \mathbf{u})$ and the forces on the diffusive species $\mathbf{F}_i$ are unspecified. This is where we will introduce a friction term as described in the next section.

To determine the force densities on the ions and the fluid, we consider the force balance for a single ion in z-direction. There are three contributions to the forces F_i^z acting on the ions:

1. external electric field:

$$F_i^{z,E} = \mathrm{e} z_i E^z, \tag{3.18}$$

   where E^z is the applied electric field,

2. friction between ions and the DNA:

$$F_i^{z,\mathrm{fric}}(r) = -\alpha \omega(r) v^z, \tag{3.19}$$

   where α is a numerical constant and ω a position-dependent weight function as defined in Eq. (3.8) but taken from the surface of the inner cylinder. The ions velocities can be expressed in terms of the fluxes and concentrations as $v_z = \frac{j_i^z}{c_i}$.

3. Friction between the fluid and the ions $F_i^{z,\mathrm{visc}}$. As we will see, this force is completely determined by the stationary assumption and its form can be directly derived.

Inserting the definitions for the external force $F_i^z = F_i^{z,E} + F_i^{z,\mathrm{fric}}$ in Eq. (3.11), yields

$$j_i^z = \left[\mathbf{u} + \mu_i \left(\mathrm{e} z_i E^z - \alpha\omega \frac{j_i^z}{c_i}\right)\right] c_i, \tag{3.20}$$

where we have used that $\partial_z c_i = 0$. Solving for the current density j_i^z, we arrive at

$$j_i^z(r) = \frac{u^z(r) + \mu_i \mathrm{e} z_i E^z}{\alpha\mu_i\omega(r) + 1} c_i(r). \tag{3.21}$$

Inserting this expression into Eq. (3.19) yields a new expression for the force between ions and DNA:

$$F_i^{z,\mathrm{fric}}(r) = -\alpha\omega(r) \frac{u^z(r) + \mu_i \mathrm{e} z_i E^z}{\alpha\mu_i\omega(r) + 1}. \tag{3.22}$$

Since we are considering a stationary state, the net force on the particles has to vanish, so that

$$F_i^{z,E} + F_i^{z,\mathrm{fric}} + F_i^{z,\mathrm{visc}} = 0. \tag{3.23}$$

Assuming a common mobility $\mu = \mu_i$ for all species allows us to calculate the force density on the fluid $f^z(r) = -\sum_i c_i(r) F_i^{z,visc} = \sum_i c_i (F_i^{z,E} + F_i^{z,fric})$:

$$f^z(r) = \frac{-\alpha\omega(r) \left[\sum_i c_i\right] u^z(r) + \left[\sum_i \mathrm{e} z_i c_i\right] E^z}{\alpha\mu\omega(r) + 1}, \tag{3.24}$$

Using (3.16) to eliminate the concentrations and assuming a 1:1 salt, we arrive at

$$f^z(r) = -2c_0 \frac{\mathrm{e} \sinh\left(\frac{\mathrm{e}\psi(\rho)}{k_\mathrm{B}T}\right) E^z + \alpha\omega(r) \cosh\left(\frac{\mathrm{e}\psi(\rho)}{k_\mathrm{B}T}\right) u_z(r)}{\alpha\mu\omega(r) + 1}. \tag{3.25}$$

For the total current density we get

$$j^z(r) = 2ec_0 \frac{e\mu \cosh\left(\frac{e\psi(\rho)}{k_B T}\right) E^z - \sinh\left(\frac{e\psi(\rho)}{k_B T}\right) u_z(r)}{\alpha\mu\omega(r) + 1}. \quad (3.26)$$

It can be observed that the presence of the friction term in (3.25) changes the character of the equation for u^z. For $\alpha = 0$, if the solution of the POISSON-BOLTZMANN equation was known, Stokes' equation (3.15) could be integrated to yield a closed expression for j^z. With the friction the force density f in Eq. (3.15) depends on u^z, and the equation is similar in mathematical structure to a linearized POISSON-BOLTZMANN equation, for which no solutions in cylinders are known. Therefore, the conductivity of the system is only known implicitly via a differential equation, and no closed expression for it can be given. It is hence not possible to write down an Ohm-type law of the form $j^z = \sigma E^z$ with some conductivity $\sigma = \sigma(c_i, E^z, \dots)$.

The electric current I observed in the simulation is the radially integrated current density

$$I = \int_{r_{\mathrm{DNA}}}^{r_{\mathrm{pore}}} r dr j^z. \quad (3.27)$$

The (ideal) current density of the empty uncharged pore is simply given by

$$j^z_{\mathrm{id}} = 2c_0 e\mu E^z, \quad (3.28)$$

resulting in the total current

$$I_0 = \pi r^2_{\mathrm{pore}} j^z_{\mathrm{id}}, \quad (3.29)$$

and the absolute change in current ΔI is

$$\Delta I = I - I_0,$$

from which the relative change can be calculated.

We solve the coupled ODE system of Eq. (3.15) and Eq. (3.17) with the force density term (3.24) for the Stokes' equation numerically. We then evaluate Eq. (3.27) to obtain the ionic currents. The numerical solutions are obtained by finite element

method (FEM) calculations. To this end, the equation system and geometry are implemented in a model for the commercial FEM package Comsol MULTIPHYSICS 5.3a by Comsol AB. Due to the low-dimensional nature and small size of the problem domain, the whole system can be regularly resolved with a sufficiently fine mesh. Also, numerical artifacts such as spurious flows, which electrokinetic systems are prone to in general [49], do not occur here because the diffusion-advection/Poisson-Boltzmann equation is only solved in directions orthogonal to the flow velocity.

The geometry of the continuum model described in this article differs from the coarse-grained molecular dynamics model described in Ref. [52]: Here, we use a cylinder for the DNA, while in the particle model, the double-helix structure is explicitly represented. We still use the same functional form as in Eq. (3.19) for the friction and the same cutoff radius r_c.

All other parameters are provided by the system under study. As in the experiment [126], we assume an aqueous potassium chloride solution at a temperature of $T = 300\,\mathrm{K}$ and the dynamic viscosity of $\eta = 0.001\,\mathrm{Pa\,s}$ for water. For the diffusion coefficients, we use the infinite dilution value of $D = 2.0 \times 10^{-9}\,\mathrm{m^2\,s^{-1}}$ for both ionic species [133]. We assume that the Einstein relation is valid, and set $\mu = \frac{D}{k_\mathrm{B}T} = 4.8286 \times 10^{11}\,\mathrm{s\,kg^{-1}}$. We use $\varepsilon_r = 80$ for water, resulting in a Bjerrum length of $\lambda_B = 0.7\,\mathrm{nm}$. We employ a pore diameter of size $d_\mathrm{pore} = 10\,\mathrm{nm}$ except for the calculations where the pore radius is varied. The numerical constant α introduced in Eq. (3.19) is chosen such that our model matches the experiment well at the crossover salt concentration. After this calibration, we use a fixed value of $\alpha = 1.5\,\mathrm{kg\,s^{-1}}$ for all parameter variations throughout the paper. It is crucial for the transferability of the model that a single parameter yields good results for all salt concentrations. The cutoff r_c for the position-dependent friction $\omega(r)$ of Eq. (3.19) is set to 2.5 nm in accordance with Ref. [52].

Current density for positively and negatively charged species

(denoted by suffix $_+$ and $_-$):

$$j_+ = \frac{u^z + \mu e E^z}{\alpha\mu\omega + 1} c_+ e, \tag{3.30}$$

$$j_- = -\frac{u^z - \mu e E^z}{\alpha\mu\omega + 1} c_+ e, \tag{3.31}$$

where u^z is the fluid velocity, μ the ion's electrophoretic mobility, α is a friction constant, ω the distance-dependent frictional weight function, e the elementary charge and c_+/c_- are the number densities of the charged species. The total current density reads:

$$j_{\text{total}} = j_+ + j_- = \frac{e u_z \left(c_+ - c_-\right) + \mu e^2 E^z \left(c_+ + c_-\right)}{\alpha\mu\omega + 1} \tag{3.32}$$

Extension to an origami model

In order to resample the geometry of a DNA origami consisting of a block of multiple interconnected DNA helices we used the DNA representation of the mean field model as described in the previous section as a building block. This building block is then replicated as shown in the sketch in Fig. 3.7.

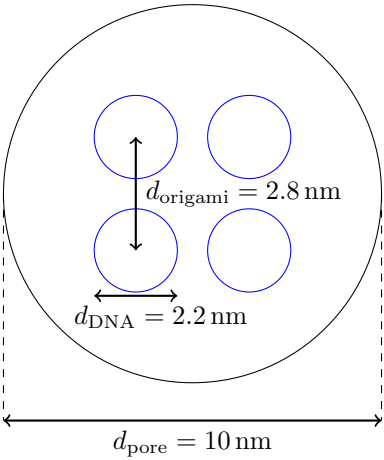

Figure 3.7: Sketch of the DNA origami model's geometry.

3.4 Mean field model of a finite pore-DNA system

The model description in this section is part of a draft for a publication that has not been submitted at the time of writing.

The model under study incorporates two electrolyte reservoirs with a monovalent electrolyte solution of varying concentration that are connected by a nanopore. The DNA is modeled as a cylindrical object with rounded ends fixed at the center of the pore. The DNA ends are modeled as hemispherical caps of the same diameter as the DNA. We mainly follow the modeling approach as described of Weik *et al.* [53] However, while they neglect any finite size effects of the pore and the DNA molecule, the model in this work explicitly takes these effects into account. The sketch in Fig. 3.8 shows the whole simulation domain with the two electrolyte reservoirs, the connecting nanopore and the DNA in the center of the pore. The diameter of the pore is 10 nm while the investigated pore length is 40 nm. The length of the DNA is varied in the range from 0.4 to 1.6 pore lengths (*i. e.* 16 nm to 64 nm) in order to also investigate the conductivity for systems where the DNA is significantly shorter or larger than the nanopore. The overall system length has been set to 10 times the pore length.

The mean field model employed in this work is based on solving the electrokinetic equations (Poisson for electrostatics, Nernst-Planck for ion transport and Stokes for hydrodynamics of the solvent) for a charged cylinder representing the dsDNA in an uncharged cylinder representing the nanopore following the approach in Ref. [53]. The Nernst-Planck equation is modified to incorporate the friction between ions and the dsDNA molecule that has previously been found to be crucial for coarsened dsDNA models in order to reproduce experimental and all-atom simulation data on current modulation in nanopores [47, 52].

The diffusion-advection equation for the fluxes of the ionic

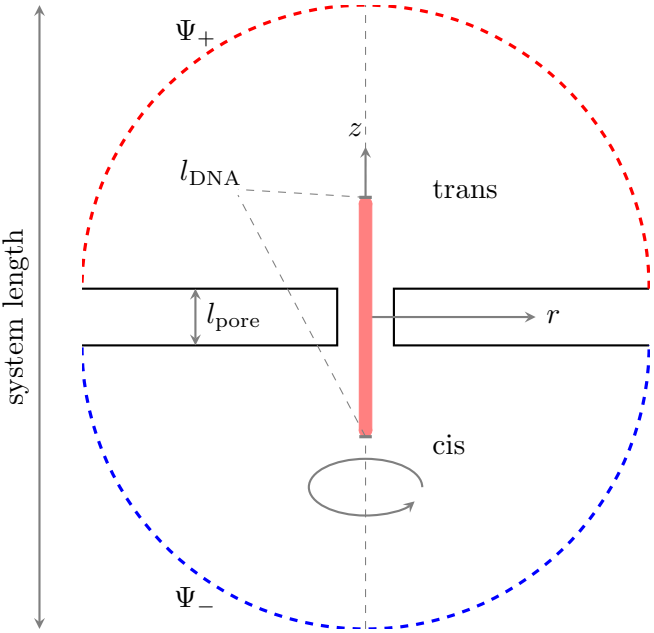

Figure 3.8: A sketch of the mean field model of a nanopore with finite length. The system is axisymmetric and can therefore be treated in two dimensions. The hemispheric areas at the top and the bottom correspond to the cis and trans electrolyte reservoirs.

species $\mathbf{j}_\pm$ in the system reads:

$$\mathbf{j}_\pm = \left[-D\nabla + \mathbf{u} + \mu_\pm \mathbf{F}_\pm\right] c_\pm, \tag{3.33}$$

where $D_\pm$ is the diffusion constant, $\mathbf{u}$ is the fluid velocity, $\mu_\pm = \mu = \frac{D}{k_\mathrm{B}T} = 4.8286 \times 10^{11}\,\mathrm{s\,kg^{-1}}$ is the ion mobility, $\mathbf{F}_\pm$ contains any external forces, and $c_\pm$ the ion density. The external forces are comprised of the electrostatic forces and the frictional forces:

$$\mathbf{F}_\pm = ez_\pm \mathbf{E} - \alpha\omega \left(0, 0, \frac{j_\pm^z}{c_\pm}\right)^\mathsf{T}. \tag{3.34}$$

Due to the velocity dependent frictional force, this results in an

algebraic equation for the fluxes along the pore (z component):

$$j_{\pm}^{z}(r,z) = \left[-D\frac{\partial}{\partial_z} + u^z(r,z) + \mu \left(ez_{\pm}E^z(r,z) - \alpha\omega(r,z)\frac{j_{\pm}^{z}(r,z)}{c_{\pm}(r,z)} \right) \right] c_{\pm}(r,z), \quad (3.35)$$

where e is the elementary charge, $z_{\pm}$ the valency of the ions, E^z the electric field strength along the symmetry axis, $\alpha = 15 \times 10^{-12}\,\mathrm{kg\,s^{-1}}$ a numerical constant (controlling the amount of frictional force) and ω is a position dependent weight function for the frictional force (adopted from Ref. Weik *et al.* [53]):

$$\omega(r,z) = \begin{cases} \left(1 - \frac{r}{r_{\mathrm{cut}}}\right)^2 & \text{if } r < r_{\mathrm{cut}} \text{ and } |z| < \frac{l_{\mathrm{DNA}}}{2}, \\ 0 & \text{else,} \end{cases} \quad (3.36)$$

where $r_{\mathrm{cut}} = 1.4\,\mathrm{nm}$ is the cutoff distance for the friction. We assume temperature of 300 K throughout all simulations.

The advective motion of ions is taken into account by means of Stokes' equations with incompressibility condition (*cf.* Eq. (3.13)). A no-slip boundary condition $\mathbf{u} = 0$ is applied on both the pore and DNA surface. Hydrodynamic momentum exchange over the reservoir boundaries (dashed lines in Fig. 3.8) is prevented by applying a vanishing normal stress condition for the fluid flow.

Electrostatic interactions between ions are considered by solving the Poisson equation (*cf.* Eq. (3.12)). On the DNA boundary, we set the surface charge density $\sigma = -0.136\,\mathrm{C/m^2}$. For the pore surface a zero-charge condition $\mathbf{n} \cdot \nabla\Psi = 0$ is applied, where $\mathbf{n}$ denotes the unit vector normal to the boundary. For the lower and upper boundaries (drawn with blue and red dashed lines in Fig. 3.8) we set the electrostatic potentials $\Psi_{-} = 0$ and $\Psi_{+} = l_{\mathrm{pore}}E_{\mathrm{ext}}^{z}$ with l_{pore} being the length of the pore and $E_{\mathrm{ext}}^{z} = 1 \times 10^6\,\mathrm{V\,m^{-1}}$ being the approximate value for the electric field in comparable experimental setups [31]. By choosing the electrostatic potential difference depending on the pore

length and thereby keeping the electric field in the pore approximately constant we are able to directly compare results from different pores. The friction between ions and dsDNA results in a coupling between electrostatic and advective forces on the ions. The model's inherent axisymmetry reduces the problem domain to two dimensions. We solved the electrokinetic equations with the finite-element method using the commercial software package COMSOL Multiphysics® version 5.6.

Effective Pore Length

In experimental studies of Wang *et al.* [31] a similar setup to the model presented in this manuscript has been utilized to investigate the current modulation of complex DNA structures. One of the more significant differences, however, is the pore geometry. The glass capillaries used in the experimental study have a diameter of about 10 nm at the tip but have a conical geometry with an opening angle of about 6°. It is known from experimental [54] as well as simulation studies [53] that a wider nanopore causes a larger magnitude of electroosmotic flow which leads to a larger contribution of the advective current to the overall ionic current. However, all-atom simulations in an infinite cylindrical pore setup [47] revealed that this contribution is negligible for infinite DNA nanopore systems. Nevertheless, even if this geometric effect might not be significant for the conductivity of the system, the absolute length of the nanopore might influence the importance of the finite size effects. To get an estimate for up to which length the conicity of the experimental pore affects the conductivity, we calculated the length-dependent pore resistance. For an infinitesimal pore segment of length $\mathrm{d}z$ the resistance of a conical pore with the cross-section area $A(z)$ can be described as

$$\mathrm{d}R = \rho \frac{\mathrm{d}z}{A(z)}, \tag{3.37}$$

where ρ is the bulk electrolyte resistance and $A(z) = \pi r(z)^2 = \pi(r_1 + z\tan\alpha)^2$ is the cross-section area of the pore at the position z measured from the tip of the pore. Here, α denotes the

opening angle of the conical pore geometry. Integrating Eq. 3.37 yields:

$$R(z) = \rho \int_0^z \mathrm{d}\tilde{z} \frac{1}{A(\tilde{z})} = \frac{\rho}{\pi} \frac{z}{(r_1(z + \frac{r_1}{\tan\alpha})) \tan\alpha} \tag{3.38}$$

In Fig. 3.9, Eq. 3.38 is shown for a pore length up to 1 µm. The value of the bulk resistance ρ is arbitrarily set to unity. In the

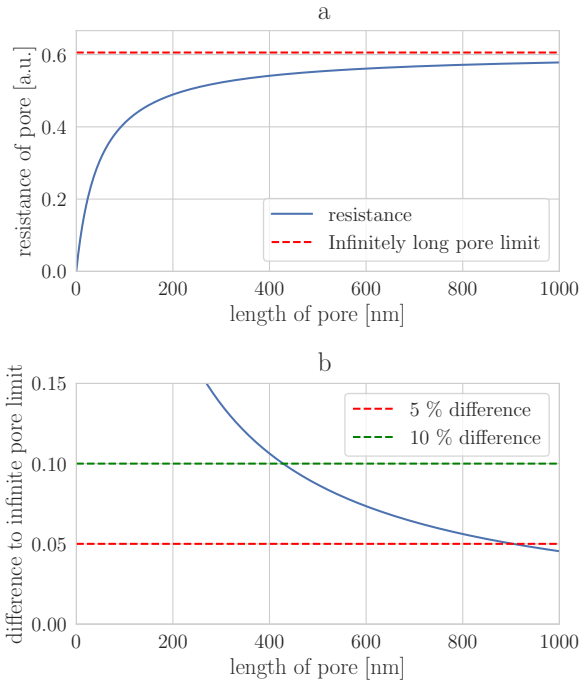

Figure 3.9: Length-dependent pore resistance for a conical pore and the respective resistance in the infinite pore limit (a). The difference between the resistance of the conical pore with a given length and the infinite pore limit (b). The crossing of the 5 % line and the resistance curve is at about 900 nm.

limit of an infinitely long conical pore Eq. (3.38) converges to

a resistance of $R_\infty = \frac{\rho}{\pi \tan(\alpha) r_1}$. However, as shown in Fig. 3.9, the largest contribution to the resistance (95 % at about 900 nm) suggests an effective length of the pore on the order of several hundred nanometers. Although this model only takes into account the resistance based on the geometry of the pore, the result is in line with simulation studies in Ref. [30] in which the decay of the electric field in the pore was used to estimate the sensing length.

The DNA structures studied by Wang *et al.* in Ref. [31] are between approximately 150 nm and 600 nm and are therefore shorter than the estimated effective pore length. This clearly sets those DNA nanopore systems apart from many other experimentally investigated setups in which the DNA is orders of magnitude longer than the pore.

Electric Dipole Field Model

This model assumes that the z-component of the total dipole moment DNA nanopore system is created by a single pair of charges at the two ends of the DNA on the symmetry axis. This assumption is based on the observation that the charge density is asymmetric along the DNA as shown in Fig. 3.10. Thus, the electrostatic potential of these two charges ($+q$ at $z = -0.5\, l_{\mathrm{DNA}}$ and $-q$ at $z = 0.5\, l_{\mathrm{DNA}}$) reads:

$$\Phi(r,z) = \frac{|q|}{4\pi\epsilon_0\epsilon_\mathrm{r}} \left[\left(r^2 + \left(z + \frac{l_{\mathrm{DNA}}}{2} \right)^2 \right)^{-\frac{1}{2}} - \left(r^2 + \left(z - \frac{l_{\mathrm{DNA}}}{2} \right)^2 \right)^{-\frac{1}{2}} \right]. \tag{3.39}$$

From the electrostatic potential, the z-component of the electric field at $z = 0$ can be calculated by taking the negative gra-

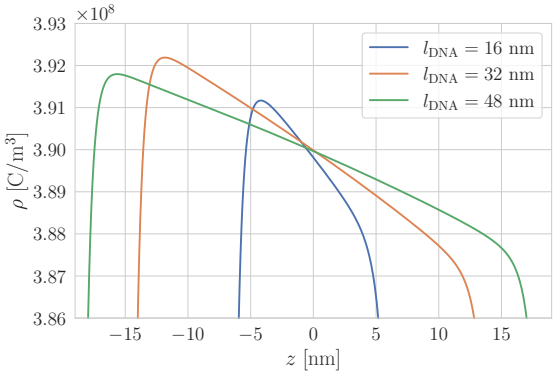

Figure 3.10: The charge density along the z-axis at $r = r_{\mathrm{DNA}}$ for three different DNA lengths. The ion cloud at the vicinity of the DNA is asymmetric due to the externally applied electric field.

dient of the potential:

$$E_z^{\mathrm{dipole}}(r, z=0) = \left(-\nabla\Phi(r,z)\right)_{z,z=0} = \frac{2\,|q|\,l_{\mathrm{DNA}}}{\pi\epsilon_0\epsilon_{\mathrm{r}}\left(l_{\mathrm{DNA}}^2 + 4r^2\right)^{\frac{3}{2}}}. \tag{3.40}$$

We now insert the assumption that the system's total dipole moment is only caused by the two charges, *i. e.* $|q| = \frac{|P_z|}{l_{\mathrm{DNA}}}$

$$E_z^{\mathrm{dipole}}(r, z=0) = \frac{2\,|P_z|}{\pi\epsilon_0\epsilon_{\mathrm{r}}\left(l_{\mathrm{DNA}}^2 + 4r^2\right)^{\frac{3}{2}}}. \tag{3.41}$$

FEM Mesh

The rotational symmetry of the investigated three-dimensional system setup allows for its treatment using a quasi-two-dimensional axisymmetric simulation domain. The FEM mesh for this domain was adapted (*cf.* Fig. 3.11) in order to properly resolve the

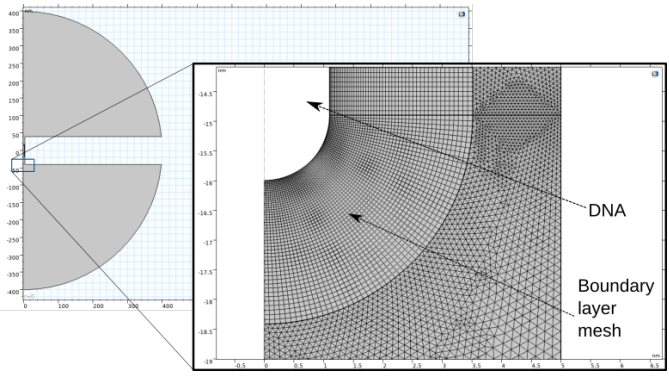

Figure 3.11: Example of the customized mesh used for the FEM simulations. The area around the electrically charged DNA surface is resolved with quadrilateral elements to properly capture the behavior in the Debye layer. The rest of the simulation domain consists of triangular mesh elements.

Debye layer near the negatively charged DNA. Using quadrilateral elements close to the DNA surface, the geometry of the mesh more closely follows the expected symmetry of the solution for the Poisson equation for electrostatics which defines the smallest length scale in the investigated DNA nanopore system.

Chapter 4

Results

This chapter contains the results of investigations for various systems that incorporate the three different DNA models on the all-atom (as described in Sec. 3.1), coarse-grained (as described in Sec. 3.2) and mean-field (as described in Sec. 3.3) level of detail. First, the validation and basic investigations for the coarse-grained model are shown in Sec. 4.1 since this model was the starting point for all the investigations. In Sec. 4.2, the mean-field model is discussed in great detail. Afterwards, in Sec. 4.3 a comparison of all three models in an origami configuration is discussed and compared to experiments. Finally, in Sec. 4.4 a finite pore system is investigated by means of a mean-field description.

4.1 Coarse-grained model

The coarse-grained model as described in Section 3.2 had to be validated against reference data since the implementation of such a model in combination with an updated version of the simulation package ESPResSo was non-trivial in several ways. First, there are many interactions with respective parameters that have to be set between the beads of the DNA model (*cf.* details in 3.2) which had not been documented precisely for the original implementation that has been described in Refs. [52, 76]. Furthermore, between publication of the aforementioned and the reimplemen-

tation there has been a change of the interface scripting language in ESPResSo and bug fixes for parts of the frictional interactions for which the impact on the simulation results was not clear.

In order to validate the interactions between the ions and the DNA model, we checked for the radial density profiles of the ions around the DNA in an infinite pore system with a pore diameter of 10 nm and compared the data to reference data of all-atom simulations [47]. This comparison is shown in Fig. 4.1 for a single salt concentration. Clearly the counter-ion structure resembles the all-atom data very well. However, due to the coarser beads of the DNA model the layering structure is not reproduced perfectly. The radial structure of the repressed co-ions around the DNA matches very well with the reference data.

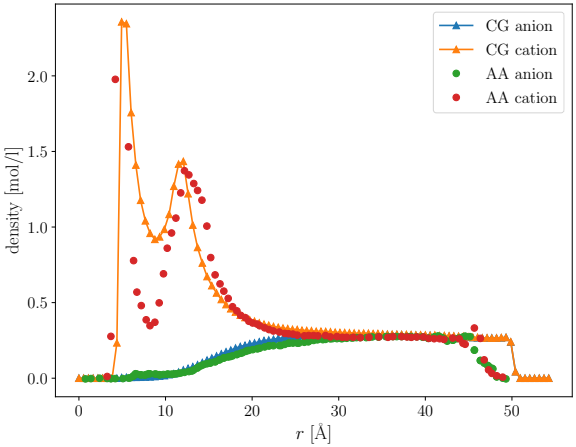

Figure 4.1: Comparison of the ion densities retrieved from all-atom and coarse-grained simulations of a single dsDNA molecule.

In order to compare not only static and structural data with the all-atom reference the salt dependent current modulation in an infinite pore system has been looked at. The current modulation is defined by $I_{\text{modulation}} = (I_{\text{DNA}} - I_{\text{empty}})/I_{\text{empty}}$, where

I_{DNA} is the current through the pore if a DNA molecule is present and I_{empty} is the current through an empty pore. The comparison in Fig. 4.2 shows a very good agreement between the data of the reimplemented coarse-grained DNA model and the all-atom reference data of Ref. Kesselheim *et al.* [47]. This is a very important reference benchmark for the ion-DNA interaction including the distance dependent frictional interaction as described in Sec. 3.2. The fact that the re-implementation in combination with the updated version of ESPResSo (git hash: `846cc74bef84d28ba46563d0e9e845a9dc5afc80`) is able to reproduce the current modulation renders this model a good starting point for further investigations, *e. g.* as a building block for DNA origami molecules as presented in Sec. 3.2.

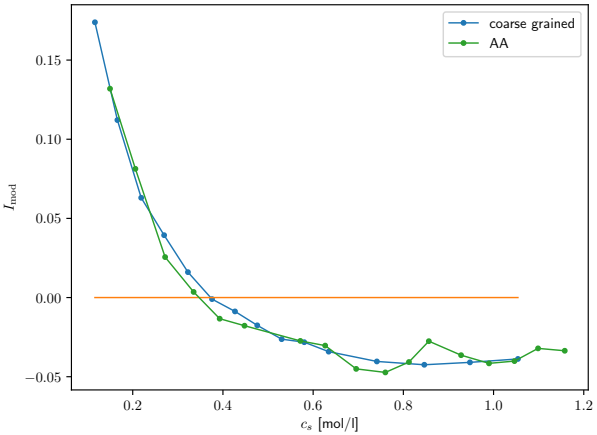

Figure 4.2: Comparison of the ionic current modulation retrieved from all-atom and coarse-grained simulations of a single dsDNA molecule.

In order to study a finite DNA nanopore system with the coarse-grained model the linear response regime for the electrophoretic mobility of the DNA with respect to the applied

electric field had to be estimated. This is the regime in which the electrophoretic mobility of the DNA chain does not depend on the externally applied electric field, *i. e.* the regime in which the chain is not significantly deformed by the electric field. To this end, the coarse-grained DNA chain with 20 base pairs has been simulated in a cubic box with a side length of 20 nm. In order to keep the system electroneutral the respective amount of counter-ions has been added. Two different approaches to measure the electrophoretic mobility have been examined: first, using a GREEN-KUBO relation exploring cross correlations between the center of mass of the DNA and all charged particles in the system, and second, applying an electric field and measuring the velocity of the DNA's center of mass. The GREEN-KUBO relation as derived in Ref. [134] and applied in Refs. [135, 72] reads:

$$\mu = \frac{1}{3k_{\mathrm{B}}T} \sum_i q_i \int_0^\infty \langle \mathbf{v}_i(0)\mathbf{v}_{\mathrm{COM}}(\tau)\rangle \, d\tau, \tag{4.1}$$

with q_i being the charge of particle i in the system, $\mathbf{v}_i$ the particle velocity and $\mathbf{v}_{\mathrm{COM}}$ the velocity of the DNA's center of mass.

Fig. 4.3 shows the result for both approaches. In the Figure at the top the field strength dependent center of mass velocity is shown (all in reduced units, absolute numbers are not relevant) and in the Figure below the respective mobilities. For electric field strengths below ≈ 0.1 a constant mobility is measured whereas for higher external fields the mobility increases. This is in line with literature values as presented in Ref. [136]. Deviations between the measured electrophoretic mobilities via the GREEN-KUBO approach without applied field and the approach for varying external field can be attributed to poor statistics of the cross-correlation that gets numerically integrated (*cf.* Eq. (4.1)). A systematic error estimation for the GREEN-KUBO estimation for the mobility has not been performed in the course of this study.

Due to the fact that the electrostatic interactions between charged particles are long-ranged and cannot be cut off at some finite distance there exist algorithms to treat charged particles in periodic boundary conditions, namely the Particle-Particle

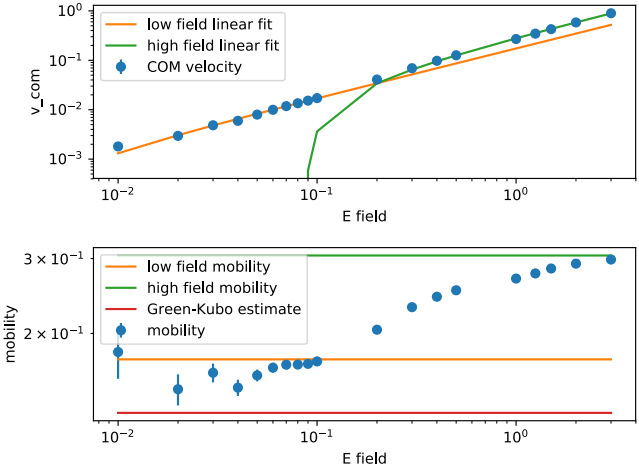

Figure 4.3: Comparison of simulation results for the electrophoretic mobility for different magnitudes of the external field. The data shows that an external field up to about 0.1 in reduced units leads to mobilities that are comparable to linear-response theory. For higher field strengths a non-linear behavior can be observed.

Particle-Mesh algorithm [112]. This algorithm is based on the so-called *Fast Fourier Transform*(FFT) algorithm and therefore scales as $\mathcal{O}(N \log N)$, with N being the number of charged particles. However, this algorithm is still the most time-consuming part of a molecular dynamics simulation of charged particles. Therefore, in order to keep the number of charged particles minimal a system with only counter-ions has been investigated. To this end, the simulation system contained the coarse-grained DNA with 20 base pairs, the 40 counter-ions and a membrane with a nanometer-sized cylindrical or conical pore with a length of 60 base pairs. The investigation of differences in the ionic current due to the shape of the nanopore, *i. e.* the comparison between conical and cylindrical geometries, is only possible if

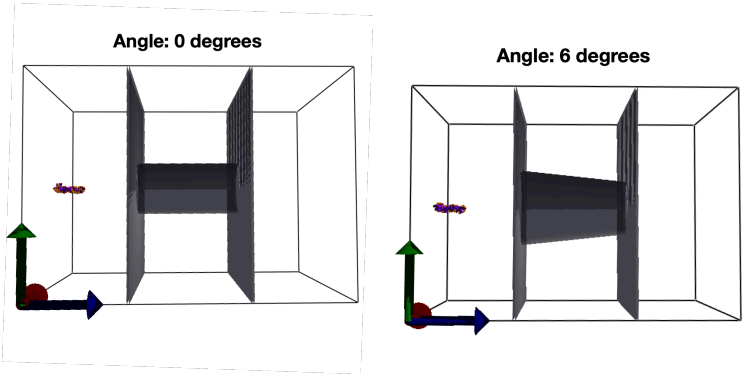

Figure 4.4: Snapshots of a visualization of a system of a finite cylindrical (left) and conical (right) pore for the coarse-grained model of a 20 base pair DNA.

the system contains a finite pore and the two reservoirs. The opening angle of 6° for the conical pore used in the simulation is motivated by the geometry of experimentally investigated glass nanocapillaries in the context of DNA nanopore translocation [31]. The diameter of the conical pore's smaller orifice matches the one of the cylindrical nanopore. Fig. 4.5 shows the ionic current through the pore as a function of the center of mass of the DNA. The conical pore system shows a slightly higher conductivity which may be attributed to a reduced interaction between the counter-ions and the pore wall. Simulations of systems with excess salt did not yield results with sufficient statistics due to the fact that the electric field is nearly zero outside the pore. Therefore, the DNA has to reach the pore mostly due to diffusion which renders these simulations very expensive in terms of computational effort. In order to find a computationally more efficient DNA model a mean-field approach has been investigated in the next section.

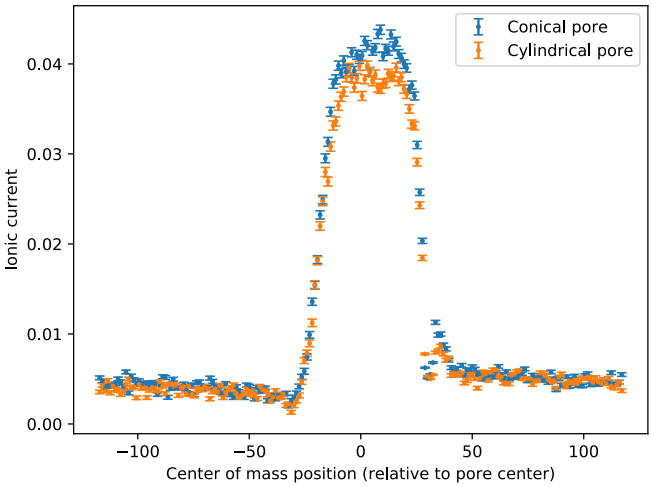

Figure 4.5: The ionic current as a function of the center of mass for a coarse-grained model of a freely translocating DNA with 20 base pairs. No excess salt has been added to the system.

4.2 A mean field investigation of a DNA nanopore system

The results presented in the this section are part of the following publication (F. Weik and K. Szuttor contributed equally):

> Florian Weik, Kai Szuttor, Jonas Landsgesell, and Christian Holm. Modeling the current modulation of dsDNA in nanopores – from mean-field to atomistic and back. *European Physical Journal Special Topics*, 227(14):1639–1655, 2019. doi: 10.1140/epjst/e2019-800189-3

The geometry of the continuum model described in this article differs from the coarse-grained molecular dynamics model

described in Ref. [52]: Here, we use a cylinder for the DNA, while in the particle model, the double-helix structure is explicitly represented. We still use the same functional form as in Eq. (3.19) for the friction and the same cutoff radius ρ_c.

All other parameters are provided by the system under study. As in the experiment [126], we assume an aqueous potassium chloride solution at a temperature of $T = 300\,\mathrm{K}$ and the dynamic viscosity of $\eta = 0.001\,\mathrm{Pa\,s}$ for water. For the diffusion coefficients, we use the infinite dilution value of $D = 2.0 \times 10^{-9}\,\mathrm{m^2\,s^{-1}}$ for both ionic species [133]. The Einstein relation is assumed to be valid, thus the mobility is set to $\mu = \frac{D}{k_\mathrm{B}T} = 4.8286 \times 10^{11}\,\mathrm{s\,kg^{-1}}$. The relative permittivity of the medium is set to $\varepsilon_r = 80$ for water, resulting in a Bjerrum length of $\lambda_B = 0.7\,\mathrm{nm}$. The investigated pore diameter is $d_\mathrm{pore} = 10\,\mathrm{nm}$. Deviating pore diameters are mentioned explicitly in the section that contains the study about the influence of the pore size. The numerical constant α introduced in Eq. (3.19) is chosen such that our model matches the experiment well at the crossover salt concentration. After this calibration, we used a fixed value of $\alpha = 1.5\,\mathrm{kg\,s^{-1}}$ for all parameter variations throughout the paper. It is crucial for the transferability of the model that a single parameter yields good results for all salt concentrations. The cutoff ρ_c for the position-dependent friction $\omega(\rho)$ of Eq. (3.19) is set to 2.5 nm in accordance with Ref. [52].

As defined in Ref. [47], the current modulation is $\frac{\Delta I}{I_0} \equiv (I_{\text{with DNA}} - I_0)/I_0$, where I_0 is the current of the empty pore, given by Eq. (3.29). When the dsDNA is absent, the system just consists of a bulk volume of an ideal electrolyte solution, and the current is easily calculated analytically.

To verify that the conductivity modulation from the experiment and the molecular dynamics simulations are reproduced, we vary the bulk concentration c_0 of the species from zero to $1\,\mathrm{mol\,l^{-1}}$, similar to the range covered in previous simulations and experiments. The current change caused by the presence of DNA in the pore was calculated according to Eq. (3.27) for each salt concentration. The resulting current modulations are shown in Fig. 4.13. The current modulation of the coarse-grained model is reproduced very closely. However, removing the friction term

results in significant deviations. This strongly suggests that the friction coupling term introduced in the previous section can be used to model the electrokinetic influence of the DNA.

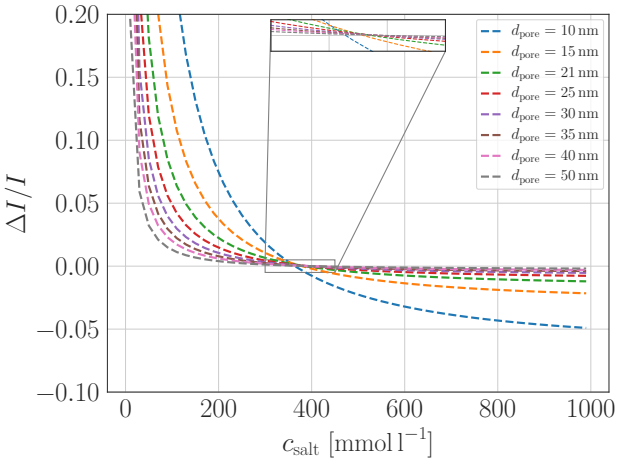

Figure 4.6: The current modulation for a single DNA in pores of varying diameter $d_{\mathrm{pore}} \in [10\,\mathrm{nm}, 50\,\mathrm{nm}]$. The inset enlarges the region of the crossover concentration c^*_{salt} which is described in the text.

In the following the dependency of the current modulation on the properties of the pore is investigated. To this end, we repeat the calculation of the current modulation for pores with different diameters. The results are shown in Fig. 4.6. The trends we observe for the pore size dependence of the current modulation are similar to experimental results reported earlier by van Dorp *et al.* [54]: In the investigated range of salt concentrations c_{salt} between 20 and 50 mmol l^{-1}, the change in relative conductivity is larger for small pores than for larger pores.

Fig. 4.7 depicts the cross-over salt concentration c^*_{salt} as a function of the pore size [1]. The obtained data shows that c^*_{salt}

[1]The crossover concentrations for different salt concentrations are ob-

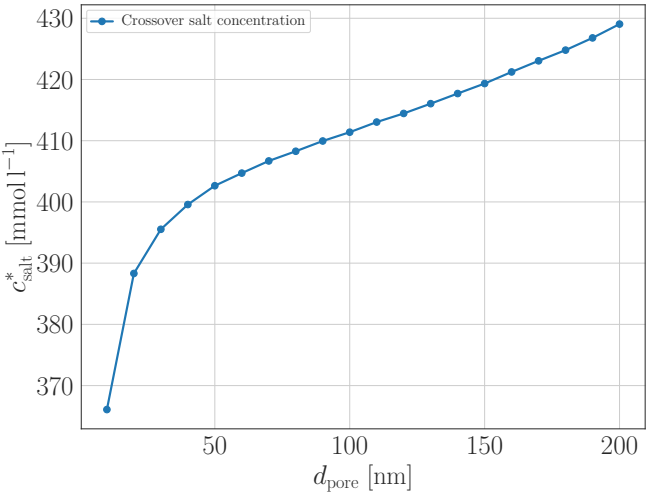

Figure 4.7: The crossover salt concentration dependence as function of the pore diameter.

has a weak dependence on the pore size. This may be of interest to estimate the uncertainties for experimental results, now being able to predict the influence of pore size variations on the current modulation.

In general, the crossover concentration is influenced by the relative importance of the friction and by the solvent velocity u_z. The relative importance of the friction can be defined as the ratio of the volume in which friction influences the ions to the total volume. Clearly, this ratio decreases with increasing pore radius ($\rho_c/\rho_{\text{pore}} \to 0$ for large ρ_{pore}). As shown in Fig. 4.8, u_z is increased for larger pore sizes, which results in a larger advective velocity of the ions and in an increased frictional loss. The resulting influence of the pore size on the current modulation is therefore hard to predict. However, our results (*cf.* Fig. 4.6) show that a larger pore leads to an increased conductivity, yet

tained from the current modulation curves in Fig. 4.9 via fitting a line to the data points $\Delta I(c_{\text{salt}})$ around the zero crossing.

this dependency is weak taking into account pore size uncertainties in the experiment [126].

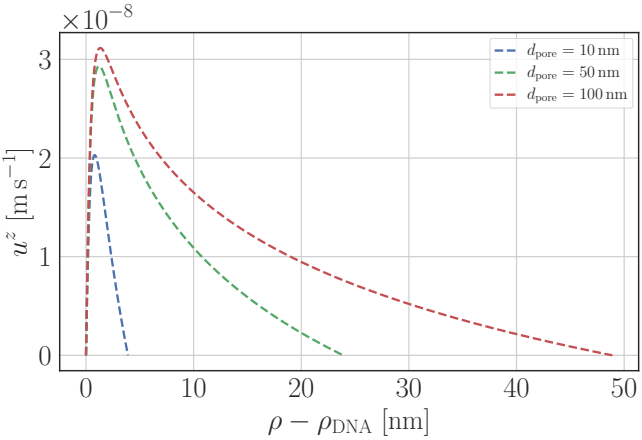

Figure 4.8: The radial flow velocity profile $u(\rho)$ for a varying pore diameter at a salt concentration of $c_{\text{salt}} = 380\,\text{mmol}\,\text{l}^{-1}$.

Consistent with the previous explanation of a reduced influence of the DNA friction with increasing pore size, it is observed that the change in cross-over salt concentrations is stronger for small pore diameters as compared to larger pore diameters (*cf.* Fig. 4.7).

In the experiment, a multitude of different pore types are used, which are produced with different techniques. Moreover, some pores carry a surface charge. This was neglected in our previous molecular dynamics investigations. Specifically, glass have a negative surface charge [137]. Hence, we investigated the influence of pore surface charge σ_{pore} on the ionic current. In our continuum model, the surface charge can be easily added by changing the boundary condition for the electrostatic potential in Eq.(3.12) from $\partial_\rho \psi(\rho_{\text{pore}}) = 0$ to $\partial_\rho \psi(\rho_{\text{pore}}) = -\sigma_{\text{pore}}/(\varepsilon_0 \varepsilon_r)$. In our calculation, we increased σ_{pore} in steps from zero (previous calculations) to a value of $-0.15\,\text{C}\,\text{m}^{-2}$, which are typical surface charge densities for glass nanocapillaries [137]. In this

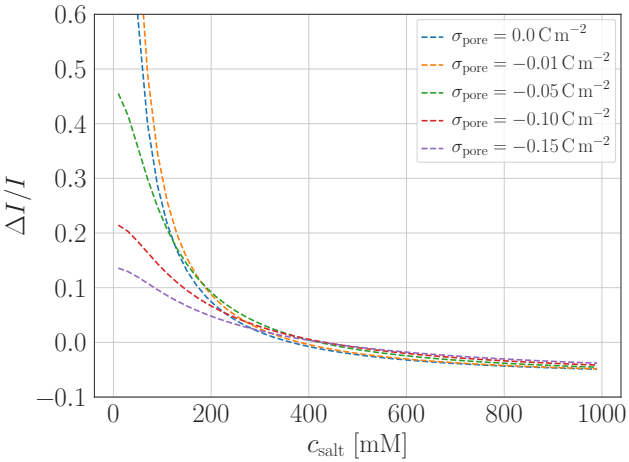

Figure 4.9: The current modulation for a single DNA in pores of varying charge densities on the pore.

case the current without DNA can no longer be determined by Eq. (3.29), but is calculated numerically by removing the inner cylinder from the setup. Fig. 4.9 shows the conductivity behavior with various surface charges on the outer cylinder. We can see that there is little influence of such a charge except for very low salt concentrations. In the salt-free case, the current through the pore is zero. Therefore, the current modulation curve diverges for an uncharged pore at zero salt. For low salt concentrations and low pore charges, the charge modulation curve seems to diverge, however it has a finite value. This can be explained by the fact that the empty pore now is conductive even with no added salt because of the counter ions compensating the surface charge. Therefore, the ratio plotted remains finite at concentration zero.

Further increasing the surface charge density of the pore reveals a significant change of the current modulation at low salt concentrations (*cf.* Fig. 4.9). The additional counterions of the charged pore reduce the increase of the current that the counte-

rions of the DNA provide compared to the empty but charged pore. Therefore, the current modulation is reduced compared to the uncharged pore.

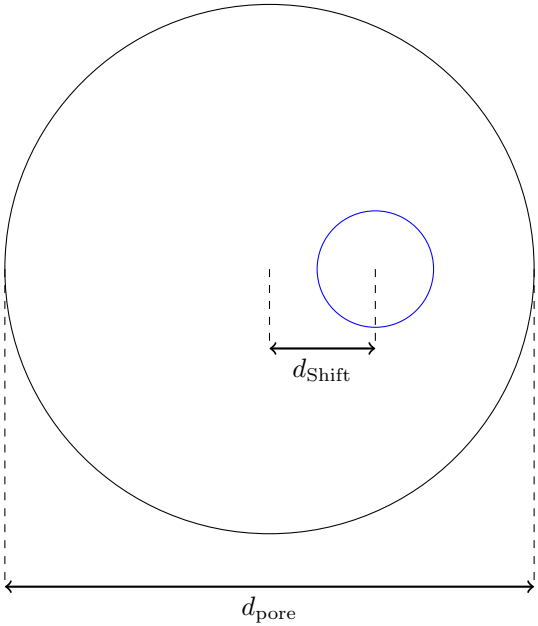

Figure 4.10: Sketch of the shifted DNA.

So far, the DNA was assumed to be in the center of the pore. This, of course, will reflect the experimental situation at most on average. Therefore, we also calculated the influence of shifting the DNA from the center of the pore via appropriately extending the one-dimensional model: The system no longer has radial symmetry, thus the radial model has to be extended by explicitly taking into account the ϕ dependence of the fields. To this end, we varied d_{shift} defined as in Fig. 4.10 from zero to 3.8 nm in a pore with $d_{\text{pore}} = 10\,\text{nm}$. Again, we looked at the current modulation, which is shown in Fig. 4.11. We observe a moderate reduction of the current with increasing d_{shift} due to the

reduced electroosmotic flow between DNA and pore boundary. In Fig. 4.12, the change of the cross-over salt concentration c^*_{salt} as a function of the shift is shown. For small values of d_{shift}, the change is negligible. However, when the distance between the DNA and the pore boundary is comparable to the Debye length, the reduction in the current becomes more significant.

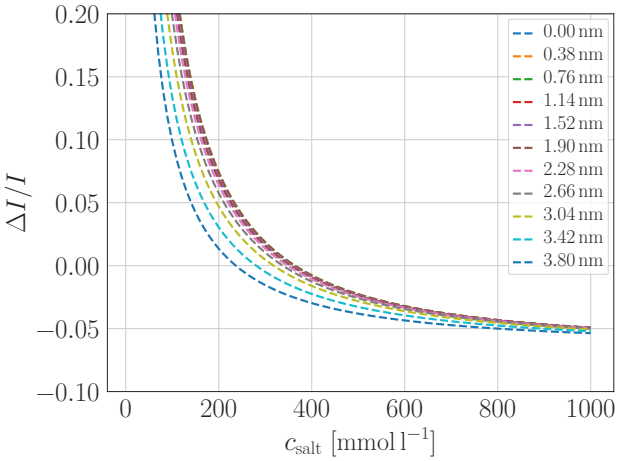

Figure 4.11: The current modulation for a single DNA in a pore with pore radius of 5 nm at various shifts of the DNA from the center of the pore. The shift d_{shift} is denoted in the legend. The DNA shift ranges from 0 nm to 3.8 nm.

In the following, we briefly recapitulate the physical mechanisms that influence the relative conductivity. For low salt concentrations, the current modulation is positive because the DNA adds many counterions contributing to the ion current through the pore. At higher salt concentrations, the current modulation is negative because first, the DNA blocks some volume which is not available for ion conductivity and second, the DNA friction reduces the flow of ions. At the cross-over salt concentration, the DNA-induced current blocking and the enhancement of the

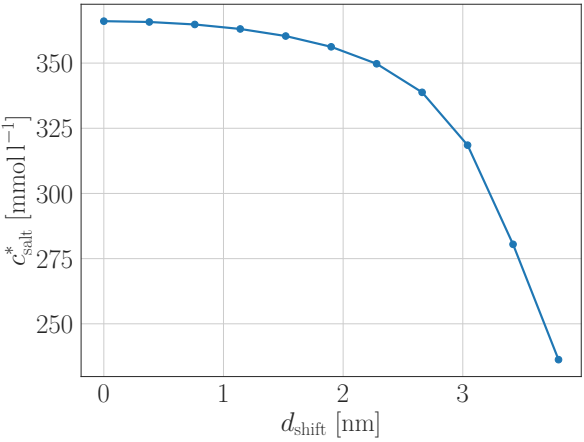

Figure 4.12: The crossover salt concentration for various shifts of the DNA from the center of the pore. The crossover concentrations are derived from the data shown in figure 4.11.

current cancel each other. Therefore, the current modulation vanishes at the crossover concentration c^*_{salt}.

Conclusion and Further Work

We have demonstrated how simulations performed on different scales are able to elucidate the influence of a dsDNA on ionic currents within a nanopore. The all-atom results of Kesselheim *et al.* have shown that a distance-dependent friction is the key ingredient for understanding the experimentally observed behavior. In a previous study, we were able to use this information to construct a viable coarse-grained molecular dynamics model that reproduces a number of experimentally measured quantities like the electrophoretic mobility and the electrostatic influence on the persistence length. Building on this success, we use the frictional information to parametrize a continuum model for electrokinetic

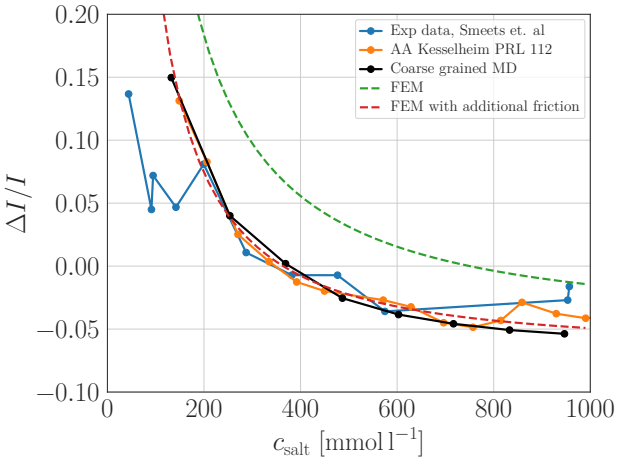

Figure 4.13: The current modulation due to the presence of a single dsDNA strand in a nanopore with diameter $d_{\text{pore}} = 10\,\text{nm}$. The dashed lines show the results of our model with and without additional friction between ions and DNA. Experimental data is taken from Ref. [126], all-atom simulation results from Ref. [47], and coarse-grained simulation results from Ref. [52].

applications, reproducing transport properties from the more detailed models. We applied the continuum model to investigate the pore-size and pore-charge dependence of translocating DNA molecules on the current modulation in glass nanocapillaries. Our continuum model allows us to easily change model parameters and quickly access the effects of such changes.

We showed that depending on the salt concentration, there is only weak to moderate influence of the pore size on the current modulation. We further demonstrated that the current modulation is robust against changes in the surface charge of the pore. This is important because for some experimentally relevant pore types like glass nanocapillaries, the surface charge is significant, but also hard to control. Furthermore, the position of the DNA,

which is fluctuating in the pore during the experiments, has been found to have little influence on the current modulation, except for those situations where the DNA strand is very close to the pore wall.

A possibility to extend this model even further would be to integrate the friction term in a continuum models for flexible DNA like the finite element model by Allison *et al.* [138] However, so far this model could not adequately predict the mobility of DNA. Since our extended coarse-grained DNA model gave good results for the free-draining mobility, such an incorporation of the friction term could potentially improve also other mean-field models. Another obvious path for further investigation is to combine the friction model presented here with more elaborate models for glass nanocapillaries that some authors have used before [50, 51] to investigate, *e. g.*, DNA trapping in capillaries. In this context, it would also be interesting to study more complicated DNA constructs such as DNA origami [131] in more depth.

4.3 Mean-field model for dsDNA origami

The results presented in the following section are part of the following publication:

> Kai Szuttor, Florian Weik, Jean-Noël Grad, and Christian Holm. Modeling the current modulation of bundled DNA structures in nanopores. *The Journal of Chemical Physics*, 154(5):054901, 2021. doi: 10.1063/5.0038530

Model agreement across scales

In the following, we will compare the salt-dependent current modulation for the four aforementioned models (all-atom origami, all-atom quad, coarse-grained and mean-field model). To get a dimensionless number that we can directly compare across the models, we looked at the relative change in ionic current $I_{\mathrm{mod}} = \left(I_{\mathrm{DNA}} - I_{\mathrm{empty}}\right)/I_{\mathrm{empty}}$, where I_{DNA} is the current of

the pore with the DNA origami molecule inside and I_{empty} the current of the empty pore with salt only. As shown in Fig. 4.14, the agreement for the current modulation is very good among the models, taking into account the statistical errors for each model. Especially with regard to the crossover salt concentration $\tilde{c}$ where the relative change in current vanishes ($I_{\text{mod}}(\tilde{c}) = 0$), the results of the four models agree within a small interval of the bulk salt concentration. The fact that a quantitative agreement for these models has already been observed for a single dsDNA molecule in Refs. [47, 76, 53] and the agreement we found in this work for a larger dsDNA bundle structure, suggests that our models would also show consistent results for larger bundle structures, *e. g.* for a system of 4-by-4 helices as investigated by Wang *et al.* in Ref. [31] (*cf.* Fig. 4.18).

In order to investigate the location dependent contribution to the current modulation, the relative current density modulation across the pore $j_{\text{mod}} = \left(j_{\text{DNA}} - j_{\text{empty}}\right)/j_{\text{empty}}$ (naming convention as for I_{mod}) is shown in Fig. 4.15. In case of the all-atom and the coarse-grained model, the current density for the empty pore has been radially averaged to reduce the noise. For the all-atom quad model, we additionally averaged the current density data for the filled pore by rotating the data by $N\pi/2$ with $N \in \{1, 2, 3\}$ around the pore center, leveraging the D_4 symmetry group of the model's geometry. As expected, we observe a negative current density modulation in the area where the DNA helices are located due to blockage and friction with the ions. In the case of the all-atom origami model, the footprints of the inter-helix connections are visible and neutralize the modulation within a small area. For this model j_{mod} is larger in the pore center than between two adjacent helices whereas in the case of the all-atom quad model it is the other way around. The two coarser models (coarse-grained and mean-field) without inter-helix connections both show a very similar current density modulation profile compared to the all-atom quad model.

Since the current modulations for all investigated systems show a very good agreement (*cf.* Fig. 4.14), the differences in the current density modulation profiles (*cf.* Fig. 4.15) have to have the following characteristics: local differences between the

models are canceled out by complementary differences in other regions of the pore and these compensating effects either do not depend on the salt concentration *or* depend on it in a way that preserves the ionic current's dependency on the salt concentration.

To investigate the current density in greater detail, we additionally analyzed the components that make up the current density, namely the charge density profile and the ion velocity profiles. The charge density profiles shown in Fig. 4.16 reveal that the all-atom origami system has a slightly higher concentration of charges between adjacent helices but overall the profiles for all four models look very similar. Thus, the charge density profile does not explain the differences in the relative current density modulation we observed for the all-atom origami model (*cf.* Fig. 4.15).

The velocity profiles for the molecular dynamics systems (as described in Sec. 3.1, 3.1, 3.2) can be directly computed from the trajectories of the ions. Ion velocities [2] for the mean-field model have been obtained via the following expression:

$$v_i(x,y)^z = \frac{j_i(x,y)^z}{c_i(x,y)} = \frac{u(x,y)^z + \mu_i e z_i E^z}{\alpha\mu\omega(x,y) + 1}. \tag{4.2}$$

A detailed explanation of the notation can be found in Sec. 3.3.

All velocity profiles shown in Fig. 4.17 are normalized with the respective average ion velocity in the empty pore, thus enabling the direct comparison of the data for the different models. While the velocity profiles for the anions do not show a significant deviation among the models, more prominent differences are visible between the cation (counter-ion) velocity profiles of the all-atom origami and all-atom quad model. Here, the cation velocity in the origami model is larger at the pore center compared to the region between adjacent helices. On the other hand, the opposite relation is observed for the quad model. These differences in the velocity profiles together with the charge density data shown in Fig. 4.16 thus explain the relative current modulation differences between those two models.

[2] The impression of different pore diameters is an interpolation artifact due to different bin sizes.

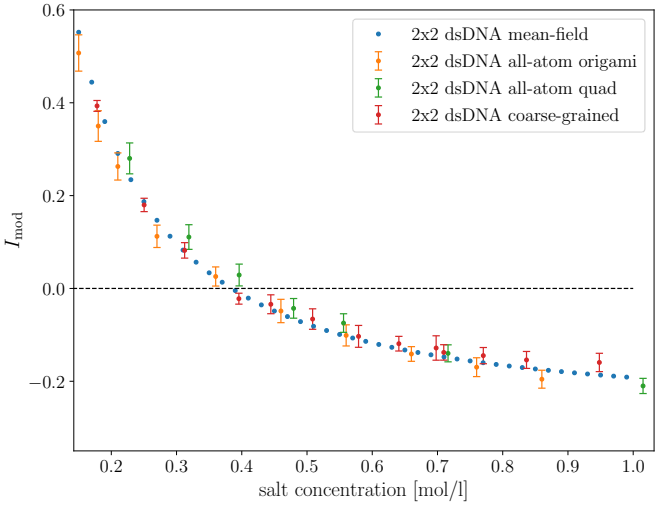

Figure 4.14: Relative change in ionic current through the nanopore for all four investigated models for a 2-by-2 dsDNA bundle. The results of all models agree within errors over the whole range of investigated salt concentrations.

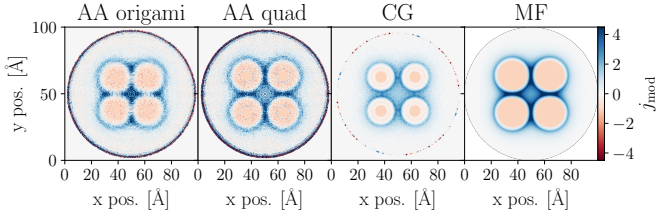

Figure 4.15: Relative current density modulation for the all-atom (left), the coarse-grained (mid) and the mean-field model (right). The non-vanishing modulation at the pore walls for the all-atom and coarse-grained models can be attributed to large current density fluctuations and poor statistics. The salt concentration for all models was approx. $0.18\,\mathrm{mol\,l^{-1}}$.

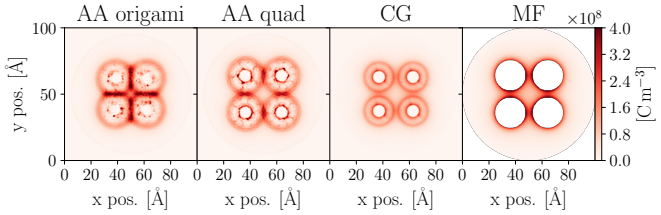

Figure 4.16: Charge density profiles for the all-atom origami, the all-atom quad, the coarse-grained and the mean-field model at approx. $0.18\,\mathrm{mol\,l^{-1}}$.

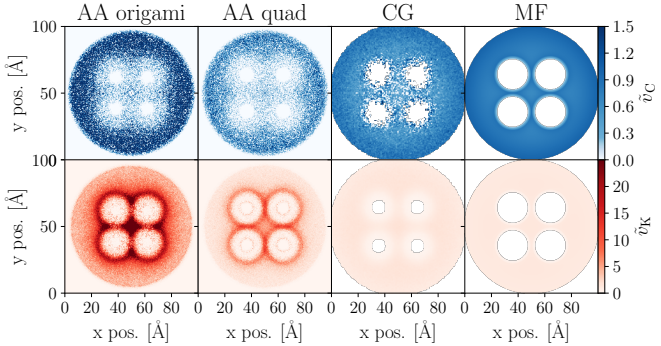

Figure 4.17: Normalized ion velocity profiles for the anions (top row) and the cations (bottom row) at a salt concentration of approx. $0.18\,\mathrm{mol\,l^{-1}}$. The velocities are normalized with the respective empty pore ion velocities in order to get directly comparable dimensionless values.

Comparison to experimental data

The group of Ulrich Keyser in Cambridge performed experiments in a similar setting [31]. They conducted translocation experiments using conical glass nanocapillary pores immersed in solutions of KCl. These nanopores had a mean pore diameter of 14.2 nm. For comparison, we used 10 nm diameter pores in the simulations. However, as shown in a previous publication [53] the pore size does not significantly influence the current modulation. The DNA origami molecules of Ref. [31] have been designed and assembled of 4 or 16 parallel dsDNA double-helices connected by periodically repeating crossover staple strands. Any possible occurrence of electroosmotic flow due to the charged glass walls has been suppressed by adding a tuned amount of polyethylene glycol. Wang *et al.* reported a much smaller crossover salt concentration $\tilde{c}$ ($128\,\mathrm{mmol\,l^{-1}}$ for the 2-by-2 origami and $310\,\mathrm{mmol\,l^{-1}}$ for dsDNA) compared to similar experimental setups where dsDNA translocation has been investigated [137]. Furthermore, they found a non-monotonic behavior of $\tilde{c}$ with respect to the size of the analyte: $\tilde{c}_{\mathrm{dsDNA}} > \tilde{c}_{\text{2-by-2}} < \tilde{c}_{\text{4-by-4}}$, *i. e.* the crossover salt concentration for 4-by-4 origami molecules is reportedly higher ($183\,\mathrm{mmol\,l^{-1}}$) than for the smaller 2-by-2 origami. From all-atom simulations of an infinite pore system [47] with a dsDNA molecule it is known that the ionic current is determined by two competing effects: (i) reduction in current due to friction between ions and DNA helices, and (ii) enhanced current due to additional mobile (counter-) ions. The relative importance of these effects for the overall current modulation depends on the bulk salt concentration of the electrolyte and is non-trivial.

Since we now can safely assume that the frictional effects add up linearly, we also investigated a 4-by-4 origami with our mean-field model. An overview of the salt dependent current modulation for different experimental systems and simulation models is shown in Fig. 4.18. The data labeled as "mean-field" in the plot legend refers to the respective model as described in Sec. 3.3 with varying numbers of charged cylinders representing the different numbers of DNA helices in the model. The current modulation of the three mean-field systems shows a slight monotonic trend to-

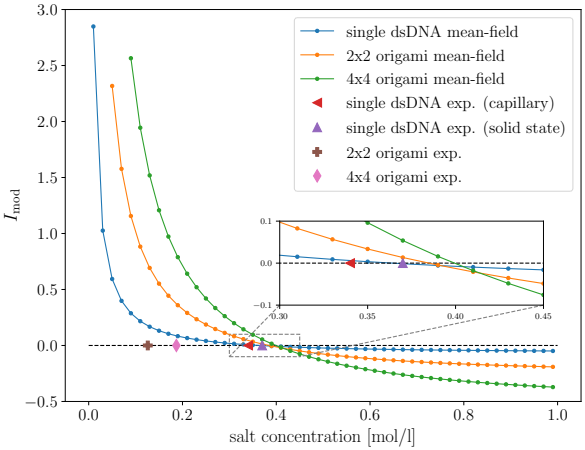

Figure 4.18: Comparison of the current modulation for different setups. Experimental data taken from Refs. [126, 31].

wards higher crossover salt concentrations for larger DNA structures (*cf.* inset of Fig. 4.18) whereas the experimental results show a large drop of $\tilde{c}$ to smaller salt concentrations from a dsDNA molecule to the 2-by-2 origami. Furthermore, the 4-by-4 origami shows an increased value for $\tilde{c}$ compared to the 2-by-2 in the experiments of Wang et al. [31]. Thus, all of our simulation results show a significant deviation for all origami systems despite being accurate for the case of a single DNA molecule as has been shown in Refs. [47, 52, 76, 84].

Comparing the experimental setup to our simulation models, we presume deviations to result from one or combinations of the following simplifications in our models: the pore entrance and the finite molecule lengths are neglected, an alignment of the molecule's symmetry axis with the pore axis is assumed, and the lateral position of the DNA structure's symmetry axis is fixed to the pore center.

Regarding the finite pore and analyte effects, a possible deviation might be expected since the 2-by-2 origami molecule and the 4-by-4 origami molecule are folded from the same scaffold

strand and therefore have a different aspect ratios which may be related to the non-monotonic effect of the molecule's apparent blocking area on the crossover salt concentration. Moreover, Ref. [31] speculates about the possibility of a diffusion limited current through the origami structure.

Another possibility is that tilted conformations of the origami molecules might occur that may lead to a higher effective friction between ions and origami and the pore. As the simulations show (*cf.* Fig. 4.15), the highest current density is in the counter ion layer around the helices. If these layers come closer to the pore walls, this might also lead to a reduction in pore conductivity. However, due to the like-charge repulsion of the glass capillary and the DNA molecule, we expect this effect to be minor.

The dependency of the pore conductivity on the position of a single dsDNA molecule has already been investigated for the mean-field model in Ref. [53]. No significant influence of the molecules position on the pore conductivity had been found unless the gap between the DNA molecule and the pore wall is smaller than the Debye length. Since the Debye length is $\approx \frac{1}{10}$ pore diameter at the experimentally reported crossover salt concentration, we do not expect this effect to be significant. Also, our current density profiles show that a non-negligible portion of the current stems from ions inside the DNA structure which is not directly influenced by the pore walls.

Conclusion

We presented a thorough investigation of four simulation models for the current modulation of bundled DNA nanostructures. The coarse-grained and mean-field models were parametrized only for a *single* dsDNA molecule. Although the level of detail is ranging from the all-atom scale to the mean field scale, we observe a very good agreement among the models with respect to the salt dependent current modulation in a nanopore. This means that the frictional effects are additive for the nanostructures which opens up the door to build arbitrarily large DNA bundles from dsDNA . Spatially resolving the current density across the pore revealed slight different ion mobilities at the center of the pore.

While the ion mobilities for the coarse-grained model and the mean-field model are very similar, the all-atom origami model shows a higher ion mobility at the center of the DNA nanostructure. The difference in the current density in the pore center, however, is compensated by slight differences between adjoint helices in the structure. In summary, our study shows that the current modulation for an infinite pore system is robust against changes to molecular details.

Furthermore, we compared our results to recent experiments by Wang *et al.* [31] This comparison revealed a significant mismatch of the crossover salt concentrations between our models and experimental results (*cf.* Fig. 4.18). Compared to a single dsDNA molecule, the experimental results show a much lower ionic current if the bundled DNA structure is in the pore [31]. Wang *et al.* suggested this to be a non-linear effect of the overlapping ion-DNA frictional interaction near the bundled DNA structures. However, we do not observe such a drop in the current density within the structures but a significant increase (compared to the bulk) either between adjoint helices (all-atom quad, coarse-grained and mean-field model) or at the pore center (all-atom DNA origami). The two other possible suggestions for the current reduction in Ref. [31], namely the idea of a diffusion limitation and end-effects in the pore, cannot be investigated with the models presented here.

A possible way of further investigations could be a model with finite pore and analyte. Such a model is presented in Sec. 3.4 and the corresponding results in Sec. 4.4.

4.4 Mean field model of a finite pore-DNA system

The results presented in the following section are part of a draft for a publication that has not been submitted at the time of writing.

The central physical quantity of interest is the ionic current through the DNA nanopore system. In analogy to previous ex-

perimental and theoretical studies [126, 31, 53, 82], we define the following pore length independent current modulation:

$$I_{\mathrm{mod}} \coloneqq \frac{I_{\mathrm{filled}} - I_{\mathrm{empty}}}{I_{\mathrm{empty}}}, \tag{4.3}$$

where I_{filled} is the ionic current through the pore if a test molecule is present in the pore and I_{empty} is the empty pore current. In Fig. 4.19, the ionic current modulation is shown as a function of the DNA length for different electrolyte bulk concentrations. There is a significant drop in the modulation for shorter DNA molecules if the molecule length falls below the pore length.

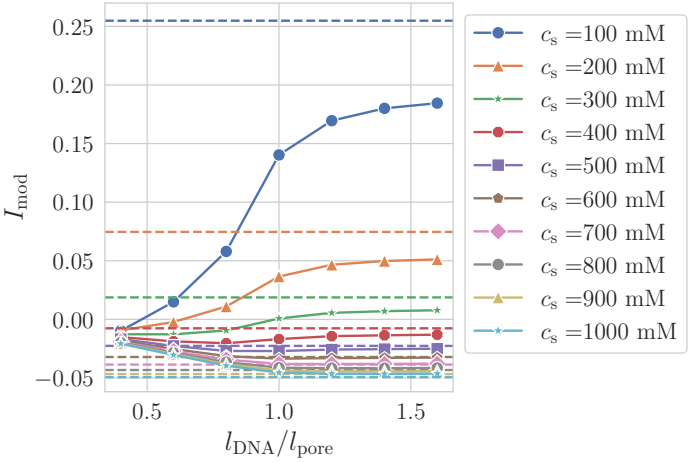

Figure 4.19: The ionic current modulation as a function of the DNA molecule's length for different salt concentrations. The length of the nanopore is 40 nm. The dashed lines show the current modulation for an infinite pore (taken from results for the model as presented in Ref. [53]).

Comparing the current modulation to data from the infinite pore model of Ref. [53] (*cf.* Fig. 4.20), the curves for the finite pore seem to converge towards the infinite pore reference for

increasing ratios of $l_{\mathrm{DNA}}/l_{\mathrm{pore}}$. The differences in the modulation are larger for shorter molecules and smaller salt concentrations. Consistent with results from all-atom simulations of an infinite

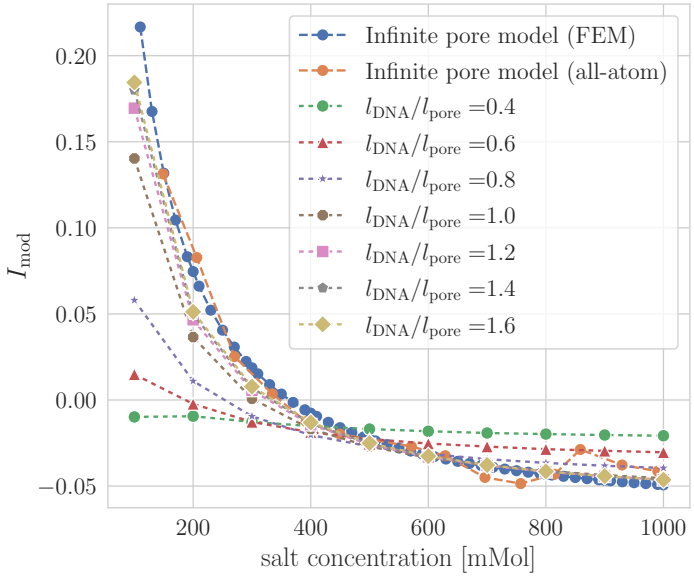

Figure 4.20: The ionic current modulation as a function of salt concentration different DNA molecule lengths. The data is also compared to results from two infinite pore models on the mean-field level [53] and the atomistic level of detail [47].

pore system as presented in Ref. [47], the ionic current through the pore is dominated by the direct contribution caused by the applied electric field (*cf.* Eq. (4.4)). As can be seen in Fig. 4.21a, the advective current fraction due to electroosmotic flow along the DNA is at most in the order of 5–6 percent. Notably, the ionic current's dependency on the DNA length has its maximum for the lowest salt concentration, *i. e.* where the negatively-charged surface is screened least. This is in line with the salt-dependent

ionic current modulation in experimental systems [126, 31] and simulation studies [47, 53, 82] of similar systems in which the current modulation diverges in the limit of zero bulk electrolyte concentrations.

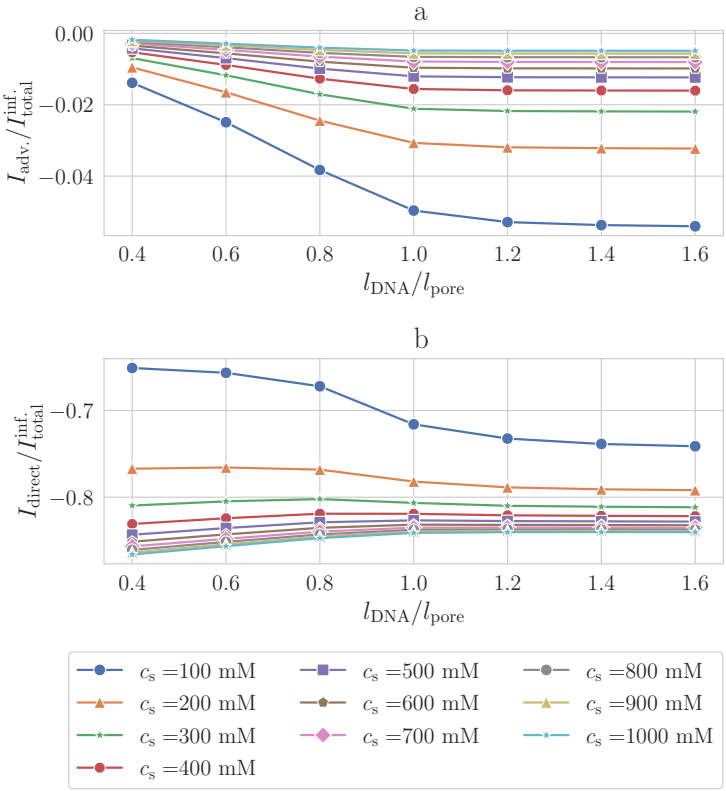

Figure 4.21: The advective (a) and direct (b) contributions to the ionic current as a function of the DNA length.

Because of the much larger influence of the direct current on the total current modulation, we focus further analysis on the electric field and the amount of charge in the pore since these quantities actually define the direct current density (neglecting

constants):

$$j^z_{\text{direct}}(r,z) = \frac{\mu e^2 E_z(r,z)\left[c_+(r,z)+c_-(r,z)\right]}{\alpha\mu\omega(r,z)+1}, \tag{4.4}$$

where we reused the notation of Eq. 3.35.

In order to investigate the electric field's dependency on the DNA length we radially averaged the z-component of the field at the center of the pore ($z = 0$ and $r \in \left[r_{\text{DNA}}, r_{\text{pore}}\right]$). Along this horizontal line, the electric field vanishes for symmetry reasons if no external field acts on the mobile charges of the system. However, as can be seen in Fig. 4.22 if an external field is applied we observe a significant modulation of the electric field along the pore as a function of the DNA length for small electrolyte concentrations. In the most intuitive picture on the level of an equivalent circuit model for the DNA nanopore system the DNA acts as an increased resistance in the pore and the total resistance of the DNA increases with its length. Thus, a larger portion of the potential drops along the DNA which increases the electric field in the pore. However, as Fig. 4.19 shows, the DNA actually enhances the current in the pore (for bulk electrolyte concentrations up to around $400\,\text{mmol}\,\text{l}^{-1}$). Therefore, this simplified picture can not explain our observation of an increased electric field.

The external electric field induces an electric dipole field caused by the polarized counter-ion cloud around the negatively charged DNA that weakens the externally applied field in the pore. Fig. 4.23 shows the dependency of this dipole moment on the DNA length. Here, again we see a significant dependency on the DNA length for low salt concentrations. In addition, the induced dipole moment decreases with the salt concentration. Intuitively one might think that a larger dipole moment would lead to a larger opposing field and therefore a weaker total field in the pore center. The dipole electric field in the pore center, however, also depends on the locations of the charges.

In the following, we want to develop a simple model to get a better understanding of what the induced dipole moment's data actually means for the electric field in the pore. In this

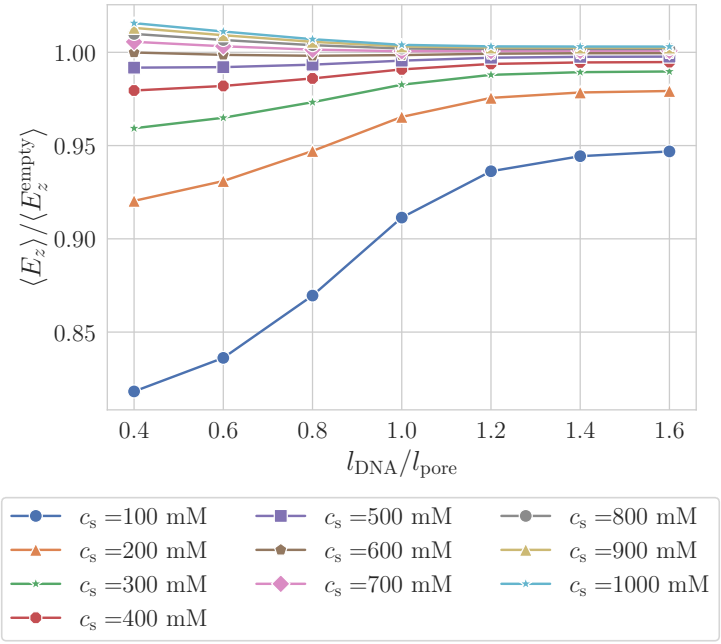

Figure 4.22: The average z-component of the electric field in the center of the pore as a function of the DNA length normalized by the average z-component of the electric field in the center of an empty pore.

model we assume that all electrostatic effects of the mobile ions and the negatively charged DNA are included in the resulting electric dipole field. We therefore calculate the electric field of two charges that are located at the two ends of the DNA on the symmetry axis of the system at $(\pm 0.5 l_{\text{DNA}})$. This results in an electric field in the center of the pore (*cf.* Sec. 3.4):

$$E_z^{\text{dipole}}(r, z = 0) = \frac{2\,|P_z|}{\pi \varepsilon_0 \varepsilon_r \left(l_{\text{DNA}}^2 + 4r^2\right)^{\frac{3}{2}}}, \tag{4.5}$$

where P_z is the induced dipole moment, ε_0 is the vacuum permit-

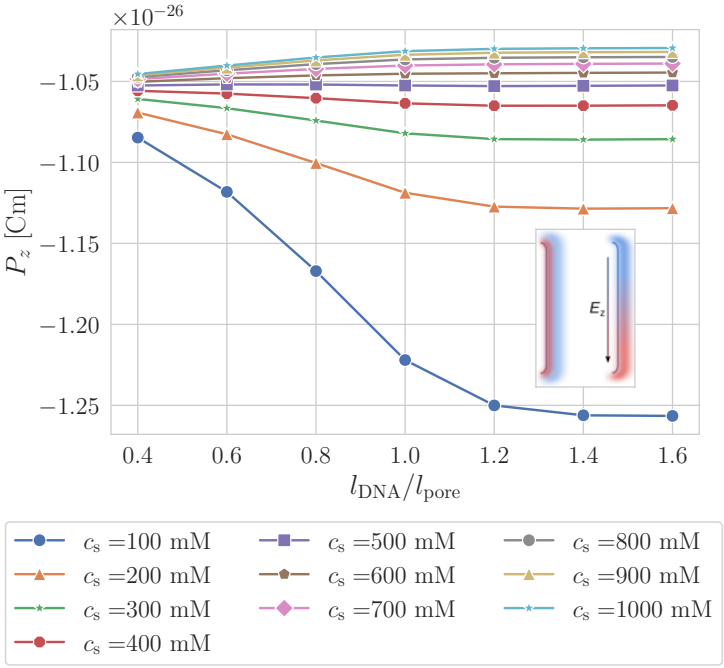

Figure 4.23: The z-component of the total electric dipole of the whole simulation domain. The inset image shows a sketch of the ion cloud around the charged surface of the DNA: the external field induces an asymmetry in the mobile ion distribution.

tivity and ε_r is the permittivity of water. The resulting electric field radially averaged over the pore at $z = 0$ decreases with increasing DNA length (*cf.* Fig. 4.24) which explains the observation of an increasing total electric field in the pore center: the decreasing electric field strength of the induced dipole has less influence on the total electric field for longer DNA molecules. In addition, there is a reduced influence of the electric field on the DNA length for increasing electrolyte concentrations. From $c_s \approx 700\,\mathrm{mmol\,l^{-1}}$ on the DNA charge seems to be completely screened. For these high salt concentrations the DNA can be

seen as an additional resistor, therefore causing a higher portion of the electrostatic potential to drop along the DNA which is equivalent to a larger electric field strength.

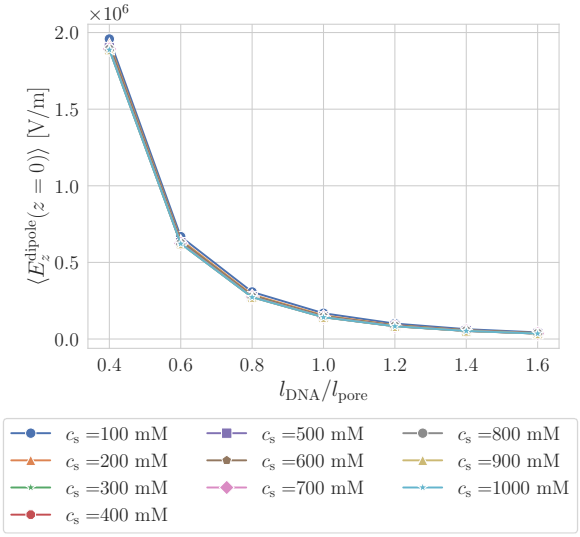

Figure 4.24: The average z-component of the electric field caused by a single

The second contributing factor to the direct current is the total charge in the pore. Therefore, we analyze the DNA length's influence on the ion density in the pore. In the pore, the presence of the negatively charged DNA repels the co-ions and attracts the counter-ions. In addition, this effect is enhanced for longer DNA molecules. The total ion density in the pore, however, is enhanced (compared to the reservoir) and increases with the length of the DNA. Therefore, the repulsion of co-ions is overcompensated by the attraction of the counter-ions (*cf.* Fig. 4.25). This observation is in line with the overall observation of a larger ionic current through the pore for electrolyte concentrations of up to about $400\,\mathrm{mol\,l^{-1}}$. We additionally analyzed the density of the two ion species in the pore. The co-ions of the dsDNA are re-

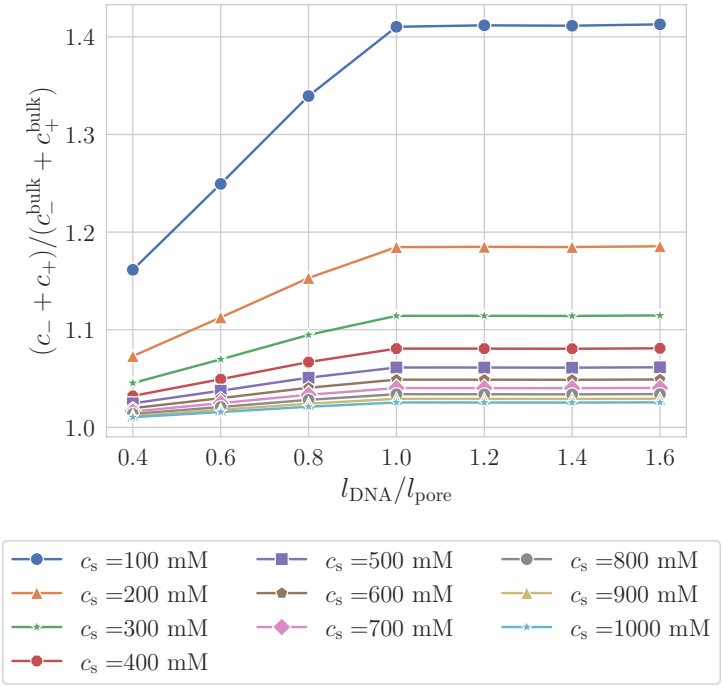

Figure 4.25: The averaged total ion density in the pore normalized with the respective bulk values as a function of the DNA length.

pelled from the pore and the density is well below the bulk value for all investigated DNA lengths and salt concentrations. The cation density, however, is enhanced in the pore and increases with the length of the DNA (*cf.* Fig. 4.26).

Conclusion

We have shown that the current modulation of analytes in nanopore sensing setups significantly depends on the length of the translocating charged object if the length of the object is shorter than

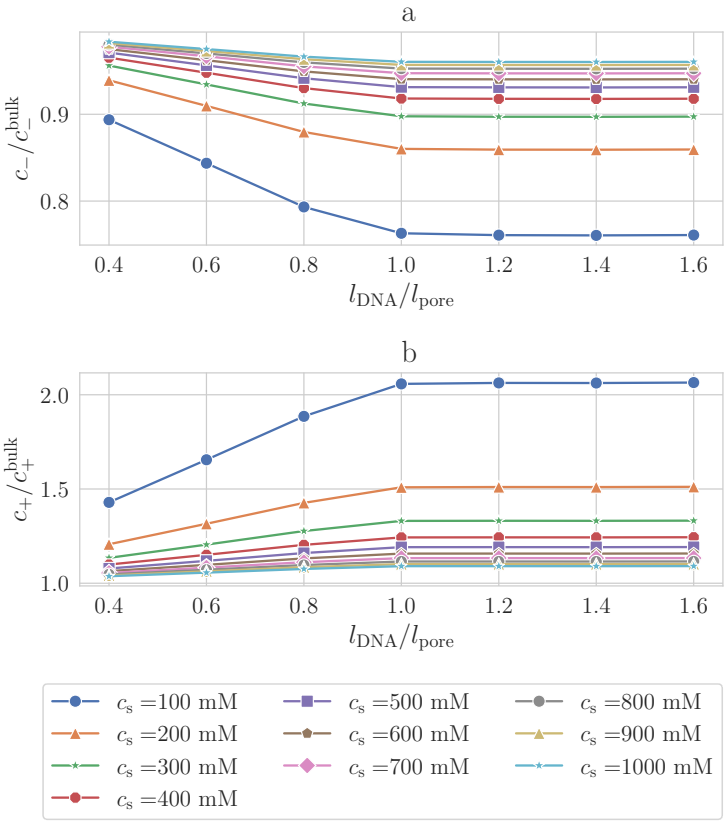

Figure 4.26: The average anion (a) and cation density (b) in the pore normalized with the respective bulk values as a function of the DNA length.

the sensing length of the pore for electrolyte concentrations up to about 400 mmol l^{-1}. Our model in this work extends a previously studied mean-field model [53] for an infinite dsDNA molecule in an infinite pore to a model that includes a finite pore and the cis- and trans-reservoirs of the Coulter-type sensing setup. Our data shows that the ionic current increases with the length of

the DNA and converges to values of infinite pore models as presented in Refs. [47, 76, 53, 82]. Furthermore, we investigated the underlying electrostatic effects, namely the length-dependent opposing electric field that results from the polarized ion cloud around the DNA. This dipole field's component parallel to the pore gets smaller for an increasing DNA length which leads to an overall increasing electric field in the pore. Such effects are not present our infinite pore models for DNA origamis as presented in Ref. [82] which might explain the deviation between the simulation data of these models and experimental results of Wang *et al.* [31].

Chapter 5

Outlook

5.1 Mean-field model

Finite pore model for DNA origamis

There are mainly two possibilities to develop an axisymmetric model for the DNA origami in a finite pore. Either the volume or the surface area of the multi-cylinder origami model as shown in Fig. 5.2 (adapted from Ref. [82]) can be mapped to an axisymmetric single (hollow) cylinder geometry.

Mapping the volume Mapping the volume is equivalent to mapping the cross-section area for a fixed length molecule. The surface area of the four cylinders of the 2-by-2 origami is $A_{2-\mathrm{by}-2} = 4\pi r_{\mathrm{DNA}}^2$. The axisymmetric mapping to a single cylinder is found by solving the following algebraic equation:

$$\begin{aligned} \pi r_{\mathrm{origami}}^2 &= 4\pi r_{\mathrm{DNA}}^2 \\ \Leftrightarrow r_{\mathrm{origami}} &= 2r_{\mathrm{DNA}}, \end{aligned} \tag{5.1}$$

where r_{origami} is the radius of the cylinder for the axisymmetric origami model. For the origami molecules we assume the respective line charge density $\lambda_{\mathrm{origami}}$ to be scaled by the number of helices. Therefore, the surface charge density $\sigma_{\mathrm{origami}}$ of the

single cylinder representation is:

$$\sigma_{\text{origami}} = \frac{\lambda_{2-\text{by}-2}}{2\pi r_{\text{origami}}} = 2\sigma_{\text{dsDNA}}. \tag{5.2}$$

With this mapping of the geometry and surface charge, the friction between the ions and the cylinder surface can be tuned such that the salt concentration of vanishing ionic current modulation through the pore matches to the results from the four single cylinders.

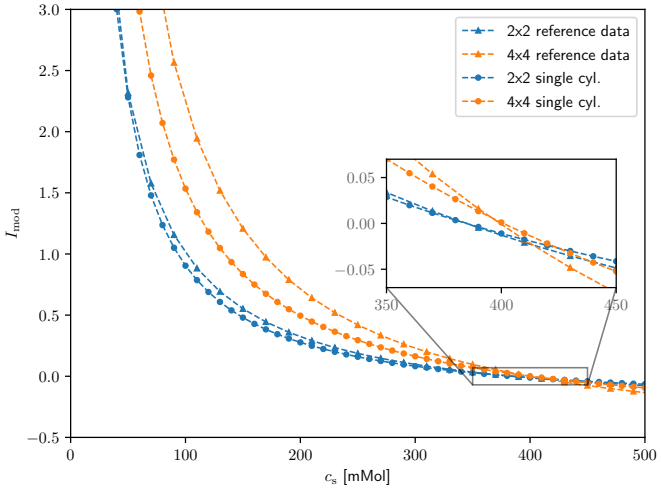

Figure 5.1: Current modulation for the two models of a single cylinder representing the origami molecules with 2-by-2 and 4-by-4 double-stranded helices. The friction prefactor has been tuned for a single salt concentration to optimize for a matching cross over salt concentration. $\alpha_{2-\text{by}-2} = 2.81 \times 10^{-11}\,\text{kg}\,\text{s}^{-1}$, $\alpha_{4-\text{by}-4} = 2.0 \times 10^{-11}\,\text{kg}\,\text{s}^{-1}$.

Mapping the surface area Similarly, the four cylinder origami model can be mapped to an axisymmetric hollow cylinder with

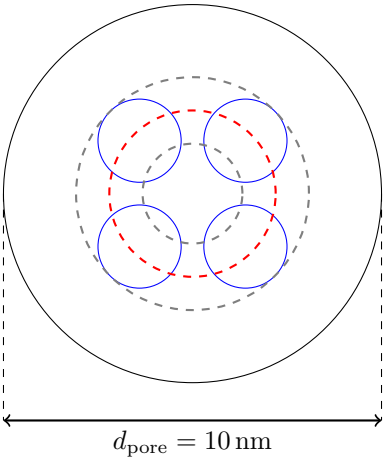

Figure 5.2: The mapping of the four cylinder DNA origami model: either the volume is matched to a single cylinder (red dashed line) or the surface is matched to a hollow cylinder (gray dashed line).

the same surface area. Mapping the surface area is equivalent to matching the circumference of the four single cylinders to the sum of the circumference of the enveloping cylinder plus the circumference of the inner cylinder of the hollow cylinder. The radius for the enveloping cylinder is found to be $\tilde{r}^{\text{outer}}_{\text{origami}} = \sqrt{2}\,(r_{\text{DNA}} + 0.5d) + r_{\text{DNA}}$ (*cf.* Fig. 5.3). The radius for the inner cylinder is then defined by:

$$\begin{aligned}\tilde{r}^{\text{inner}}_{\text{origami}} &= \frac{C_{\text{origami}} - 2\pi\tilde{r}^{\text{outer}}_{\text{origami}}}{2\pi} \\ &= \frac{8\pi r_{\text{DNA}} - 2\pi\left[\sqrt{2}\,(r_{\text{DNA}} + 0.5d) + r_{\text{DNA}}\right]}{2\pi} \\ &= 4r_{\text{DNA}} - \left[\sqrt{2}\,(r_{\text{DNA}} + 0.5d) + r_{\text{DNA}}\right],\end{aligned} \tag{5.3}$$

where C_{origami} is the summed circumferences of the four cylinder origami. The surface charge density for this mapping is then the

same as for a single DNA helix which might be a more realistic mapping due to the importance of the friction between ions and the DNA/origami surface.

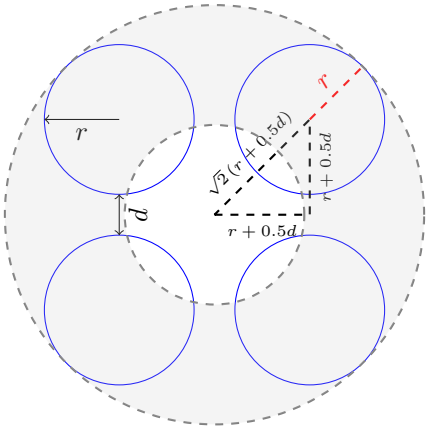

Figure 5.3: The axisymmetric hollow cylinder model for a 2-by-2 origami molecule. The radius of the enveloping circle is $\tilde{r}^{\text{outer}}_{\text{origami}} = \sqrt{2}\,(r + 0.5d) + r$ where the subscript of the DNA radius has been ommited for sake of brevity and d denotes the gap between the surfaces of the DNA cylinders.

Influence of the molecule position along the symmetry axis in the finite pore system Until now the finite pore system has only been investigated for a single position of the DNA centered in the pore. However, since there is an inherent asymmetry in the system caused by the negative surface charge density on the DNA it might be of interest to investigate the influence of varying but fixed molecule positions along the symmetry axis on the ionic current modulation. This might give a more detailed insight into the time dependent current signals that are measured in experiments, *e. g.* how far outside the pore does the DNA significantly influence the current in the pore. An answer to this questions might make it possible to map the current sig-

nal to positions of the molecule in the pore, an information that is experimentally not directly accessible.

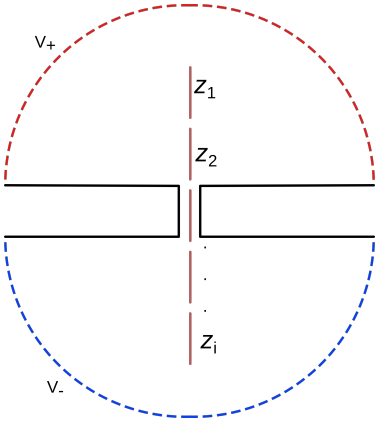

Figure 5.4: Sketch for investigations of different z positions of the molecule along the symmetry axis. For each position z_i a steady state simulation may be done and the current through the pore is measured.

Fig. 5.5 shows preliminary results for the position dependent ionic current modulation through a nanopore with a length of 40 nm and a diameter of 10 nm at a bulk electrolyte concentration of 100 mmol l^{-1}. There is a significant modulation at positions where the DNA end enters the pore and where it leaves the pore. Notably, this modulation is about a factor of five larger than the modulation observed for a completely filled pore. However, since this high modulation is only observed for a relatively short part of the translocation of about 20 nm the sampling frequency of experimental setups need to be sufficiently large to capture such effects. The translocation speed of a DNA through a solid state nanopore is about 1×10^6 bp s^{-1}-1×10^8 bp s^{-1}, *i. e.* $v = 0.34\,\mathrm{mm\,s^{-1}} - 34.0\,\mathrm{mm\,s^{-1}}$ [139, 140]. That means that the time interval that has to be resolved in the experiment is about $\Delta t = \frac{\Delta z}{v} \approx 0.588\,\mu\mathrm{s} - 5.88\,\mu\mathrm{s}$. Therefore, to sufficiently sample these events a sampling rate of about 1.7 MHz-17 MHz would

be necessary. In some publications the ionic current is sampled with a much smaller frequency, *e. g.* 250 kHz in Ref. [30]. In Ref. [141] a very high sampling rate of up to 10 MHz has been used to measure the ionic current. However, they used a very short pore combined with a large bias potential across the pore which results in electric fields that are 1-2 orders of magnitude larger than the fields investigated in this work ($1 \times 10^6\,\mathrm{V\,m^{-1}}$). In addition, Shekar *et al.* [141] investigated single stranded DNA for which we expect the entrance effects to be smaller due to the reduced line charge density compared to dsDNA.

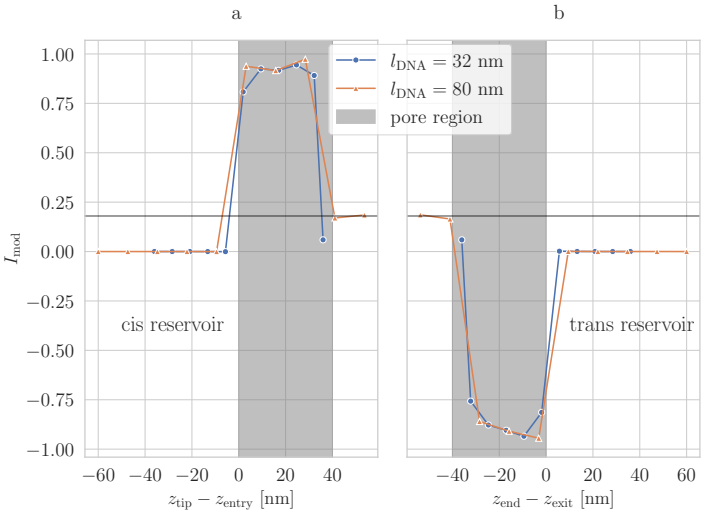

Figure 5.5: The ionic current modulation as a function of the distance between the DNA tip and the pore entry (a) and as a function of the distance between the DNA end and the pore exit (b) for two different DNA lengths.

Chapter 6

Conclusion

The key point of this dissertation is the investigation of the ionic current modulation of DNA structures in nanopores by means of computer simulations.

After having covered the necessary theory to understand the basic physics and the biological impact of DNA and important concepts in the context of DNA nanopores systems in Chapter 2 the three different DNA modeling approaches are discussed in Chapter 3. More precisely, three DNA models with a varying degree of molecular details have been presented ranging from an all-atom description to a coarse-grained model and finally to a mean-field model. Technically, these models are implemented within the framework of molecular dynamics (all-atom and coarse-grained) and using finite-element simulations (mean-field). These models have been used two-fold: first, as a model for a double-stranded DNA helix as a reference model to validate against readily available experimental data, and, second, as a building block for the simulation of more complex multilayer DNA origami structures. Common to all reference models has been that none of them took finite pore or finite DNA effects into account. Therefore, these models assumed a translational symmetry along the pore and DNA. In addition, a realistic model for an all-atom DNA origami has been described in Chapter 3 as well as the extension of the mean-field DNA nanopore model to explicitly incorporate finite size effects.

A detailed description of the investigations for the different DNA nanopore systems has been given in Chapter 4. First, the validation for the re-implementation of the coarse-grained model has been shown alongside the investigation of a finite pore system and the comparison of systems with conical and cylindrical pores. These results revealed a substantial sampling issue of finite pore systems that explicitly contain the electrolyte reservoir due to the computational costs that are connected to systems with many charged particles. Also, the fact that in these systems the electric field outside the pore is nearly zero and the DNA has to arrive at the pore by diffusion which adds to the aforementioned sampling issues. Thus, investigations of the finite pore systems via coarse-grained molecular dynamics simulations had been done for the case of no excess salt only. Here, the conical pore showed a slightly higher conductivity as expected from geometrical reasons. Interestingly, these simple systems already hinted to an asymmetry in the ionic current as a function of the DNA position comparing the cis- and the trans-reservoir pore entries.

This motivated us in the next step to employ a mean-field model that has previously been described and compared to existing data for the ionic current modulation in Chapter 4. Furthermore, due to the low computational costs of this low resolution model several parameter studies like the investigation of the influence of varying DNA positions in the pore's cross-section as well as the influence of a charged pore wall on the ionic current through the pore had been possible. These parameter studies revealed that the crossover salt concentration only weakly depends on such changes and is only affected for the extreme cases where, *e. g.* the DNA being very close to the pore wall such that the counter-ion layer is in close contact with the pore wall. The influence of a charged pore wall could only be observed for low salt concentration that had been significantly lower than the crossover salt concentration.

Following the rigorous investigation of the mean-field model for a single double-stranded DNA molecule, an extensive study of a DNA origami nanopore system has been presented in Sec. 4.3. In these studies a quite significant deviation to experimental data

had been revealed. However, in these studies the three different levels of detail (all-atom, coarse-grained and mean-field) did all show a very good agreement with respect to the ionic current modulation through the nanopore among each other. These simulations also revealed that local differences between the models are canceled out by complementary differences in other regions of the pore and these compensating effects either do not depend on the salt concentration or depend on it in a way that preserves the ionic current's dependency on the salt concentration. Nevertheless, these results could not explain data from an experimental study. Therefore, the last section in this chapter had been devoted to the rigorous investigation of results for a finite DNA nanopore system.

Finally, this system revealed a significant dependency of the ionic current through the nanopore on the length of the DNA if the ratio of DNA length to pore length is smaller than unity. To be more specific, we found that an induced electric dipole field reduces the field strength of the externally applied electric field in the nanopore. This dipole field's component parallel to the pore gets smaller for an increasing DNA length which leads to an overall increasing electric field in the pore. Because these effects are neglected in the infinite pore model for DNA origamis their data quite significantly deviates from experimental results.

In summary, it was shown that a modeling approach on multiple scales is necessary for DNA nanopore systems. On the one hand is helps to overcome technical issues in some situations (*e. g.* a high computational cost) and on the other hand it enables the investigation of effects that may not be feasible to be covered by a single model. Also, by investigating models with different levels of detail it is possible to extract the most significant mechanisms that affect electrokinetic transport phenomena in DNA nanopore systems. To give an example, the ion mobility reduction close to the DNA as it has been observed in all-atom simulations enabled us to come up with coarser models of the DNA molecule by adding a phenomenological frictional interaction. On the other hand, the investigations we have done on the DNA length dependency are not feasible within the framework of all-atom simulations because of the very large system sizes

and the corresponding computational costs.

In chapter 5 possible extensions for the mean-field model are described. These extensions include a DNA Origami model, which, due to a simplified geometry with rotational symmetry, could be used to investigate the finite pore effects in two dimensions. Another model could be used to study the translocation process through a finite pore in detail. Here, we were already able to obtain first results, which were not known experimentally so far.

Chapter 7

Zusammenfassung

Im Mittelpunkt dieser Dissertation steht die Untersuchung der Ionenstrommodulation von DNA-Strukturen in Nanoporen mithilfe von Computersimulationen. Im Folgenden wird eine kurze Rekapitulation des Inhalts dieser Arbeit gegeben.

Nachdem die notwendige Theorie, die physikalischen Grundlagen und die biologische Bedeutung von DNA beschrieben wurden sowie wichtige Konzepte im Zusammenhang mit DNA-Nanoporen Systemen in Kapitel 2 eingeführt wurden, werden die drei verschiedenen DNA Modellierungsansätze in Kapitel 3 diskutiert. Genauer gesagt, werden drei DNA-Modelle mit unterschiedlichen molekularen Detailgrad vorgestellt, der von einer atomaren Beschreibung („all-atom “), über ein vergröbertes Modell („coarse-grained“) und schließlich einem Mean-Field-Modell reicht. Technisch gesehen werden diese Modelle im Rahmen der Molekulardynamik (atomares und vergröbertes Modell) und der Finite-Elemente Methode (Mean-Field) umgesetzt. Diese Modelle wurden in zweierlei Hinsicht verwendet: zunächst als Modell für eine doppelsträngige DNA als eine Art Referenzmodell, um es mit leicht verfügbaren experimentellen Daten zu validieren, und zweitens als Baustein für die Simulation von komplexeren mehrschichtigen DNA-Origami-Strukturen. Alle Referenzmodelle haben gemein, dass keines von ihnen Effekte endlicher Poren oder einer endlichen DNA berücksichtigt. Entsprechend nehmen diese Modelle eine Symmetrie entlang der Pore und der DNA an.

Darüber hinaus wurden zwei Erweiterungen entwickelt: zum einen ein realistisches Modell für ein DNA-Origami und zum anderen eine Erweiterung des Mean-Field Modells um endliche Porengeometrien zu simulieren.

Die Ergebnisse zu den verschiedenen DNA-Nanoporen Systemen wurde in Kapitel 4 detailliert beschrieben. Zunächst wird dort die Validierung für die Re-Implementierung des vergröberten Modells sowie die Untersuchung eines endlichen Porensystems und der Vergleich von Systemen mit konischen und zylindrischen Poren dargestellt. Diese Ergebnisse zeigten, dass es für solche Systeme inhärente Schwierigkeiten gibt, eine aussagekräftige Statistik des Translokationsvorgangs zu erreichen. Dies lässt sich für die Systeme mit endlicher Porengeometrie damit begründen, dass das Elektrolytreservoir explizit enthalten ist und damit der Berechnungsaufwand aufgrund der hohen Anzahl geladener Teilchen beträchtlich größer wird. Auch die Tatsache, dass in diesen Systemen das elektrische Feld außerhalb der Pore nahezu Null ist und die DNA durch Diffusion zur Pore gelangen muss, verstärkt die oben erwähnten Probleme der ineffizienten Datengenerierung. Daher beschränkten wir die Untersuchungen der endlichen Poren-Systeme auf vergröberte Molekulardynamik-Simulationen, bei denen nur Gegenionen und keine zusätzlichesnSalz-Ionen vorliegen. Hier zeigte die konische Pore eine etwas höhere Leitfähigkeit, wie es aus geometrischen Gründen zu erwarten ist. Interessanterweise zeigen diese einfachen Systeme bereits eine Asymmetrie im elektrischen Strom als Funktion der DNA-Position, wenn man die cis und die trans Poreneingänge vergleicht.

Im darauffolgenden Kapitel wurden die Ergebnisse für das Mean-Field Modell eines DNA-Nanoporen-Systems beschrieben und mit experimentellen Literaturdaten für die Ionenstrommodulation verglichen. Außerdem wurden aufgrund des geringen Rechenaufwands dieses einfachen Modells verschiedene Parameterstudien unternommen. Zum Beispiel wurde der Einfluss unterschiedlicher DNA-Positionen im Porenquerschnitt sowie der Einfluss einer geladenen Porenwand auf den Ionenstrom durch die Pore untersucht. Diese Parameterstudien zeigten, dass die Crossover-Salzkonzentration nur schwach von solchen Änderungen abhängt und nur in Extremfällen beeinflusst wird, in denen z.B.

die DNA sehr nahe an der Porenwand liegt, sodass die Gegenionenschicht in engem Kontakt mit der Porenwand steht. Der Einfluss einer geladenen Porenwand konnte nur für niedrige Salzkonzentrationen beobachtet werden, die deutlich unterhalb der Crossover-Salzkonzentration lagen.

Nach der rigorosen Untersuchung des Mean-Field-Modells für ein einzelnes doppelsträngiges DNA-Molekül, wurde eine umfangreiche Studie eines DNA-Origami-Nanoporensystems in Kapitel 4.3 durchgeführt. In diesen Studien wurde eine signifikante Abweichung zu experimentellen Daten festgestellt. Allerdings zeigten die Modelle auf den drei verschiedenen Detailebenen (allatom, vergröbert und mean-field) eine sehr gute Übereinstimmung hinsichtlich der Ionenstrom Modulation durch die Nanopore untereinander. Dieses konsistente Bild ließ darauf schließen, dass die im Experiment gemessenen Daten auf Effekte einer endlichen Geometrie zurückzuführen sein könnten. Die Simulationen zeigten auch, dass lokale Unterschiede zwischen den Modellen durch komplementäre Unterschiede in anderen Regionen der Pore ausgeglichen werden und diese kompensierenden Effekte nicht von der Salzkonzentration abhängen, oder aber nur so von ihr abhängen, dass die Abhängigkeit des Ionenstroms von der Salzkonzentration erhalten bleibt. Dennoch konnten diese Ergebnisse die Daten aus einer experimentellen Studie nicht erklären. Daher war der letzte Abschnitt in diesem Kapitel der rigorosen Untersuchung eines Systems mit endlicher Geometrie gewidmet.

Dieses System schließlich zeigte eine signifikante Abhängigkeit des Ionenstroms von der Länge der DNA, wenn das Verhältnis von DNA-Länge zu Porenlänge kleiner als eins ist. Konkret wurde festgestellt, dass ein induziertes elektrisches Dipolfeld die Feldstärke des von außen angelegten elektrischen Feldes in der Nanopore reduziert. Die Komponente dieses Dipolfeldes parallel zur Pore wird mit zunehmender DNA-Länge kleiner, was zu einem insgesamt zunehmenden elektrischen Feld in der Pore führt. Da diese Effekte in dem unendlichen Porenmodell für DNA-Origamis vernachlässigt werden, weichen deren Daten erheblich von den experimentellen Ergebnissen ab.

Zusammenfassend haben wir gezeigt, dass ein Modellierungsansatz auf mehreren Skalen für DNA-Nanoporen-Systeme not-

wendig ist. Zum einen lassen dich dadurch technische Probleme (wie etwa ein hoher Rechenaufwand) umgehen und zum anderen ist die Untersuchung bestimmter Effekte möglich, die von einem einzelnen Modell nicht abgedeckt werden können. So wäre es zum Beispiel nicht möglich gewesen ein System mit explizit modelliertem Elektrolytreservoir auf der voll atomistischen Detailebene in sinnvoller Zeit zu untersuchen. Auf der anderen Seite waren die voll atomistischen Modelle notwendig, um etwa die Annahme der einfachen Überlagerung der Reibungseffekte zwischen Ionen und DNA zu überprüfen. Letztlich ist es durch die Untersuchung von Modellen mit verschiedenen Detaillevel möglich, die wichtigsten Mechanismen zu extrahieren, die zu den beobachteten Effekten der Strommodulation in DNA-Nanoporensystemen führen. Hier zeigte sich, dass sich die Modulation des Stromes als Funktion der Salzkonzentration auch ohne atomare Auflösung modellieren lässt und die verminderte Ionenmobilität durch eine effektive Reibung darstellen lässt.

In Kapitel 5 werden mögliche Erweiterungen für das Mean-Field Modell beschrieben. Diese Erweiterungen beinhalten zum einen ein DNA Origami Modell, mit dem aufgrund einer vereinfachten Geometrie mit Rotationssymmetrie die Effekte durch eine endliche Pore in zwei Dimensionen untersucht werden kann. Ein weiteres Modell könnte den Translokationsvorgang durch eine endliche Pore im Detail untersuchen. Hier wurden bereits erste Ergebnisse gezeigt, die experimentell bisher nicht bekannt waren.

Chapter 8

Appendix

8.1 All-atom simulations

DNA origami

The 2-by-2 DNA origami as it has been investigated in Wang *et al.* [31] is a bundle of 4 double helices that are interconnected by shorter stable strands. The scaffold strand contains 7250 nucleobases. The whole structure is stabilized by 174 shorter staple strands. The exact sequence is listed in Table S9 of Ref. [31]. The whole structure has a translational symmetry along its main axis with a period of 217.6 Å. This unit cell is shown below in Fig. 8.1.

In the all-atom model for the origami structure, a segment of the scaffold strand and 7 staple strands are used: full-length oligomers 9, 10, 67, 119, 150, and fragments of oligomers 66 and 68. The ends of the structure are connected across the periodic boundaries to get a fully periodic molecule that can be used in the context of the infinite pore model as described in Sec. 3.1.

The DNA origami is composed of a main strand with 7250 nucleobases folded in 4 helices and 174 short strands that stabilize the 4 helices. The system is periodic along the z-axis via translation symmetry with translation vector $[0.0\,\text{Å}, 0.0\,\text{Å}, -217.6\,\text{Å}]$. There are no periodic boundaries though, so the molecular system can be described as 27 translation images of the "unit cell"

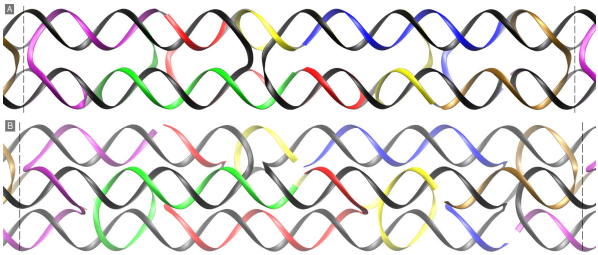

Figure 8.1: The unit cell of the 2-by-2 DNA origami structure from two different perspectives A and B related by a rotation of 45° around the main axis. The dashed lines represent the periodic boundaries. The scaffold strand is colored in black while the 6 linker strands are colored in blue, red, green, yellow, ocher and purple, respectively. This figure is taken from Ref. [82].

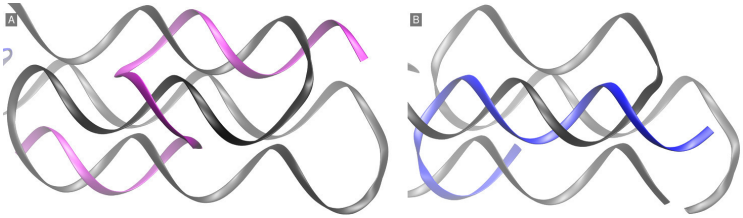

Figure 8.2: Close-up view of the main chain boundaries. The cut is visible in the lower right corner of B.

plus one extra unit cell at both termini where the DNA topology is different. The 174 linker strands can be divided in 6 categories. These are also periodic with 28 translation images, plus 3 linkers at both termini with a different geometry ($28 \cdot 6 + 2 \cdot 3 = 174$). The unit cell is visualized in Figure 8.1. The main strand is cyclic, although it has an artificial cut at one terminus (*cf.* Fig. 8.2B) with just enough space to fit a single phosphate to close the cycle.

8.2 Software Development and Project Organization

During the development of simulation models one is confronted not only with problems that belong to the field of theoretical physics, but also a lot of technical issues come up along the way. Computational physicists are de facto also software developers and therefore face very similar challenges, *e. g.*, achieving a good software-testability, -maintainability and -extensibility. These challenges do not only occur in the context of the software core that implements the algorithmic details for, *e. g.* molecular dynamics, but also in the context of the end-user implemented code that use some interface to the core implementation and thereby implementing the actual representation of a model for a physical system. Some measures that turned out to be quite useful to deal with the aforementioned software development goals are therefore discussed in this section.

Simulation Project Organization

It is a central part in software development in general to incorporate some sort of version control. This brings several advantages, *e. g.* the possibility to easily revert changes or independent development of multiple users or features. In simulation studies it turned out that there is a demand for new features in the simulation core during the development of simulation models. Therefore, the development of the actual simulation also incorporates development on the simulation engine. One way to deal with this dependency of the simulation code on the core project is to use the version control tool git and its *submodule* feature. An example for a simulation project layout could look like the following:

```
./finite_pore
├── .git
├── simulation_frontend
│   └── dna.py
└── simulation_backend
    └── .git
```

```
└── src
```

In this example the shown directory root directory is under version control via git (as indicated by the `.git` directory) as well as the subfolder containing the simulation backend. Expressed in the git framework vocabulary: `simulation_backend` is a git submodule of the simulation project. This layout has the advantages that it is always automatically documented which snapshot of the backend has been used to produce the results of the respective simulation project. This layout may even be extended by another level, *e. g.* for having a collection of related simulation projects combined in a single meta-project containing several simulation projects as git submodules:

```
./nanopore_translocation
├── .git
├── finite_pore
│   ├── .git
│   └── ...
└── dna_in_bulk
    ├── .git
    └── ...
```

This makes it much more easy to handle inter-dependencies on the versions between individual projects. Furthermore, in git projects involving the content of publications the described project layout serves as a documentation for the source of published data and therefore leads to an improved reproducibility of simulation results.

8.3 CGDNA - A python package to set up a coarse grained dsDNA model

The non-trivial python code to set up the geometry and interactions for a coarse-grained DNA model as described in Sec. 3.2, a separate python package has been developed. The advantage is that this programming code can be validated independently of the actual usage in a specific simulation project. The python package (called *cgdna*) contains several submodules with the following structure:

- `base_pair.py`
  This module contains a class that represents a single base-pair. The parameters to this class are the center of mass position, the angle between the basepair and the backbone beads, the distance between the backbone and the basepair and an azimuthal angle orientation.

- `molecule.py` This module contains a class to hold the global parameters for the coarse-grained model like the distance between the base pairs, the dihedral angle the number of base pairs, the number of coupling points for the coupling to the LBM.

- `espresso.py` In this module a class is implemented to hold and validate parameters that are directly consumed by the molecular dynamics software (in this case ESPResSo).

- `cgdna.py` This is the top level module to hold instances of the aforementioned classes and handles queries to access specific particles from the molecule. In addition, it adds the various bonded interactions between the particles and validates them.

Each of the classes contains a detailed documentation directly in the source code. As an example, the doc-string of the top level `cgdna.DNA` class is shown below.

```
class DNA:
    """
    This class is supposed to be used in conjunction with ESPResSo to simulate
    a cgDNA molecule.

    Parameters
    ----------
    system : :class:`espressomd.System` instance
    molecule_params : :class:`cgdna.molecule.Parameters` instance
    espresso_params : :class:`cgdna.espresso.Parameters` instance
    harmonic : :class:`espressomd.interactions.HarmonicBond` instance
        Harmonic potential between consecutive base pair particles.
    angle_harmonic_bp_bp_bp: :class:`espressomd.interactions.AngleHarmonic` instance
        Bond-angle potential between consecutive base pair particles.
    angle_harmonic_bp_bp_bb : :class:`espressomd.interactions.AngleHarmonic`
          instance
        Bond-angle potential between base_pair-base_pair base_pair-backbone
              particles.
    dihedral : :class:`espressomd.interactions.Dihedral` instance
        Dihedral potential.
    with_filling_parts : :obj:`bool`
```

```
        Whether to add filling particles for hydrodynamic coupling (default: True).
```

By implementing so-called mocks for all external classes with which the package has to interact (*i. e.* classes that are part of a dependent package, in this case the ESPResSo package), it's possible to write unit tests for the implementation of the coarse-grained model. This way, it is explicitly expressed what observable behavior is assumed from the dependency. The mocked classes only implement this behavior and no additional business logic:

```
class Particle:
    def __init__(self, **kwargs):
        self.__dict__.update(kwargs)

    def vs_auto_relate_to(self, id):  # pylint: disable=unused-argument
        pass

    def add_bond(self, *args, **kwargs):
        pass


class ParticleList:
    def __init__(self):
        self.particles = []

    def __getitem__(self, item):
        return self.particles[item]

    def __iter__(self):
        return self.particles.__iter__()

    def add(self, **kwargs):
        particle = Particle(**kwargs)
        if id not in kwargs:
            particle.id = len(self.particles)
        self.particles.append(particle)
        return particle


class System:
    def __init__(self):
        self.part = ParticleList()
```

In the following an example for the usage within a simulation setup is shown. An instance of the `cgdna.DNA` class is created and the inertia tensor for every basepair is set by looping over the different particle types of the polymer and extracting the respective information (mass and position). This would have been much more error-prone and hard to validate without the separate implementation of the DNA setup in the separate python package.

```
dna = cgdna.cgdna.DNA(
    system,
    get_molecule_params(p),
    espresso_params,
    harmonic_bond,
    angle_harmonic1,
    angle_harmonic2,
    dihedral_bond,
    True,
)

# inertia tensor
for bp, bb, com in zip(
    dna.base_pair_particles,
    zip(dna.backbone_particles[::2], dna.backbone_particles[1::2]),
    dna.com_particles):
    (
        principal_moments,
        principal_axes,
    ) = espressomd.rotation.diagonalized_inertia_tensor(
        [bp.pos, bb[0].pos, bb[1].pos], [bp.mass, bb[0].mass, bb[1].mass
            ]
    )
    com.rinertia = principal_moments
    com.quat = espressomd.rotation.matrix_to_quat(principal_axes)
```

8.4 Erklärung der Selbständigkeit

Die eingereichte Dissertation zum Thema *Modeling the Translocation of DNA Structures through Nanopores* stellt meine eigenständig erbrachte Leistung dar.

Ich habe ausschließlich die angegebenen Quellen und Hilfsmittel benutzt. Wörtlich oder inhaltlich aus anderen Werken übernommene Angaben habe ich als solche kenntlich gemacht.

Die Richtigkeit der hier getätigten Angaben bestätige ich und versichere, nach bestem Wissen die Wahrheit erklärt zu haben.

Stuttgart, den 9.8.2021

Chapter 9

Acknowledgements

This work would not have been possible without the support of many people around me! The following list of people might be incomplete and I might have forgotten people that actually have been important for this work.

To start off, I want to thank **Prof. Christian Holm** for supporting me in many ways, *e. g.* by pushing forward the scientific progress, discussions on the whiteboard, and of course giving me the opportunity to work in his group in the first place. In addition, he prepared me for the worst case of me failing in science by giving me a thorough education in playing table soccer on a daily basis.

I also want to thank my parents for always supporting me throughout my life and believing in my plans. Without you, I would have probably not managed to be where I am now.

My family, especially my wife **Sonja-Maria** has always motivated me and covered my back! Playing with our kids Johannes, Lena and Emma has been a great way to clear my head.

I also want to especially thank my sister **Katja** who is and has been a persistent adviser and the best childcare at days when I had to make some extra hours at the institute.

Of course, I also met a lot of people at the university and the institute that I want to thank for discussions, help and for making the working time such a pleasure (in no particular order):

- Frank Huber
- Henriette Patzelt
- Simone Blümlein
- Jens Smiatek
- Owen Hickey
- Johannes Zeman
- Jonas Landsgesell
- Jonas Weber
- Kai Philippi
- Patrick Kreissl
- Sascha Ehrhardt
- Stefan Kesselheim
- Konrad Breitsprecher
- Tobias Richter
- Tillmann Kleiner
- Georg Rempfer
- David Sean
- Rudolf Weeber
- Jean-Noël Grad
- Tamal Roy

- Ulrich Keyser
- Michael Kuron
- Maria Fyta
- Christoph Lohrmann
- Alexander Reinauer
- Miru Lee
- Samuel Tovey
- Johannes Hauskrecht
- Alexander Schlaich
- Axel Arnold
- Olaf Lenz
- Florian Weik
- Dominik Röhm
- Florian Dommert
- Shervin Raafatnia
- Claudia Lemke
- Florian Fahrenberger

Bibliography

[1] Laura D. Wood, D. Williams Parsons, Siân Jones, Jimmy Lin, Tobias Sjöblom, Rebecca J. Leary, Dong Shen, Simina M. Boca, Thomas Barber, Janine Ptak, Natalie Silliman, Steve Szabo, Zoltan Dezso, Vadim Ustyanksky, Tatiana Nikolskaya, Yuri Nikolsky, Rachel Karchin, Paul A. Wilson, Joshua S. Kaminker, Zemin Zhang, Randal Croshaw, Joseph Willis, Dawn Dawson, Michail Shipitsin, James K. V. Willson, Saraswati Sukumar, Kornelia Polyak, Ben Ho Park, Charit L. Pethiyagoda, P. V. Krishna Pant, Dennis G. Ballinger, Andrew B. Sparks, James Hartigan, Douglas R. Smith, Erick Suh, Nickolas Papadopoulos, Phillip Buckhaults, Sanford D. Markowitz, Giovanni Parmigiani, Kenneth W. Kinzler, Victor E. Velculescu, and Bert Vogelstein. The genomic landscapes of human breast and colorectal cancers. *Science*, 318(5853):1108–1113, 2007. ISSN 0036-8075. doi: 10.1126/science.1145720.

[2] Wallace H Coulter. Means for counting particles suspended in a fluid, 1953. US Patent 2,656,508.

[3] Marshall Graham. The Coulter principle: For the good of humankind. Master's thesis, University of Kentucky, 2020.

[4] RW DeBlois and CP Bean. Counting and sizing of submicron particles by the resistive pulse technique. *Review of Scientific Instruments*, 41(7):909–916, 1970.

[5] John J Kasianowicz, Eric Brandin, Daniel Branton, and David W Deamer. Characterization of individual polynu-

cleotide molecules using a membrane channel. *Proceedings of the National Academy of Sciences*, 93(24):13770–13773, 1996.

[6] C. Bustamante, S. B. Smith, J. Liphardt, and D. Smith. Single-molecule studies of DNA mechanics. *Current Opinion (Elsevier)*, 10:279–285, 2000.

[7] F. Ritort. Single molecule experiments in biophysics: exploring the thermal behavior of nonequilibrium small systems. *Pramana*, 64(6), 2005.

[8] F Ritort. Single-molecule experiments in biological physics: methods and applications. *Journal of Physics: Condensed Matter*, 18(32):R531–R583, 2006.

[9] B.M. Venkatesan and R. Bashir. Nanopore sensors for nucleic acid analysis. *Nature Nanotechnology*, 6(10):615–624, 2011.

[10] Dvir Rotem, Lakmal Jayasinghe, Maria Salichou, and Hagan Bayley. Protein detection by nanopores equipped with aptamers. *Journal of the American Chemical Society*, 134 (5):2781–2787, 2012.

[11] Murugappan Muthukumar, Calin Plesa, and Cees Dekker. Single-molecule sensing with nanopores. *Physics Today*, 68 (8):40–46, 2015. doi: 10.1063/PT.3.2881.

[12] Kuiama Lewandowski, Yifei Xu, Steven T Pullan, Sheila F Lumley, Dona Foster, Nicholas Sanderson, Alison Vaughan, Marcus Morgan, Nicole Bright, James Kavanagh, Richard Vipond, Miles Carroll, Anthony C. Marriott, Karen E. Gooch, Monique Andersson, Katie Jeffery, Timothy E. A. Peto, Derrick W. Crook, A. Sarah Walker, and Philippa C. Matthews. Metagenomic nanopore sequencing of influenza virus direct from clinical respiratory samples. *Journal of Clinical Microbiology*, 58(1):e00963–19, 2019. doi: 10.1128/JCM.00963-19.

[13] Tim Albrecht. Single-molecule analysis with solid-state nanopores. *Annual Review of Analytical Chemistry*, 12: 371–387, 2019.

[14] Gerald M Cherf, Kate R Lieberman, Hytham Rashid, Christopher E Lam, Kevin Karplus, and Mark Akeson. Automated forward and reverse ratcheting of DNA in a nanopore at 5-Å precision. *Nature biotechnology*, 30(4): 344–348, 2012.

[15] Elizabeth A Manrao, Ian M Derrington, Andrew H Laszlo, Kyle W Langford, Matthew K Hopper, Nathaniel Gillgren, Mikhail Pavlenok, Michael Niederweis, and Jens H Gundlach. Reading DNA at single-nucleotide resolution with a mutant mspa nanopore and phi29 DNA polymerase. *Nature biotechnology*, 30(4):349–353, 2012.

[16] Alexander S Mikheyev and Mandy MY Tin. A first look at the Oxford Nanopore MinION sequencer. *Molecular Ecology Resources*, 14(6):1097–1102, 2014. doi: 10.1111/1755-0998.12324.

[17] T. Laver, J. Harrison, P.A. O'Neill, K. Moore, A. Farbos, K. Paszkiewicz, and D.J. Studholme. Assessing the performance of the Oxford Nanopore Technologies MinION. *Biomolecular Detection and Quantification*, 3:1–8, 2015. ISSN 2214-7535. doi: 10.1016/j.bdq.2015.02.001.

[18] Miten Jain, Hugh E Olsen, Benedict Paten, and Mark Akeson. The Oxford Nanopore MinION: delivery of nanopore sequencing to the genomics community. *Genome Biology*, 17(1):1–11, 2016. doi: 10.1186/s13059-016-1103-0.

[19] Miten Jain, Hugh E Olsen, Benedict Paten, and Mark Akeson. Erratum to: The Oxford Nanopore MinION: delivery of nanopore sequencing to the genomics community. *Genome Biology*, 17(1):256, 2016. doi: 10.1186/s13059-016-1122-x.

[20] Farzin Haque, Jinghong Li, Hai-Chen Wu, Xing-Jie Liang, and Peixuan Guo. Solid-state and biological nanopore

for real-time sensing of single chemical and sequencing of DNA. *Nano today*, 8(1):56–74, 2013.

[21] Chan Cao and Yi-Tao Long. Biological nanopores: confined spaces for electrochemical single-molecule analysis. *Accounts of chemical research*, 51(2):331–341, 2018.

[22] Jiali Li, Derek Stein, Ciaran McMullan, Daniel Branton, Michael J. Aziz, and Jene Golovchenko. Ion-beam sculpting at nanometre length scales. *Nature*, 412(6843):166–169, 2001.

[23] Kimberly Venta, Gabriel Shemer, Matthew Puster, Julio A Rodriguez-Manzo, Adrian Balan, Jacob K Rosenstein, Ken Shepard, and Marija Drndic. Differentiation of short, single-stranded DNA homopolymers in solid-state nanopores. *ACS Nano*, 7(5):4629–4636, 2013. doi: 10.1021/nn4014388.

[24] Harold Kwok, Kyle Briggs, and Vincent Tabard-Cossa. Nanopore fabrication by controlled dielectric breakdown. *PloS one*, 9(3):e92880, 2014.

[25] Kyle Briggs, Martin Charron, Harold Kwok, Timothea Le, Sanmeet Chahal, José Bustamante, Matthew Waugh, and Vincent Tabard-Cossa. Kinetics of nanopore fabrication during controlled breakdown of dielectric membranes in solution. *Nanotechnology*, 26(8):084004, 2015.

[26] Jingjie Sha, Zhonghua Ni, Lei Liu, Hong Yi, and Yunfei Chen. A novel method of fabricating a nanopore based on a glass tube for single-molecule detection. *Nanotechnology*, 22(17):175304, 2011.

[27] Miloslav Karhanek, Jennifer T Kemp, Nader Pourmand, Ronald W Davis, and Chris D Webb. Single DNA molecule detection using nanopipettes and nanoparticles. *Nano Letters*, 5(2):403–407, 2005. doi: 10.1021/nl0480464.

[28] Nicholas A. W. Bell, Vivek V. Thacker, Silvia Hernández-Ainsa, Maria E. Fuentes-Perez, Fernando Moreno-Herrero,

Tim Liedl, and Ulrich F. Keyser. Multiplexed ionic current sensing with glass nanopores. *Lab Chip*, 13:1859–1862, 2013. doi: 10.1039/c3lc50069a.

[29] Nicholas A. W. Bell and Ulrich F. Keyser. Specific protein detection using designed dna carriers and nanopores. *Journal of the American Chemical Society*, 137(5):2035–2041, 2015. doi: 10.1021/ja512521w.

[30] Nicholas AW Bell, Murugappan Muthukumar, and Ulrich F Keyser. Translocation frequency of double-stranded dna through a solid-state nanopore. *Physical Review E*, 93 (2):022401, 2016.

[31] Vivian Wang, Niklas Ermann, and Ulrich F. Keyser. Current enhancement in solid-state nanopores depends on three-dimensional DNA structure. *Nano Letters*, 19(8): 5661–5666, 2019. doi: 10.1021/acs.nanolett.9b02219.

[32] Daniel Fologea, Marc Gershow, Bradley Ledden, David S McNabb, Jene A Golovchenko, and Jiali Li. Detecting single stranded DNA with a solid state nanopore. *Nano Letters*, 5(10):1905–1909, 2005.

[33] A. J. Storm, J. H. Chen, H. W. Zandbergen, and C. Dekker. Translocation of double-strand DNA through a silicon oxide nanopore. *Physical Review E*, 71:051903, 2005.

[34] Arnold J. Storm, Cornelis Storm, Jianghua Chen, Henny Zandbergen, Jean-Francois Joanny, and Cees Dekker. Fast DNA translocation through a solid-state nanopore. *Nano Letters*, 5:1193, 2005.

[35] UF Keyser, J. van der Does, C. Dekker, and NH Dekker. Optical tweezers for force measurements on DNA in nanopores. *Review of Scientific Instruments*, 77:105105, 2006.

[36] UF Keyser, BN Koeleman, S van Dorp, D Krapf, RMM Smeets, SG Lemay, NH Dekker, and C Dekker. Direct force

measurements on DNA in a solid-state nanopore. *Nature Physics*, 2:473–477, 2006.

[37] Michiel van den Hout, Igor D Vilfan, Susanne Hage, and Nynke H Dekker. Direct force measurements on double-stranded rna in solid-state nanopores. *Nano Letters*, 10 (2):701–707, 2010.

[38] Christopher A Merchant, Ken Healy, Meni Wanunu, Vishva Ray, Neil Peterman, John Bartel, Michael D Fischbein, Kimberly Venta, Zhengtang Luo, AT Charlie Johnson, *et al.* Dna translocation through graphene nanopores. *Nano letters*, 10(8):2915–2921, 2010.

[39] Stefan W Kowalczyk, Alexander Y Grosberg, Yitzhak Rabin, and Cees Dekker. Modeling the conductance and DNA blockade of solid-state nanopores. *Nanotechnology*, 22(31): 315101, 2011. doi: 10.1088/0957-4484/22/31/315101.

[40] Stefan W Kowalczyk, David B Wells, Aleksei Aksimentiev, and Cees Dekker. Slowing down DNA translocation through a nanopore in lithium chloride. *Nano Letters*, 12 (2):1038–1044, 2012.

[41] F. Traversi, C. Raillon, S. M. Benameur, K. Liu, S. Khlybov, M. Tosun, D. Krasnozhon, A. Kis, and A. Radenovic. Detecting the translocation of DNA through a nanopore using graphene nanoribbons. *Nature Nanotechnology*, 8 (12):939–945, nov 2013. doi: 10.1038/nnano.2013.240.

[42] B. Luan and A. Aksimentiev. Electro-osmotic screening of the DNA charge in a nanopore. *Physical Review E*, 78(2): 021912, 2008.

[43] Ulrich F. Keyser, Stijn van Dorp, and Serge G. Lemay. Tether forces in DNA electrophoresis. *Chemical Society Reviews*, 39:939–947, 2010. doi: 10.1039/B902072C.

[44] Sebastian Getfert, Thomas Töws, and Peter Reimann. Opposite translocation of long and short oligomers through a

nanopore. *Physical Review E*, 87(6):062710, 2013. doi: 10.1103/PhysRevE.87.062710.

[45] Wen-Jie Lan, Deric A Holden, Bo Zhang, and Henry S White. Nanoparticle transport in conical-shaped nanopores. *Analytical Chemistry*, 83(10):3840–3847, 2011. doi: 10.1021/ac200312n.

[46] Nadanai Laohakunakorn, Sandip Ghosal, Oliver Otto, Karolis Misiunas, and Ulrich F Keyser. DNA interactions in crowded nanopores. *Nano Letters*, 13(6):2798–2802, 2013.

[47] Stefan Kesselheim, Wojciech Müller, and Christian Holm. Origin of current blockades in nanopore translocation experiments. *Physical Review Letters*, 112:018101, January 2014. doi: 10.1103/PhysRevLett.112.018101.

[48] Li-Hsien Yeh, Mingkan Zhang, Shizhi Qian, and Jyh-Ping Hsu. Regulating dna translocation through functionalized soft nanopores. *Nanoscale*, 4(8):2685–2693, 2012.

[49] Georg Rempfer, Gary B. Davies, Christian Holm, and Joost de Graaf. Reducing spurious flow in simulations of electrokinetic phenomena. *The Journal of Chemical Physics*, 145(4):044901, 2016. doi: 10.1063/1.4958950.

[50] Georg Rempfer, Sascha Ehrhardt, Nadanai Laohakunakorn, Gary B. Davies, Ulrich F. Keyser, Christian Holm, and Joost de Graaf. Selective trapping of DNA using glass microcapillaries. *Langmuir*, 32(33):8525–8532, 2016. doi: 10.1021/acs.langmuir.6b02071.

[51] Georg Rempfer, Sascha Ehrhardt, Christian Holm, and Joost de Graaf. Nanoparticle translocation through conical nanopores: A finite element study of electrokinetic transport. *Macromolecular Theory and Simulations*, 26 (1):1600051, 2017. doi: 10.1002/mats.201600051.

[52] Florian Weik, Stefan Kesselheim, and Christian Holm. A coarse-grained DNA model for the prediction of current

signals in DNA translocation experiments. *The Journal of Chemical Physics*, 145(19):194106, 2016. doi: 10.1063/1.4967458.

[53] Florian Weik, Kai Szuttor, Jonas Landsgesell, and Christian Holm. Modeling the current modulation of dsDNA in nanopores – from mean-field to atomistic and back. *European Physical Journal Special Topics*, 227(14):1639–1655, 2019. doi: 10.1140/epjst/e2019-800189-3.

[54] Stijn van Dorp, Ulrich F. Keyser, Nynke H. Dekker, Cees Dekker, and Serge G. Lemay. Origin of the electrophoretic force on DNA in solid-state nanopores. *Nature Physics*, 5 (5):347–351, May 2009. ISSN 1745-2473.

[55] Jehanzeb Hameed Chaudhry, Jeffrey Comer, Aleksei Aksimentiev, and Luke N Olson. A stabilized finite element method for modified poisson-nernst-planck equations to determine ion flow through a nanopore. *Communications in computational physics*, 15(1):93–125, 2014.

[56] Maria Fyta, Simone Melchionna, and Sauro Succi. Translocation of biomolecules through solid-state nanopores: Theory meets experiments. *Journal of Polymer Science Part B: Polymer Physics*, 49(14):985–1011, 2011. doi: 10.1002/polb.22284.

[57] Yanxiao Feng, Yuechuan Zhang, Cuifeng Ying, Deqiang Wang, and Chunlei Du. Nanopore-based fourth-generation DNA sequencing technology. *Genomics, proteomics & bioinformatics*, 13(1):4–16, 2015.

[58] Wenqing Shi, Alicia K Friedman, and Lane A Baker. Nanopore sensing. *Analytical chemistry*, 89(1):157–188, 2017.

[59] Long Luo, Sean R German, Wen-Jie Lan, Deric A Holden, Tony L Mega, and Henry S White. Resistive-pulse analysis of nanoparticles. *Annual Review of Analytical Chemistry*, 7:513–535, 2014. doi: 10.1146/annurev-anchem-071213-020107.

[60] Sandip Ghosal, John D Sherwood, and Hsueh-Chia Chang. Solid-state nanopore hydrodynamics and transport. *Biomicrofluidics*, 13(1):011301, 2019.

[61] Aleksij Aksementiev, Jiunn B. Heng, Gregory Timp, and Klaus Schulten. Microscopic kinetics of DNA translocation through syntetic nanopores. *Biophysical Journal*, 87:2086–2097, 2004.

[62] S. Reboux, F. Capuani, N. Gonzales-Segredo, and Daan Frenkel. Lattice-boltzmann simulations of ionic current modulation by DNA translocation. *Journal of Chemical Theory and Computation*, 2:495–503, 2006. doi: 10.1021/ct050340g.

[63] T. A. Knotts IV, N. Rathore, D. C. Schwartz, and J. J. de Pablo. A coarse grain model for DNA. *The Journal of Chemical Physics*, 126:084901, 2007.

[64] Maria Fyta, Simone Melchionna, Sauro Succi, and Efthimios Kaxiras. Hydrodynamic correlations in the translocation of a biopolymer through a nanopore: Theory and multiscale simulations. *Physical Review E*, 78:036704, September 2008. doi: 10.1103/PhysRevE.78.036704.

[65] E J Sambriski, D C Schwartz, and J J de Pablo. A mesoscale model of DNA and its renaturation. *Biophysical Journal*, 96(5):1675–90, 2009. doi: 10.1016/j.bpj.2008.09.061.

[66] Thomas E Ouldridge, Ard A Louis, and Jonathan PK Doye. DNA nanotweezers studied with a coarse-grained model of DNA. *Physical Review Letters*, 104(17):178101, 2010. doi: 10.1103/PhysRevLett.104.178101.

[67] Thomas E. Ouldridge, Ard A. Louis, and Jonathan P. K. Doye. Structural, mechanical, and thermodynamic properties of a coarse-grained DNA model. *The Journal of Chemical Physics*, 134(8):085101, 2011. doi: 10.1063/1.3552946.

[68] Alex Morriss-Andrews, Joerg Rottler, and Steven S Plotkin. A systematically coarse-grained model for dna and its predictions for persistence length, stacking, twist, and chirality. *The Journal of chemical physics*, 132(3): 01B611, 2010.

[69] Jeffrey Comer and Aleksei Aksimentiev. Predicting the DNA sequence dependence of nanopore ion current using atomic-resolution brownian dynamics. *The Journal of Physical Chemistry C*, 116(5):3376–3393, 2012.

[70] Chia Wei Hsu, Maria Fyta, Greg Lakatos, Simone Melchionna, and Efthimios Kaxiras. Ab initio determination of coarse-grained interactions in double-stranded DNA. *The Journal of Chemical Physics*, 137(10):105102, 2012.

[71] Tamar Schlick. *Molecular Modeling and Simulation*. Springer-Verlag New York, Inc., 2002.

[72] Kai Grass, Ute Böhme, Ulrich Scheler, Hervé Cottet, and Christian Holm. Importance of hydrodynamic shielding for the dynamic behavior of short polyelectrolyte chains. *Physical Review Letters*, 100:096104, 2008. doi: 10.1103/physrevlett.100.096104.

[73] Kai Grass and Christian Holm. Mesoscale modelling of polyelectrolyte electrophoresis. *Faraday Discussions*, 144: 57–70, 2010. doi: 10.1039/b902011j.

[74] Burkhard Dünweg and Anthony JC Ladd. Lattice Boltzmann simulations of soft matter systems. In *Advanced Computer Simulation Approaches for Soft Matter Sciences III*, pages 89–166. Springer, 2009.

[75] P. Español and P. Warren. Statistical mechanics of dissipative particle dynamics. *Europhysics Letters*, 30(4):191, 2007.

[76] Tobias Rau, Florian Weik, and Christian Holm. A dsDNA model optimized for electrokinetic applications. *Soft Matter*, 13:3918–3926, 2017. doi: 10.1039/C7SM00270J.

[77] D. A. Hoagland, E. Arvanitidou, and C. Welch. Capillary electrophoresis measurements of the free solution mobility for several model polyelectrolyte systems. *Macromolecules*, 32(19):6180–6190, September 1999.

[78] Annaël Brunet, Catherine Tardin, Laurence Salomé, Philippe Rousseau, Nicolas Destainville, and Manoel Manghi. Dependence of DNA persistence length on ionic strength of solutions with monovalent and divalent salts: A joint theory–experiment study. *Macromolecules*, 48(11): 3641–3652, 2015. doi: 10.1021/acs.macromol.5b00735.

[79] G. V. Ramanathan and Charles P. Woodbury, Jr. The cell model for polyelectrolytes with added salt. *The Journal of Chemical Physics*, 82(3):1482–91, 1985.

[80] Markus Deserno, Christian Holm, and Sylvio May. Fraction of condensed counterions around a charged rod: Comparison of Poisson-Boltzmann theory and computer simulations. *Macromolecules*, 33:199–206, 2000. doi: 10.1021/ma990897o.

[81] Markus Deserno and Christian Holm. Cell-model and poisson-boltzmann-theory: A brief introduction. In C. Holm, P. Kékicheff, and R. Podgornik, editors, *Electrostatic Effects in Soft Matter and Biophysics*, volume 46 of *NATO Science Series II - Mathematics, Physics and Chemistry*, pages 27–50. Kluwer Academic Publishers, Dordrecht, Nl, December 2001. doi: 10.1007/978-94-010-0577-7_2.

[82] Kai Szuttor, Florian Weik, Jean-Noël Grad, and Christian Holm. Modeling the current modulation of bundled DNA structures in nanopores. *The Journal of Chemical Physics*, 154(5):054901, 2021. doi: 10.1063/5.0038530.

[83] Miru Lee, Christoph Lohrmann, Kai Szuttor, Harold Auradou, and Christian Holm. The influence of motility on bacterial accumulation in a microporous channel. *Soft Matter*, 17:893–902, 2021. doi: 10.1039/D0SM01595D.

[84] Florian Weik, Rudolf Weeber, Kai Szuttor, Konrad Breitsprecher, Joost de Graaf, Michael Kuron, Jonas Landsgesell, Henri Menke, David Sean, and Christian Holm. ESPResSo 4.0 – an extensible software package for simulating soft matter systems. *European Physical Journal Special Topics*, 227(14):1789–1816, 2019. doi: 10.1140/epjst/e2019-800186-9.

[85] Miru Lee, Kai Szuttor, and Christian Holm. A computational model for bacterial run-and-tumble motion. *The Journal of Chemical Physics*, 150:174111, 2019. doi: 10.1063/1.5085836.

[86] Jonas Landsgesell, David Sean, Patrick Kreissl, Kai Szuttor, and Christian Holm. Modeling gel swelling equilibrium in the mean field: From explicit to Poisson-Boltzmann models. *Physical Review Letters*, 122:208002, 5 2019. doi: 10.1103/PhysRevLett.122.208002.

[87] Johannes Hartmann, Tamal Roy, Kai Szuttor, Jens Smiatek, Christian Holm, and Steffen Hardt. Relaxation of surface-tethered polymers under moderate confinement. *Soft Matter*, 14(38):7926–7933, 2018. doi: 10.1039/c8sm01246f.

[88] Tamal Roy, Kai Szuttor, Jens Smiatek, Christian Holm, and Steffen Hardt. Conformation and dynamics of long-chain end-tethered polymers in microchannels. *Polymers*, 11(3):488, 2019. doi: 10.3390/polym11030488.

[89] Kai Szuttor, Tamal Roy, Steffen Hardt, Christian Holm, and Jens Smiatek. The stretching force on a tethered polymer in pressure-driven flow. *The Journal of Chemical Physics*, 147(3):034902, 2017. doi: 10.1063/1.4993619.

[90] Tamal Roy, Kai Szuttor, Jens Smiatek, Christian Holm, and Steffen Hardt. Electric-field-induced stretching of surface-tethered polyelectrolytes in a microchannel. *Physical Review E*, 96(3):032503, 2017. doi: 10.1103/PhysRevE.96.032503.

[91] Tamal Roy, Kai Szuttor, Jens Smiatek, Christian Holm, and Steffen Hardt. Stretching of surface-tethered polymers in pressure-driven flow under confinement. *Soft Matter*, 13: 6189–6196, 2017. doi: 10.1039/C7SM00306D.

[92] Gordon Betts, Peter Desaix, Eddie Johnson, Jody Johnson, Oksana Korol, Dean Kruse, Brandon Poe, James Wise, Mark Womble, and Kelly Young. *Anatomy & Physiology*. OpenStax, 2017. URL https://openstax.org/details/books/anatomy-and-physiology.

[93] Carlos Ernesto Castro, Fabian Kilchherr, Do-Nyun Kim, Enrique Lin Shiao, Tobias Wauer, Philipp Wortmann, Mark Bathe, and Hendrik Dietz. A primer to scaffolded DNA origami. *Nature methods*, 8(3):221, 2011.

[94] Yonggang Ke, Shawn M Douglas, Minghui Liu, Jaswinder Sharma, Anchi Cheng, Albert Leung, Yan Liu, William M Shih, and Hao Yan. Multilayer DNA origami packed on a square lattice. *Journal of the American Chemical Society*, 131(43):15903–15908, 2009. doi: 10.1021/ja906381y.

[95] William C. Swope, Hans C. Andersen, Peter H. Berens, and Kent R. Wilson. A computer simulation method for the calculation of equilibrium constants for the formation of physical clusters of molecules: Application to small water clusters. *The Journal of Chemical Physics*, 76(1):637–649, 1982. doi: 10.1063/1.442716.

[96] R. Kubo. The fluctuation-dissipation theorem. *Reports on Progress in Physics*, 29(1):255–284, 1966. doi: 10.1088/0034-4885/29/1/306.

[97] S. Chen and G. D. Doolen. Lattice Boltzmann method for fluid flows. *Annual Review of Fluid Mechanics*, 30(1): 329–364, 1998.

[98] Joseph Liouville. Note sur la théorie de la variation des constantes arbitraires. *Journal de mathématiques pures et appliquées*, pages 342–349, 1838.

[99] Harold Grad. On the kinetic theory of rarefied gases. *Communications on pure and applied mathematics*, 2(4):331–407, 1949.

[100] Ludwig Boltzmann. Weitere Studien über das Wärmegleichgewicht unter Gasmolekülen. In S.G. Brush, editor, *Kinetische Theorie II: Irreversible Prozesse Einführung und Originaltexte*, pages 115–225. Vieweg+Teubner Verlag, Wiesbaden, 1970. ISBN 978-3-322-84986-1. doi: 10.1007/978-3-322-84986-1_3.

[101] Cyrus K Aidun and Jonathan R Clausen. Lattice-Boltzmann method for complex flows. *Annual review of fluid mechanics*, 42:439–472, 2010. doi: 10.1146/annurev-fluid-121108-145519.

[102] P. L. Bhatnagar, E. P. Gross, and M. Krook. A model for collision processes in gases. i. small amplitude processes in charged and neutral one-component systems. *Physical Review*, 94(3):511, 1954.

[103] Dominique d'Humières and Piere Lallemand. Numerical simulations of hydrodynamics with lattice gas automata in two dimensions. *Complex Systems*, 1(4):599–632, 1987.

[104] Yuanxun Bill Bao and Justin Meskas. Lattice boltzmann method for fluid simulations. *Courant Institute of Mathematical Sciences*, 2011.

[105] P. Ahlrichs and B. Dünweg. Lattice-Boltzmann simulation of polymer-solvent systems. *International Journal of Modern Physics C*, 9(8):1429–1438, 1998. doi: 10.1142/S0129183198001291.

[106] B. Dünweg and A. J. C. Ladd. Lattice Boltzmann simulations of soft matter systems. In Christian Holm and Kurt Kremer, editors, *Advanced Computer Simulation Approaches for Soft Matter Sciences III*, number 221 in Advances in Polymer Science, pages 89–166. Springer, Berlin, 2009. ISBN 9783540877059. doi: 10.1007/12_2008_4.

[107] J. N. Reddy. *An introduction to the finite element method*. McGraw-Hill series in mechanical engineering. McGraw-Hill Higher Education, 2006. ISBN 9780-07-246685-0. URL http://books.google.com/books?id=8gqnRwAACAAJ.

[108] J. L. Anderson. Colloid transport by interfacial forces. *Annual Review of Fluid Mechanics*, 21:61–99, 1989. doi: 10.1146/annurev.fl.21.010189.000425.

[109] Axel Arnold, Bernward A. Mann, Hans Jörg Limbach, and Christian Holm. ESPResSo – an extensible simulation package for research on soft matter systems. In *Forschung und wissenschaftliches Rechnen 2003*. Gesellschaft für wissenschaftliche Datenverarbeitung mbH.

[110] Axel Arnold, Bernward A. Mann, and Christian Holm. Simulating charged systems with ESPResSo. In M. Ferrario, G. Ciccotti, and K. Binder, editors, *Computer Simulations in Condensed Matter: from Materials to Chemical Biology*, number 1 in Lecture Notes in Physics, pages 193–222. Springer, Berlin, Germany, 2006. doi: 10.1007/3-540-35273-2_6.

[111] Axel Arnold, Olaf Lenz, Stefan Kesselheim, Rudolf Weeber, Florian Fahrenberger, Dominic Röhm, Peter Košovan, and Christian Holm. ESPResSo 3.1 – molecular dynamics software for coarse-grained models. In M. Griebel and M. A. Schweitzer, editors, *Meshfree Methods for Partial Differential Equations VI*, volume 89 of *Lecture Notes in Computational Science and Engineering*, pages 1–23. Springer Berlin Heidelberg, 2013. doi: 10.1007/978-3-642-32979-1_1.

[112] R. W. Hockney and J. W. Eastwood. *Computer Simulation Using Particles*. IOP, London, 1988.

[113] Mark James Abraham, Teemu Murtola, Roland Schulz, Szilárd Páll, Jeremy C Smith, Berk Hess, and Erik Lindahl. GROMACS: High performance molecular simula-

tions through multi-level parallelism from laptops to supercomputers. *SoftwareX*, 1:19–25, 2015. doi: 10.1016/j.softx.2015.06.001.

[114] S. J. Plimpton. Fast parallel algorithms for short-range molecular dynamics. *Journal of Computational Physics*, 117:1–19, 1995. doi: 10.1006/jcph.1995.1039.

[115] Steve Plimpton, Paul Crozier, and Aidan Thompson. LAMMPS-large-scale atomic/molecular massively parallel simulator. *Sandia National Laboratories*, 18, 2007.

[116] Alessio Fragasso, Sonja Schmid, and Cees Dekker. Comparing current noise in biological and solid-state nanopores. *ACS nano*, 14(2):1338–1349, 2020.

[117] Yong Duan, Chun Wu, Shibasish Chowdhury, Mathew C. Lee, Guoming Xiong, Wei Zhang, Rong Yang, Piotr Cieplak, Ray Luo, Taisung Lee, James Caldwell, Junmei Wang, and Peter Kollman. A point-charge force field for molecular mechanics simulations of proteins based on condensed-phase quantum mechanical calculations. *Journal of Computational Chemistry*, 24(16):1999–2012, 2003. ISSN 1096-987X.

[118] David E. Smith and Liem X. Dang. Computer simulations of NaCl association in polarizable water. *The Journal of Chemical Physics*, 100:3757, 1994.

[119] Liem X Dang and Peter A Kollman. Free energy of association of the K+:18-crown-6 complex in water: a new molecular dynamics study. *The Journal of Physical Chemistry*, 99(1):55–58, 1995. doi: 10.1021/j100001a011.

[120] Liem X Dang. Mechanism and thermodynamics of ion selectivity in aqueous solutions of 18-crown-6 ether: a molecular dynamics study. *Journal of the American Chemical Society*, 117(26):6954–6960, 1995.

[121] H. J. C. Berendsen, J. R. Grigera, and T. P. Straatsma. The missing term in effective pair potentials. *The Journal*

of Physical Chemistry, 91(24):6269–6271, November 1987. doi: 10.1021/j100308a038.

[122] Frank H Stillinger Jr and Ronald Lovett. Ion-pair theory of concentrated electrolytes. I. basic concepts. *The Journal of Chemical Physics*, 48(9):3858–3868, 1968. doi: 10.1063/1.1669709.

[123] Timothy J Richmond and Curt A Davey. The structure of DNA in the nucleosome core. *Nature*, 423(6936):145–150, 2003. doi: 10.1038/nature01595.

[124] P. Ahlrichs and B. Dünweg. Simulation of a single polymer chain in solution by combining lattice Boltzmann and molecular dynamics. *The Journal of Chemical Physics*, 111 (17):8225–8239, 1999.

[125] Lars Onsager. Theories of concentrated electrolytes. *Chemical Reviews*, 13(1):73–89, 1933. doi: 10.1021/cr60044a006.

[126] Ralph M. M. Smeets, Ulrich F. Keyser, Diego Krapf, Meng-Yue Wu, Nynke H. Dekker, and Cees Dekker. Salt dependence of ion transport and DNA translocation through solid-state nanopores. *Nano Letters*, 6:89–95, 2006.

[127] Roland R. Netz. Electrofriction and dynamic Stern layers at planar charged surfaces. *Physical Review Letters*, 91 (13):138101, 2003. doi: 10.1103/physrevlett.91.138101.

[128] JR Blake. A note on the image system for a stokeslet in a no-slip boundary. *Mathematical Proceedings of The Cambridge Philosophical Society*, 70:303–310, 1971. doi: 10.1017/S0305004100049902.

[129] P.W.K. Rothemund. Folding DNA to create nanoscale shapes and patterns. *Nature*, 440(7082):297–302, 2006.

[130] Nicholas A. W. Bell, Christian. R. Engst, Marc Ablay, Giorgio Divitini, Caterina Ducati, Tim Liedl, and Ulrich F. Keyser. DNA Origami nanopores. *Nano Letters*, 12(1): 512–517, 2012. doi: 10.1021/nl204098n.

[131] Silvia Hernández-Ainsa, Nicholas AW Bell, Vivek V Thacker, Kerstin Gooepfrich, Karolis Misiunas, Maria Eugenia Fuentes-Perez, Fernando Moreno-Herrero, and Ulrich F Keyser. DNA origami nanopores for controlling DNA translocation. *ACS Nano*, 7(7):6024–6030, 2013.

[132] Brian J. Kirby. *Micro- and Nanoscale Fluid Mechanics: Transport in Microfluidic Devices*. Cambridge University Press, 2010. ISBN 9781139489836. doi: 10.1017/CBO9780511760723. URL http://www.kirbyresearch.com/textbook.

[133] A. L. Horvath. *Handbook of Aqueous Electrolyte Solutions*. Ellis Horwood Ltd., Chichester, 1 edition, 1985.

[134] Burkhard Dünweg, Vladimir Lobaskin, Krishnan Seethalakshmy-Hariharan, and Christian Holm. Colloidal electrophoresis: scaling analysis, Green-Kubo relation, and numerical results. *Journal of Physics: Condensed Matter*, 20(40):404214, 2008. doi: 10.1088/0953-8984/20/40/404214.

[135] Vladimir Lobaskin, Burkhard Dünweg, Martin Medebach, Thomas Palberg, and Christian Holm. Electrophoresis of colloidal dispersions in the low-salt regime. *Physical Review Letters*, 98:176105, April 2007. doi: 10.1103/physrevlett.98.176105.

[136] Roland R. Netz. Nonequilibrium unfolding of polyelectrolyte condensates in electric fields. *Physical Review Letters*, 90(12):128104, March 2003. doi: 10.1103/physrevlett.90.128104.

[137] Lorenz J. Steinbock, Alex Lucas, Oliver Otto, and Ulrich F. Keyser. Voltage-driven transport of ions and DNA through nanocapillaries. *Electrophoresis*, 33(23):3480–3487, nov 2012. doi: 10.1002/elps.201100663.

[138] Stuart Allison, Chuanying Chen, and Dirk Stigter. The length dependence of translational diffusion, free solution

electrophoretic mobility, and electrophoretic tether force of rigid rod-like model duplex DNA. *Biophysical Journal*, 81(5):2558–2568, 2001. ISSN 0006-3495. doi: 10.1016/S0006-3495(01)75900-0.

[139] Calin Plesa, Nick Van Loo, Philip Ketterer, Hendrik Dietz, and Cees Dekker. Velocity of DNA during translocation through a solid-state nanopore. *Nano Letters*, 15(1):732–737, 2015. doi: 10.1021/nl504375c.

[140] Stephanie J Heerema, Leonardo Vicarelli, Sergii Pud, Raymond N Schouten, Henny W Zandbergen, and Cees Dekker. Probing DNA translocations with inplane current signals in a graphene nanoribbon with a nanopore. *ACS Nano*, 12(3):2623–2633, 2018.

[141] Siddharth Shekar, David J Niedzwiecki, Chen-Chi Chien, Peijie Ong, Daniel A Fleischer, Jianxun Lin, Jacob K Rosenstein, Marija Drndić, and Kenneth L Shepard. Measurement of DNA translocation dynamics in a solid-state nanopore at 100 ns temporal resolution. *Nano Letters*, 16 (7):4483–4489, 2016.